CYRIC

ANNUAL REPORT

2006

(January 2006 - December 2006)

CYCLOTRON AND RADIOISOTOPE CENTER
TOHOKU UNIVERSITY
http://www.cyric.tohoku.ac.jp/

PREFACE

In this twenty-seventh issue of the CYRIC Annual Report, we summarize the activities in research and development, and in training of radioisotope safe-treatment at the Cyclotron and Radioisotope Center (CYRIC) during the calendar year 2006.

Research at CYRIC was carried out in the fields of nuclear physics, nuclear chemistry, material sciences, nuclear medicine using PET (oncology, brain study, pharmacology), radiopharmaceutical chemistry, health physics, nuclear instrumentation, nuclear medical engineering (diagnosis and therapy technology), nuclear engineering and elemental analysis using PIXE.

Developments and improvements on nuclear instruments and techniques have progressed; one of the 2006 highlights is the construction of ultra high spatial resolution semiconductor PET which has ~0.8mm FWHM in the central region of FOV. It is the first achievement of less than 1mm FWHM practical animal PET.

Both the K=110MeV AVF cyclotron and K=12 MeV AVF cyclotron were steady operated in this year. A total of 2695 hours of beam-time of the K=110 MeV cyclotron were delivered for scheduled operation in research work.

The newly designed ion guide system (RF ion guide system) of on-line isotope separation for short lived neutron rich nuclei has successfully been developed and has obtained ten times higher mass-separated yields than those of old type ion guide method for neutron rich nuclei having sub-second half-lives by the proton induced Uranium fission reaction.

As in last year [^{18}F]FDG, [^{18}F]FRP-170, [^{11}C]methionine, [^{11}C]doxepin, [^{11}C]raclopride, [^{11}C]donepezil, [^{11}C]BF-227 and [^{15}O]water were routinely prepared and duly supplied to clinical PET studies. No new PET probe was introduced to clinical research in this year, while basic studies including evaluation of new amyloid imaging agents and development of automated modules of miniature size and microreactors for PET probe syntheses were extensively carried out. The production of ^{124}I, which was established this year, is expected to accelerate our molecular imaging study by widening the variety of PET probes.

There was an important event in the year 2006 regarding life science research. Tohoku University started the "Molecular Imaging Program" including an educational course for postgraduate students supported by a JST grant for “research and education in molecular imaging”. This program is run in collaboration with National Institute of Radiological

Science, Molecular Imaging Research Center, Chiba, Japan, and CYRIC is playing an important role as the site of basic and clinical experiments.

Thus, molecular imaging of dementia has been further activated at CYRIC. [^{11}C]BF-227, introduced to clinical studies as the first domestically-developed β-amyloid imaging agent, has been tested in up to 70 clinical examinations, and the first academic report was published in Journal of Nuclear Medicine. The summarized report is included in this issue of the CYRIC Annual Report. The first academic report regarding the clinical application of [^{11}C]Donepezil is also to be published in British Journal of Clinical Pharmacology. The summarized report is also included in this issue of the Annual Report. Other routine tracers have been supplied to PET studies as before. [^{18}F]FDG study is still active, expanding the research topic to the examination of dash (fast running) and energy redistribution mechanism at whole-body level. Clinical application of [^{11}C]doxepin to phamacogenetics and pharmacogenomics research is ongoing. [^{15}O]water resulted in many excellent papers regarding attention and cognition of beauty and emotion. The number of [^{11}C]methionine studies for clinical diagnosis in neurosurgery has been steadily increasing, reflecting high clinical needs at Tohoku University Hospital.

The research program on PIXE analysis has been carried out by using an electrostatic accelerator (4.5 MV Dynamitron) at the Fast Neutron Laboratory (FNL), Graduate School of Engineering, Tohoku University, under the scientific tie up between CYRIC and FNL. A total of 480 hours of beam-time was served to this program. Micro-PIXE analysis, STIM analysis, and Micron-CT were performed by the use of the micro-beam formation system.

The training for radioisotope safe-treatment was carried out as usual. In 2006, a total of 907 staffs and students of Tohoku University took three courses: 1) Radioisotopes and radiation generators (465 trainees), 2) X-ray machines and electron microscope (354), and 3) Synchrotron Radiation (88). The number of trainees in this year decreased by about ten percents compared with the previous year (1097). The English classes for each course were practiced for 61 foreign students and scientists.

We are most grateful to Tohoku University and to the Ministry of Education, Sports, Culture, Science and Technology for continuous support.

January 2007

Keizo ISHII
Director
Cyclotron and Radioisotope Center, Tohoku University

EDITORS:

Keizo ISHII
Masatoshi ITOH
Mamoru BABA
Ren IWATA
Yasuhiro SAKEMI
Tsutomu SHINOZUKA

WORD PROCESSED BY

Yu-ko YAMASHITA

CONTENTS

IV. NUCLEAR MEDICAL ENGINEERING

V. PIXE AND ENVIRONMENTAL ANALYSIS

VI. RADIOCHEMISRTY AND NUCLEAR CHEMISTRY

VII. RADIOPHARMACEUTICAL CHEMISTRY AND BIOLOGY

VIII. NUCLEAR MEDICINE

I. NUCLEAR PHYSICS

I. 1. Search for the 4α Condensed State in ^{16}O

Itoh M., Matsuo R., Ouchi H., Ozeki K., Sakemi Y., Sugimoto N., and Terazono T.

Cyclotron and Radioisotope Center, Tohoku University

Recently, Tohsaki et al[1] explained the 7.65 MeV, 0_2^+ state of ^{12}C as a Bose-Einstein condensation-like state, in which all constituent α clusters condense into the lowest S-orbit, and are loosely bound. They predicted the 4α condensed state also exists around the 4α breakup threshold energy of 14.4 MeV in ^{16}O. In the experimental study, Wakasa et al[2] found a new candidate for the 4α condensed state in ^{16}O by measuring inelastic α scattering at E_α = 400 MeV. The excitation energy of 13.6 ± 0.1 MeV, the width of 0.6 ± 0.2 MeV, and the cross section of this candidate state were consistent with the theoretical prediction. However, since there are some 0^+ states around the 4α threshold energy in ^{16}O, they could not assert conclusively it was the 4α condensed sate. In this study, on the other hand, we would determine experimentally the 4α condensed state by measuring decay-α particles via the $^{12}C(^{16}O,^{16}O^*[\alpha+X])^{12}C$ reaction. The branching ratio of the α decay from Nα condensed state to the (N-1) α one is larger than those of other channels, because the overlap of their wave functions is very large. Thus, if the excitation energy of the 4α condensed state is higher than the $^{12}C(0_2^+)$ + α threshold, we can select the 4α condensed state from the candidates.

The test experiment was performed at the CYRIC 41 course beam line by using the $^{16}O^{5+}$ beam accelerated up to 160 MeV in the K=110 MeV AVF cyclotron. The momentum spread of the beam was limited to less than a few percent by a slit installed between two analyzer-magnets, ANA1 and ANA2 (see Ref. 3). High quality $^{16}O^{5+}$ beam bombarded a self-supported natural carbon foil. The thickness of the carbon foil was a 200 μg/cm^2. The recoiling ^{12}C nucleus was detected in a silicon detector (SSD1) of a surface barrier type. The decay-α particle was caught in a 50×50 mm^2 silicon detector (SSD2), which was segmented into 10 silicon diodes of a 5×50 mm^2 size. In order to reduce

background particles such as elastically scattered ^{16}O, beam halo, and so on, we installed a 200 μm aluminum plate in front of SSD2. The observed particles were identified by the TOF method. Figure 1 shows the TOF spectra of the SSD1 and SSD2. Since SSD1 was placed at the 100 mm distance from the target, it was difficult to identify a locus of ^{12}C. Then, we have recognized the locus of ^{12}C by measuring the recoiling ^{12}C of elastic scattering. In SSD2, which was put at the position of 200 mm from the target, it was almost only for α particles to come into the detector. The aluminum plate worked very well. In the present experiment, we measured decay α particles from the states at the excitation energy of 15.5 MeV on ^{16}O. The setting angles of SSD1 and SSD2 were 61° and 10°, respectively. The energy of the recoiling ^{12}C was 6.0 MeV. Figure 2 shows the energy spectrum of SSD2. The energy of decay α particles to the 0_2^+ state of ^{12}C are about 30 – 40 MeV, which depend on angles of decay particles. The α particles of the energy over 40 MeV arise from the $^{12}C(2_1^+)+\alpha$ or $^{12}C(g.s.)+\alpha$ channels. As shown in Fig. 2, decay α particles from the 0_2^+ state of ^{12}C were observed. However, we could not separate decay channels in this stage because of the lack of the angular resolution. Now, we are preparing the double-side silicon strip detector for improvement of the angular resolution.

References

1) Tohsaki., et al., Phys. Rev. Lett. **87** (2001) 192501.
2) Wakasa., et al., Phys. Lett. B**653** (2007) 173.
3) Itoh M., et al., CYRIC Annual Report **2005** (2005) 18.

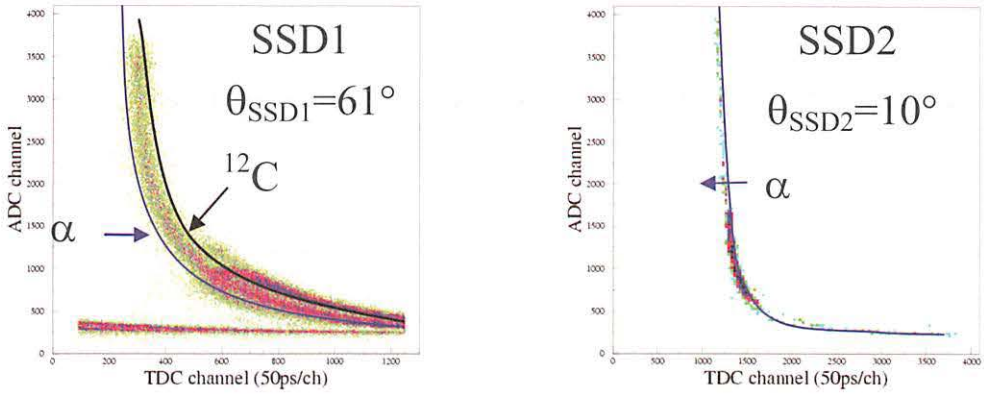

Figure 1. TOF spectra of SSD1 and SSD2.

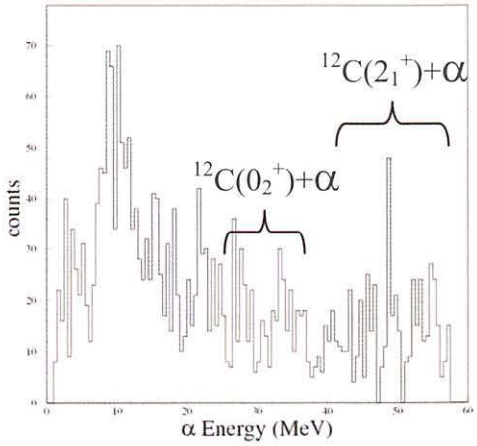

Figure 2. The energy spectrum of decay α particles from the excited ^{16}O state at the excitation energy of 15.5 MeV.

I. 2. Production of Radioactivities for Undergraduate Students

Kanda H.[1], Iguchi A.[1], Maeda K.[1], Miyase H.[1], Ohtsuki T.[2], Shinozuka T.[3], and Yuki H.[2]

[1]Department of Physics, Graduate School of Science, Tohoku University
[2]Laboratory of Nuclear Science, Tohoku University
[3]Cyclotron and Radioisotope Center, Tohoku University

We are providing the introductory nuclear physics for undergraduate students with use of the radioactive isotopes as a subject in the "Basic Research in Physics *(Butsurigaku kiso kenkyuu)*[1,2]." The aim of this class is to instruct students in the fundamentals of the radiation and the radioactivity with the measurement of the radiation. The production of the radioactive isotopes with use of the accelerator and the measurement of the gamma-ray from them enabled us of (1) the measurement of the life time of the radioactive decay and its randomness, (2) the demonstration of the conversion of the element and (3) the practical presentation of the nuclear size via measurements of the cross sections of the nuclear reaction. The proton beam of 20 MeV was irradiated on the natural iron and titanium and the gamma-ray from the produced nuclides was measured with use of a NaI(Tl) probe once a week in 2– 3 weeks. By measuring the energy spectra of the gamma-ray, students identify the produced nuclides. By the decrease of the counting rates, half lives of the nuclides are measured. The cross section of the concerned reaction is measured by the counting rates, the branching ratio of the gamma-ray, the time after the production, and the some assumptions on the detection efficiencies. We prepare ten plates of iron of 0.1 mm thick for the measurement of the energy dependence of the ^{56}Fe (p, n) ^{56}Co reaction.

The half life of the ^{56}Co produced via ^{56}Fe (p, n) ^{56}Co reaction is 77.3 days which leads small change of counting rates in several weeks. On the other hand, the half life of ^{48}V produced via ^{48}Ti (p, n) ^{48}V reaction is 16.0 days, and it is sufficiently short for the measurement of the decrease of the counting rates. The experiments were performed three times with changing the group of students. The results from three groups of students and the reference value from the Table of Isotopes[3] are shown in Table 1. Because students were not well trained for the estimation of errors in their measurements, no error was shown

on each data except for one measurement. As seen in the table, discrepancy of the half lives between the measured values and the reference value for ^{56}Co is larger than that for ^{48}V. The simple estimation of the statistic errors on the measured half lives of ^{56}Co ranged from 10 to 20 days. It means these results are consistent with the reference value within the statistic errors. The statistic errors on the measured half lives of ^{48}V ranged from 0.5 to 0.9 days. These differences were useful for the students to consider the errors on the measurements.

The measurement of the cross section for ^{56}Fe (p, n) ^{56}Co was not always successful. A result by one group which is relatively good one in the results by the three groups is compared with the reference values from Experimental Nuclear Reaction Data[4] (Fig. 1). It seemed difficult to make students to understand the realistic idea on the scale of the nucleus and the cross section of the nuclear reactions with the current explanations for them. On the other hand, the energy loss of the proton in the iron was reasonably derived. It shows that the students can imagine a concrete idea of the resistance which was suffered by a charged particle travelling through matter. For convincing the students of the nuclear scale, we may have to improve our explanation about the method of the measurements and the relation between the nuclear size and the cross sections of the nuclear reactions.

This year we continued the experiments with the production of radioactivities at CYRIC as a subject in the "Basic Research in Physics *(Butsurigaku kiso kenkyuu).*" Though we designed this experiment to be comprehensive for the students, there is still a room for the improvement in the measurement of the cross sections. By taking account of the new class: "Physics Experiment III" which is the continuing class of the "Basic Research in Physics" and starts from 2008, we improve the experiment and prepare for the new class.

References

1) Kanda H., et al., CYRIC Annual Report 2004.
2) Kanda H., et al., CYRIC Annual Report 2005.
3) WWW Table of Isotopes, http://ie.lbl.gov/toi/.
4) Experimental Nuclear Reaction Data, http://www.nndc.bnl.gov/exfor/exfor00.htm.

Table 1. The half lives of ^{56}Co and ^{48}V reported by three groups of students and from the reference[3] in the unit of day.

Group	^{56}Co	^{48}V
1	69	17.3
2	48	18.5 ± 0.9
3	57.5	16.7
Reference	77.27	15.9735

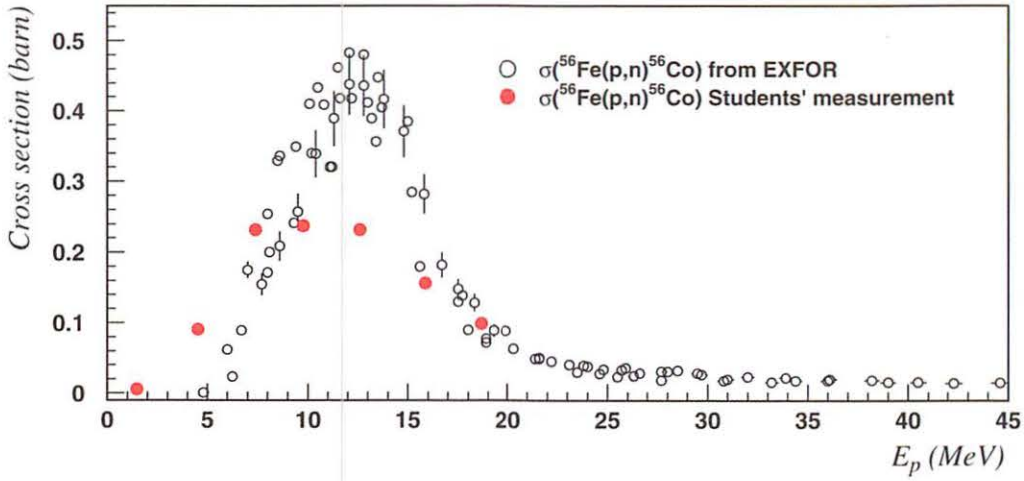

Figure 1. The cross sections of ^{56}Fe (p, n) ^{56}Co reaction with respect to the incident energy of the proton. Open circles represent the data from Experimental Nuclear Reaction Data Library[3] and red closed circles are the data from students' measurement.

II. NUCLEAR INSTRUMENTATION

II. 1. Discharge Ion Source for RFIGISOL

Wakui T.[1], Miyashita Y.[2], Sato N.[2], Ohguma M.[2], Tateoka M.[2], Nagano T.[2], Yamashita W.[2], Suzuki T.[2], Ukai M.[1], Yamazaki A.[1], and Shinozuka T.[1]

[1]*Cyclotron and Radioisotope Center, Tohoku University*
[2]*Department of Physics, Tohoku University*

The RF ion guide isotope separator on-line (RFIGISOL) has been developed for the study of nuclear structure of neutron-rich nuclei in the medium mass region[1,2]. The RFIGISOL is unique among IGISOL facilities in that it has a large volume gas cell for stopping energetic ions and DC and RF electric fields for guiding the stopped ions. This feature allows the ions to efficiently be extracted from the gas cell.

To check the performance of the RFIGISOL system without beams from accelerator (off-line), we have built a discharge ion source, which is placed inside the gas cell, replacing a Uranium target for on-line experiments. The discharge ion source produces ions from residual molecules in the gas cell and also from gaseous atoms added with a helium buffer gas. The produced ions are used as test beams for confirming the effect of electric fields, for studying properties of a beam transport line, and for optimization of the RFIGISOL system prior to on-line experiments.

Figure 1 shows a picture of the discharge ion source. It has a pair of copper electrodes which is mounted on a linear feed-through to change the source position in the gas cell. A discharge voltage is supplied to an electrode with a cable thread through the linear feed-through. The applied discharge voltage is ranging from 150 V to 200 V, depending on the pressure of buffer gas.

The produced ions are extracted from the gas cell and mass-separated for measurement of their mass spectra. Figure 2 shows a typical mass spectrum of light ions from residual molecules in the gas cell. The mass spectrum was measured using a picoammeter. In this measurement, the discharge voltage was 170 V and the pressure of helium buffer gas was 30 mbar. The obtained ion beam current for mass number 12 was 120 pA, which is high enough for studying the performance of the RFIGISOL system.

With the ion source, we have confirmed the effect of electric field guiding as described in Ref. 2.

References

1) Sonoda T., Fujita M., Yamazaki A., Endo T., Shinozuka T., Miyashita Y., Sato N., Goto A., Tanaka E., Suzuki T., Miyake T., Tanigaki M., Wada M., Nucl. Instr. Meth. **B254** (2007) 295.
2) Miyashita Y., Wakui T., Sato N., Yamazaki A., Endo T., Fujita M., Goto A., Kinoshita S.,Koike T., Ma Y., Miura Y., Miyake T., Nagano T., Ohguma M., Sonoda T., Suzuki T., Tamura H., Tanaka E., Tateoka M., Yamashita W., Ukai M., Shinozuka T., Nucl. Instr. Meth. to be published.

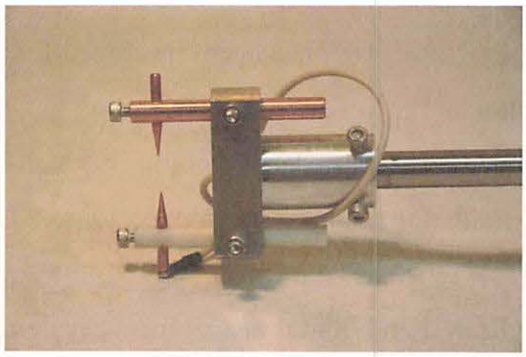

Figure 1. Discharge ion source placed in a large volume gas cell.

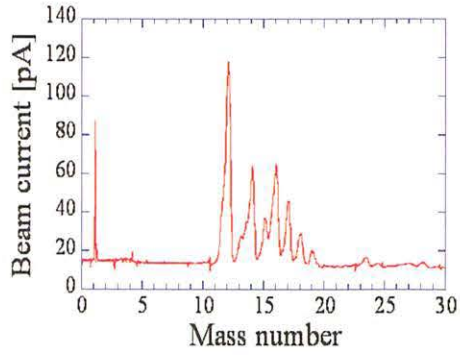

Figure 2. Typical mass spectrum of light ions.

II. 2. Beam Profile Monitor for Beam Injection Line

Yamashita W.[1], Ohguma M.[1], Miyashita Y.[1], Nagano T.[1], Suzuki T.[1], Sato N.[1], Tateoka M.[1], Ukai M.[2], Wakui T.[2], Yamazaki A.[2], and Shinozuka T.[2]

[1]*Department of Physics, Tohoku University*
[2]*Cyclotron and Radioisotope Center, Tohoku University*

Heavy ions from an all-permanent-magnet ECR ion source[1)] are delivered to the 930 cyclotron via a beam injection line, shown in Fig. 1. The beam transport efficiency of the injection line is typically 40%. To improve the beam transport efficiency, it is important to monitor the beam profile at several points in the injection line.

As the first step for developing the beam monitoring system, we have constructed a beam profile monitor (BPM) system, based on a BPM unit (Danfysik model 516). Figure 2 shows a schematic view of the BPM system. The probe has two vanes attached to a drive shaft at an angle of 45 degrees. The drive shaft oscillates the vanes. The movement makes possible to measure the cross-sectional beam distribution on both of the X and Y axes. The vanes are made by 0.5 mm thick aluminum plate. The current absorbed by the vanes is converted into voltage by a handmade I-V converter. Another signal corresponding to probe position is supplied from the probe electronics (Danfysik model 518).

For a test measurement, the BPM was installed at 14 m from the ECR ion source. Figure 3 shows a typical profile of He^{2+} beam for X axis (top) and for Y axis (bottom). The beam width (HWHM) was 4 mm for X axis and 5 mm for Y axis. The beam position for Y axis is located at a distance of 9 mm from the center of the beam line, which is shown by the solid line in Fig. 3. It clearly demonstrates that the BPM tested in this study is useful for monitoring the beam profile as well as the beam position in the injection line of the 930 cyclotron.

References

1) Yamazaki A., Fujita M., Tanaka E., Shinozuka T., Yokoi T., Ozawa T., Tanaka H., Rev. Sci. Instrum. **73** (2002) 589.

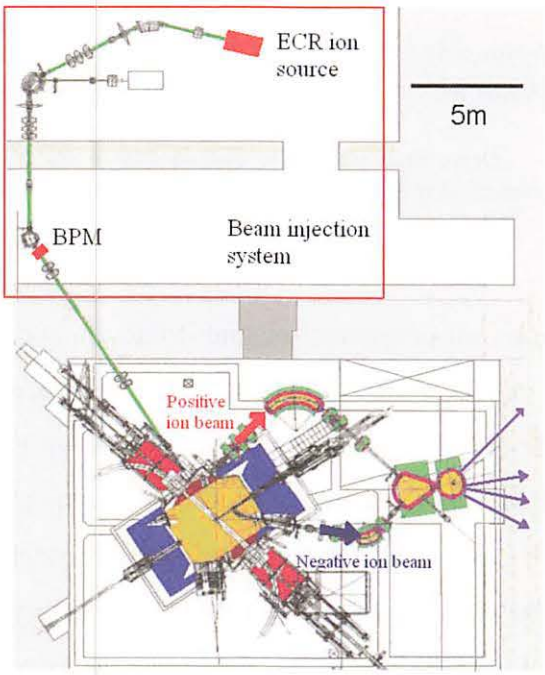

Figure 1. Schematic layout of the beam injection line.

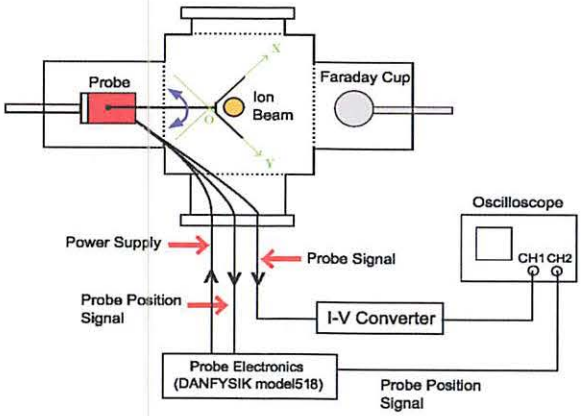

Figure 2. Schematic view of the BPM.

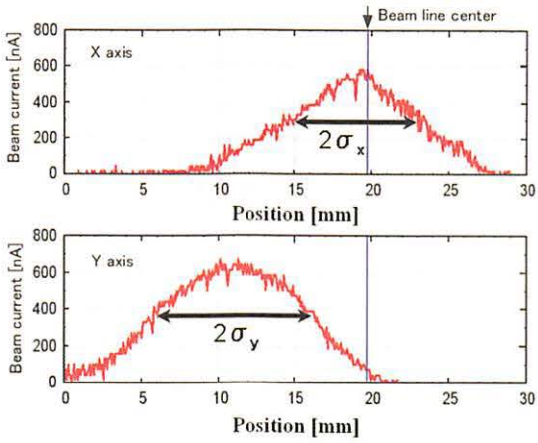

Figure 3. Beam profile for X axis (top) and for Y axis (bottom).

II. 3. A New Large RF Carpet Electrode System for RFIGISOL

Miyashita Y.[1], Hoshino S.[1], Ishida T.[2], Nagano T.[1], Ouchi H.[1], Ohguma M.[1], Suzuki T.[1], Sato N.[1], Shimada K.[2], Tateoka M.[1], Ukai M.[2], Wakui T.[2], Yamashita W.[1], Yamazaki A.[2] and Shinozuka T.[2]

[1]*Department of Physics, Tohoku University*
[2]*Cyclotron and Radioisotope center, Tohoku University*

The astrophysical r-process plays an important role for explaining the mechanism of the nuclear synthesis. The systematic studies of masses, lifetimes and neutron emission rates of neutron rich nuclei are necessary for astrophysical calculations concerning the r-process scenario. It is difficult to obtain fundamental properties of neutron rich nuclei around the r-process scenario because of shorter half-lives and smaller production cross sections. One of the techniques to obtain such neutron rich nuclei is radio frequency ion guide isotope separator on-line (RFIGISOL) technique.

The neutron rich nuclei are produced by proton induced fission reactions in an RFIGISOL chamber. The produced nuclei are thermalized with He buffer gas in the large volume gas cell of the chamber. Then the thermalized nuclei are speedily guided to the mass separator by the DC and RF electric fields.

The key point of this system is sophisticate electrode configurations for electric field guiding in the gas cell[1,2]. The DC and RF electrodes comprise the 80 ring electrodes on the cylindrical wall of gas cell (cylindrical electrode) and the 364 concentric ring electrodes around the exit hole of the gas cell (RF carpet electrode). Both are made of the flexible printed circuit boards of 50 μm Kapton, shown in Fig. 1 and Fig. 2. The cylindrical electrode is 320 mm long and 220 mm in diameter. A diameter of the RF carpet electrode is 220 mm and an exit hole of 1.2 mm diameter for extraction is bored at the center of the RF carpet electrode.

Using the RFIGISOL system, $^{112}Rh^{1+}$ ions ($T_{1/2}$ = 6.8 sec. for the high spin state and $T_{1/2}$ = 3.8 sec. for the 1+ state) are extracted and mass-separated as test ions of

short-lived nuclei. Figure 3 shows the mass-separated yield of ^{112}Rh as function of applied RF voltage. It is pointed that no RF electric field makes any yield. The mass-separated yield is increasing in accordance with the applied RF voltage. Higher RF voltages are required to obtain higher mass-separated yields. As test experiments, we have obtained mass-separated $^{112}Rh^{1+}$ ions of ~ 4000 /sec at 1 μA incident proton beam. Neutron rich nuclei for the systematic studies of masses, lifetimes and neutron emission rates are now available using RFIGISOL system.

References

1) Sonoda T., et al., Nucl. Instr. And Meth. B**245** (2007) 295.
2) Miyashita Y., et al., Proceedings of the 15th International Conference on Electromagnetic Isotope Separators and Techniques Related to their Applications, Deauville, 2007.

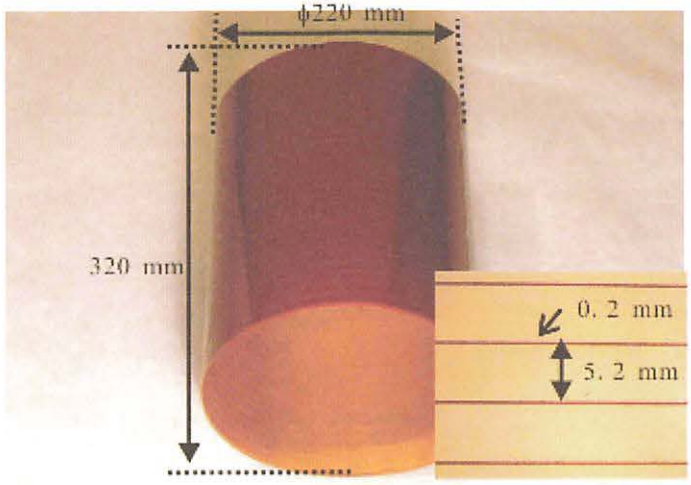

Figure 1. Cylindrical electrodes made of a flexible printed circuit board.

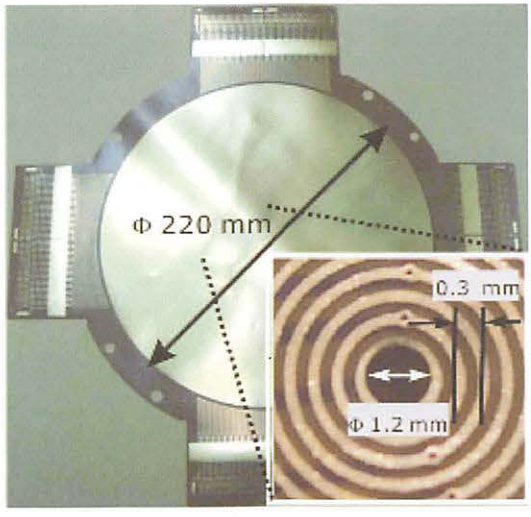

Figure 2. RF carpet electrodes made of a flexible printed circuit board.

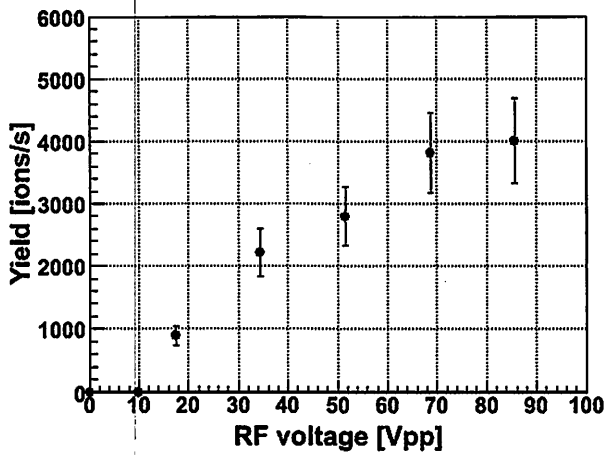

Figure 3. Mass-separated yields of 112Rh as function of applied RF voltage.

II. 4. Study of the NaI(Tl) Calorimeters for ESPRI

Matsuda Y.[1], Sakaguchi H.[2], Takeda H.[3], Terashima S.[3], Zenihiro J.[4], Itoh M.[5], Ozeki K.[5], and Kobayashi T.[1]

[1]*Department of Physics, Tohoku University*
[2]*Department of Physics, Miyazaki University*
[3]*RIKEN*
[4]*Department of Applied Physics, Kyoto University*
[5] *Cyclotron and Radioisotope Center, Tohoku University*

In order to determine density distributions of unstable nuclei, we have developed a recoil proton detection system to measure **E**lastic **S**cattering of **P**rotons with **RI** beams (ESPRI)[1]. Using this system, a missing mass distribution of the H(X,p) reactions is constructed and the angular distribution of elastically recoiled protons is measured. With a 300 MeV/u RI beam, it covers a horizontal angular range of 68 deg. to 80 deg. in the laboratory frame, which corresponds to an energy range of 20 MeV to 120 MeV.

We selected a NaI(Tl) scintillating counter as a calorimeter of recoil protons to conform with the above noted situation and achieve an energy resolution of around 200 keV (rms) at 100 MeV, which corresponds the missing mass resolution of around 300 keV (rms). And fourteen single-crystals were manufactured and housed in shield boxes. The volume of the crystal is 18 inches wide, 2 inches thick and 2inches high. The entrance window is aluminum with 100 micrometers thickness. Two photomultiplier tubes (PMT, Hamamatsu R1307) are mounted on the both sides of the 2inchs square, respectively. We have evaluated whether all the rods satisfy the required resolution.

At first, the performance was studied with a 12 MeV proton beam at Tandem Van de Graff Accelerator Laboratory at Kyoto University[2]. When the geometric mean value of read-out charge of two PMTs was used as relative proton energy, the energy resolution was about 0.6% (rms) at every irradiated point but the mean relatively fluctuated around 5% among these points. Therefore scintillating photons turned out not to be attenuated as an exponential function of a length from scintillating position to PMT. It can't become negligible with recoil energy going up to 100 MeV.

Next, the energy resolution and fluctuation at higher energy was studied using the C4 beam line at CYRIC in December 2005[2,3]. Four rods were irradiated with a 77.6 MeV proton faint beam. The beam intensity was around 200 Hz. For each rod, the energy resolution was about 0.2% (rms) but the fluctuation of the mean was around 6% and its functional shape was different from the others. So each of outputs from PMTs turned out to need to be corrected individually, especially at higher energy.

Therefore a further study of the fluctuation for all the rods was performed at CYRIC in February 2007. The beam energy and arrangement of the setup was the same as before. In this experiment, following topics were mainly studied.

1) Time dependence : The fluctuation was checked against the previous measurement. In both measurements, following circuits were used. Anode outputs from PMTs were converted into voltage pulses with preamplifiers. These were further amplified with spectroscopic amplifiers. (Ortec 671), then fed to peak hold ADCs (Hoshin C008). Figure 1 shows the fluctuation as a function of the irradiated position. The latest data were not consistent with the previous. That is to say, the inclination of fluctuation changes with the passage of time. Because the energy resolution was almost unchanged, we can use these rods on condition that correction functions of fluctuation get every experiment.

2) Range dependence : The dependence of fluctuation on proton range was examined. Beam energy was varied from 20.0 to 77.6 MeV, which corresponds to the range of 2 mm to 23 mm in NaI crystal, using a degrader installed in the beam line. During this measurement, Ortec 671 and Hoshin C008 were exchanged for Caen N568B and V785, respectively. Figure 2 shows the dependence of fluctuation on beam energy. Each fluctuation was consistent with the others. Therefore we can take into no consideration the proton range to get correction functions of fluctuation.

In summary, we confirmed that the manufactured rod could satisfy the required resolution throughout its active area and the required energy range to correct the fluctuation for the long side of the rod every experiment. With our detection system including these rods, we are measuring proton elastic scattering of ^{9}C and ^{20}O at NIRS-HIMAC.

References

1) Terashima S., et al., RIKEN Accel. Prog. Rep. **40** (2007), in press.
2) Zenihiro J., et al., CYRIC Annual Report (2005) 20.
3) Itoh M., et al., CYRIC Annual Report (2005) 18.

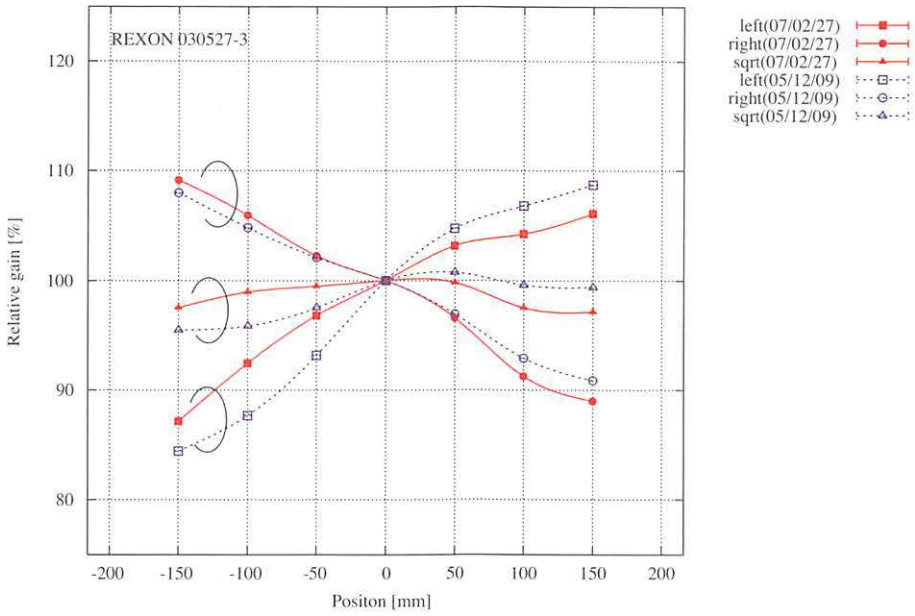

Figure1. Relative gain fluctuation. Closed and open markers are the latest and previous data, respectively. Squares and circles are relative read-out charge of one side of two PMTs, respectively. Triangles are relative values of the geometric mean of squares and circles. All the cubic spline curves are to guide the eye.

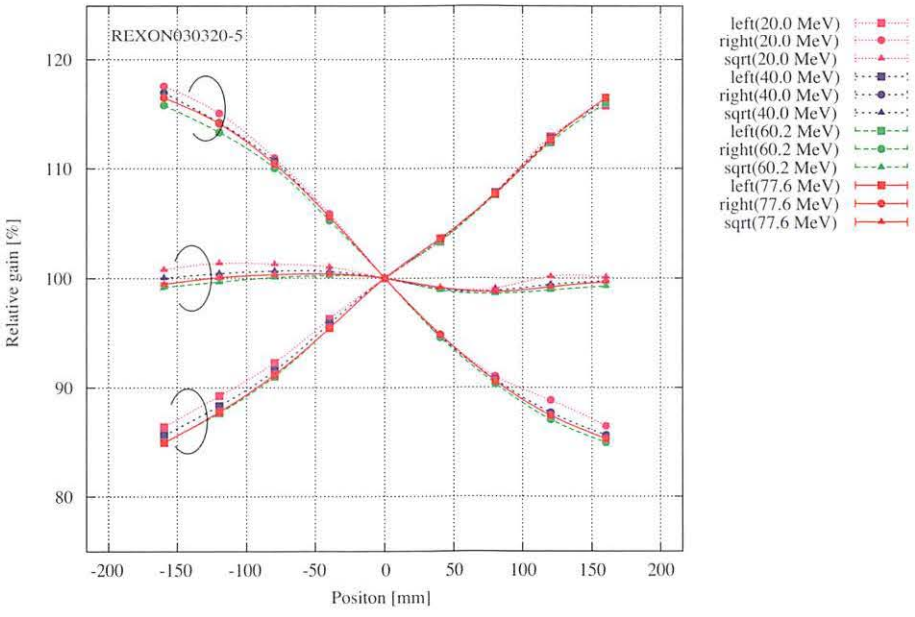

Figure 2. Dependence of relative gain fluctuation on proton energy. Red, green, blue and purple markers are data at 20.0, 40.0, 60.2, 77.6 MeV, respectively. And each maker at each energy and curves are the same as Fig. 1.

III. NUCLEAR ENGINEERING

III. 1. Effect of Helium on Mechanical Properties of ODS Ferritic/Martensitic Steels for Fusion Applications

Hasegawa A.[1], Ejiri M.[1], Nogami S.[1], Satou M.[1], Abe K.[1]
Kimura A.[2], and Jitsukawa S.[3]

[1]Department of Quantum Science and Energy Engineering, Tohoku University
[2]Institute of Advanced Energy, Kyoto University
[3]Japan Atomic Energy Agency

Introduction

The reduced activation ferritic/martensitic steels are one of the candidate structural materials for fusion reactor[1]. In the fusion reactor environment, 14 MeV neutron irradiation might produce large amount of displacement damage and transmutant helium (He) atoms in structural materials. For instance, the displacement damage will be 100 dpa and He concentration will be 1000 appm in a ferritic/martensitic steel after 10 MW/m^2 neutron wall loading.

The displacement damage might cause an increase of strength (irradiation hardening) at temperature below 400°C and the irradiation hardening might reduce facture toughness, which includes a ductile brittle transient temperature (DBTT) shift to higher temperatures[1]. It is well known that He might stabilize a point defect cluster and cause the additional hardening at lower temperature region and the increase of swelling at higher temperature region. He atoms in material might diffuse to form He bubbles at the preexisting grain boundary during higher temperature irradiation and tend to change the fracture mode from the transgranular fracture to the intergranular fracture. The previous study[2] in our group showed that the irradiation hardening, increment of the DBTT and the intergranular fracture of the 8Cr-2W ferritic/martensitic steel (F82H by JAEA) due to He implantation up to 1000 appm at 550°C using the Cyclotron accelerator of CYRIC.

The oxide dispersion strengthened (ODS) ferritic/martensitic steels were recently developed[3], which consists of fine grains and ultra fine dispersed oxides. The ODS ferritic/martensitic steels are expected to have higher strength under high temperature neutron irradiation than the conventional (non-ODS) ferritic/martensitic steels described

above because the grain boundaries and the fine dispersed oxides in this material might effectively behave as a trapping site and a sink for defects including He[4-6].

The objective of this study is to investigate the effect of He at high temperature on mechanical properties of the ODS ferritic/martensitic steel using high energy α-particle irradiation by the Cyclotron accelerator.

Experimental

The material used in this study was the ODS 9Cr-2W ferritic/martensitic steel developed by Japan Atomic Energy Agency (JAEA), which was fabricated by a mechanical alloying (MA) process. The chemical composition of this material is shown in Table 1. This material includes high density ultra fine oxides, which were produced from original Y_2O_3 powders during the MA process and the following heat treatment (1050°C x 1 h for tempering and 800°C x 1h for annealing). Miniaturized Charpy V notch (CVN) specimen for the Charpy impact test was machined with the dimension of 1.5 mm x 1.5 mm x 20 mm and the notch geometry of 0.3 mm in notch depth, 0.08 mm in notch root radius and 30° in notch angle. Figure 1 shows the CVN specimen shape and geometry.

He-ion implantation was performed using 50 MeV α-particles from the AVF cyclotron of CYRIC of Tohoku University. The projected range of 50 MeV He-ions in a Fe-9Cr steel was calculated to be about 400 μm by TRIM code[7]. The tandem type energy degrader system consisting of 2 rotating wheels was used to obtain the uniform depth distribution of He atoms in specimens[8]. The calculated depth distribution of He concentration and displacement damage is shown in figure 2. The nominal He concentration was about 1000 appm. The displacement damage was about 0.37 dpa at the specimen surface and 0.28dpa in average. The implantation temperature was 550°C +/−10°C, which was measured using thermocouples during the implantation test.

The Vickers hardness measurement, the Charpy impact property evaluation, and the fracture surface analysis after the impact test was carried out after He implantation. The Vickers hardness was measured using a Vickers hardness tester at Radio Isotope Laboratory of Tohoku University. The indentation load and dwell time was 200 gf and 15 sec, respectively. The Charpy impact test was carried out using an instrumented Charpy impact testing equipment at the Hot Laboratory of International Research Center for Nuclear Materials Science of Tohoku University. The test temperature ranged from −120°C to room temperature. The fracture surface of the CVN specimens after the impact test was observed using a scanning electron microscope (SEM) at the Hot Laboratory of

International Research Center for Nuclear Materials Science of Tohoku University.

Results and Discussion

Figure 3 shows the Vickers hardness of the ODS 9Cr-2W steel and the conventional 8Cr-2W steel (F82H) in the previous work[2]. The hardness of the as-received ODS 9Cr-2W steel before He implantation (Hv = 385) was about 55% larger than that of the as-received conventional 8Cr-2W steel (Hv = 248). Almost no change of the hardness in the ODS 9Cr-2W steel due to He implantation at 550°C was observed though the conventional 8Cr-2W steel showed the clear irradiation hardening (ΔHv = +27).

The Charpy impact data for the ODS 9Cr-2W steel and the conventional 8Cr-2W steel in the previous work[2] are shown in Figure 4. The DBTT of the as-received ODS 9Cr-2W steel before He implantation (DBTT = –51°C) was about 54°C higher than that of the as-received conventional 8Cr-2W steel (DBTT = –105°C). The upper shelf of the absorbed energy for the as-received ODS 9Cr-2W steel before He implantation (E_{upper} = 0.5 J) was about 45% lower than that for the as-received conventional 8Cr-2W steel (E_{upper} = 0.9 J), though the lower shelf energies of these two materials were almost the same. Almost no change of the DBTT in the ODS 9Cr-2W steel due to He implantation at 550°C was observed though the conventional 8Cr-2W steel showed the clear increment of the DBTT (ΔDBTT = +70°C).

The typical fracture surfaces for the He-implanted Charpy impact specimen of the ODS 9Cr-2W steel tested at –120°C and the conventional 8Cr-2W steel tested at –60°C in the previous work[2] are shown in Figure 5. Fracture mode for the He-implanted region and the He-unimplanted region of the ODS 9Cr-2W steel was cleavage fracture, though the He-implanted region of the conventional 8Cr-2W steel showed an intergranular fracture.

Almost no irradiation hardening, no increment of the DBTT and no intergranular fracture due to He implantation at 550°C were observed for the ODS 9Cr-2W steel though the conventional 8Cr-2W steel showed them. The ODS 9Cr-2W steel consists of fine grains and ultra fine dispersed oxides. Therefore, almost no embrittlement due to He implantation occurred since the grain boundaries and the fines dispersed oxides in this material are considered to effectively behave as a He-trapping site and sink of He atoms. Based on these results in this study, suppression of the irradiation hardening (increment of the yield strength) and the grain boundary degradation due to transmutant He during high temperature neutron irradiation can be expected for the ODS 9Cr-2W steel in comparison with the conventional 8Cr-2W steel.

Summary

Effect of transmutant He on mechanical properties of the ODS 9Cr-2W ferritic/martensitic steel was evaluated using high energy α-particle irradiation by the Cyclotron accelerator of CYRIC and was compared with that of the conventional 8Cr-2W ferritic/martensitic steel. The following results were obtained.

1) Almost no irradiation hardening of the ODS 9Cr-2W steel due to He implantation at 550°C was clearly observed.
2) Almost no change of the DBTT in the ODS 9Cr-2W steel due to He implantation at 550°C was observed though the conventional 8Cr-2W steel showed the clear increment of the DBTT (ΔDBTT = +70°C).
3) The He-implanted region of the ODS 9Cr-2W steel showed a cleavage fracture, though that of the conventional 8Cr-2W steel showed an intergranular fracture.

Acknowledgement

The authors are grateful to the staffs of CYRIC of Tohoku University relating to the accelerator operation and the irradiation experiments. This work was partly supported by the JUPITER-II (Japan-USA Program of Irradiation Testing for Fusion Research II) program.

References

1) Baluc N., Gelles D.S., Jitsukawa S., Kimura A., Klueh R.L., Odette G.R., van der Schaaf B., Jinnan Yu., J. Nucl. Mater. **367-370** (2007) 33.
2) Hasegawa A., Suzuki A., Tanaka K., Satou M., Abe K., Jitsukawa S., CYRIC Annual Report 2004, 27.
3) Ukai S., Fujiwara M., J. Nucl. Mater. **307-311** (2002) 749.
4) Klueh R.L., Maziasz P.J., Kim I.S., Heatherly L., Hoelzer D.T., Hashimoto N., Kenik E.A., Miyahara K., J. Nucl. Mater. **307-311** (2002) 773.
5) Schaeublin R., Leguey T., Spätig P., Baluc N., Victoria M., J. Nucl. Mater. **307-311** (2002) 778.
6) Goshchitskii B.N., Sagaradze V.V., Shalaev V.I., Arbuzov V.L., Tian Y., Qun W., Jiguang S., J. Nucl. Mater. **307-311** (2002) 783.
7) Biersack J.P., Ziegler J.F., TRIM85 Program, IBM Corp., Yorktown, NY, 1985.
8) Hasegawa A., Wakabayashi E., Tanaka K., Abe K., Jitsukawa S., CYRIC Annual Report 2002, 34.

Table 1. The chemical composition of the ODS ferritic steel (unit: wt.%).

C	Si	Mn	Cr	W	N	Ti	Y	Y_2O_3	Fe
0.14	0.048	0.05	8.67	1.96	0.017	0.23	0.27	0.34	Bal.

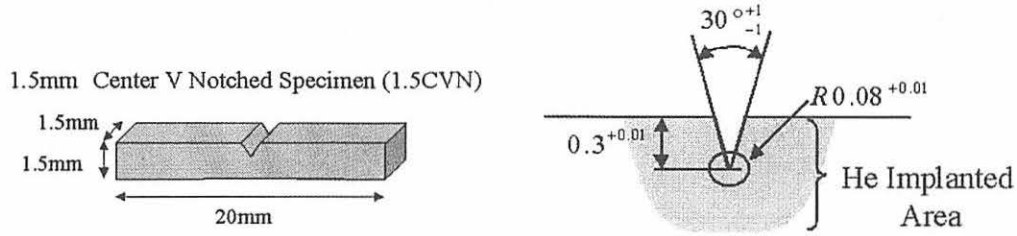

Figure 1. The shape and geometry of the miniaturized Charpy V notch (CVN) specimen.

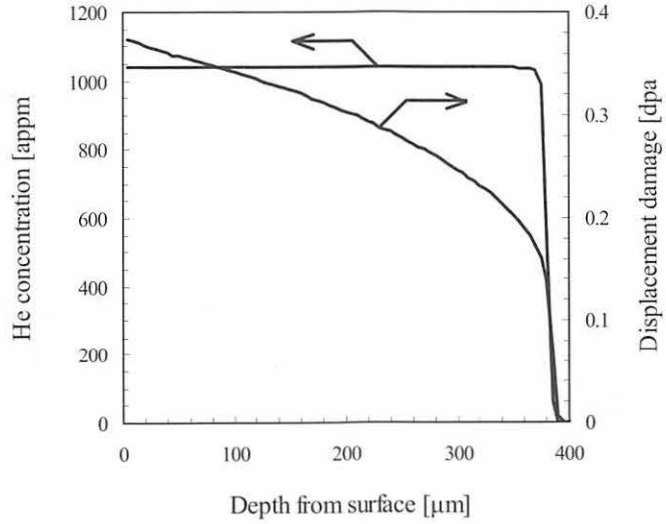

Figure 2. The calculated depth distribution of He concentration and displacement damage in the ODS 9Cr-2W ferritic/martensitic steel.

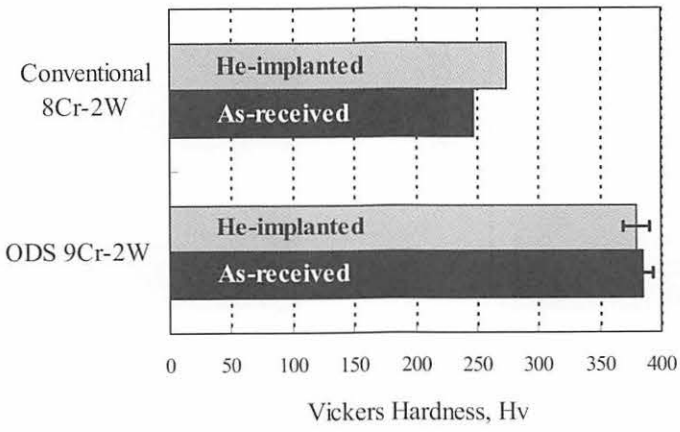

Figure 3. The Vickers hardness of the ODS 9Cr-2W steel and the conventional 8Cr-2W steel (F82H) in the previous work[2].

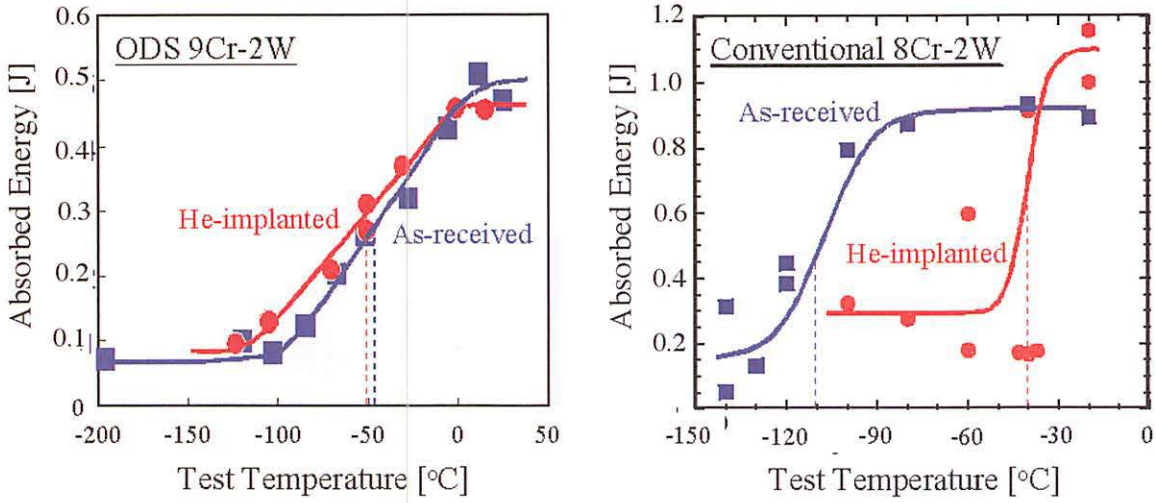

Figure 4. The Charpy impact data for the ODS 9Cr-2W steel and the conventional 8Cr-2W steel in the previous work[2].

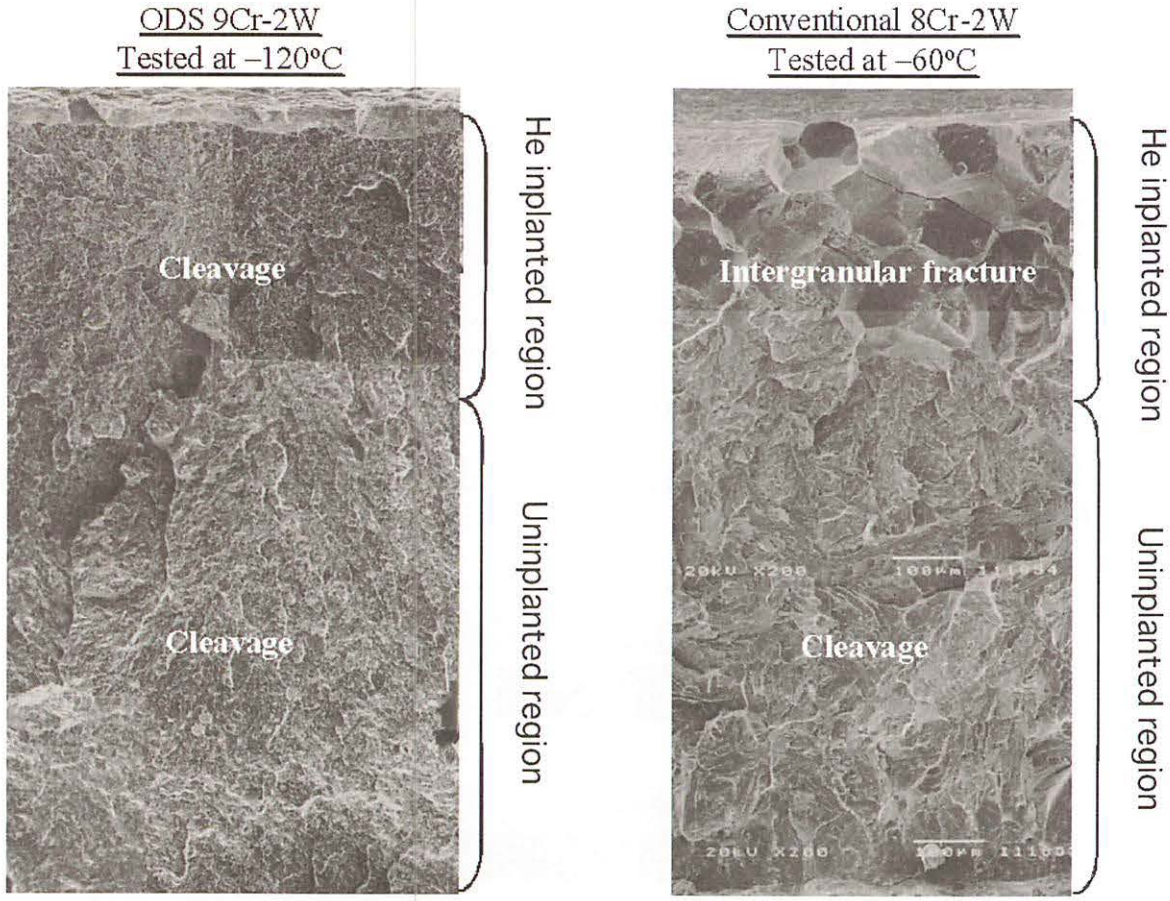

Figure 5. The typical fracture surfaces for the He-implanted Charpy impact specimen of the ODS 9Cr-2W steel tested at –120°C and the conventional 8Cr-2W steel tested at –60°C in the previous work[2].

III. 2. Evaluation of Helium Effect on Candidate Structural Materials for Next Generation Long-life Nuclear Plant

Hasegawa A.[1], Nogami S.[1], Satou M.[1], Wakai E.[2], and Aoto K.[2]

[1]Department of Quantum Science and Energy Engineering, Tohoku University
[2]Japan Atomic Energy Agency

Introduction

For development of the next generation long-life nuclear plant, precise prediction of the irradiation damage to reactor vessel and in-core component during operation is necessary. This study focuses on the developing the index for evaluation of the irradiation damage for the candidate structural materials of the next generation long-life nuclear plant such as SUS304 steel, SUS316FR steel and 12Cr steel (HCM12A), which can be applied to reactor design method considering irradiation environment effect. This study also focuses on the developing the non-destructive inspection technique for precise understanding of irradiation damage progress during operation based on the index.

The amount of generated helium (He) is recognized as one of the promising index in this study. The database of mechanical property change for those materials due to He implantation should be established in order to verify whether He generation amount is adequate as the index for evaluation of the irradiation damage. Therefore, short time mechanical properties such as the tensile property (tensile strength and yield stress) and the hardness were evaluated in this year in order to clarify the relation between He and their changes. Microstructure observation was also performed for analysis of the microstructure change due to He implantation.

Experimental

(1) He Implantation using Cyclotron

Material in this study is the 316FR steel and the HCM12A steel, which are the candidate structural material for next generation nuclear plants. The chemical composition of these materials is shown in table 1. The specimen shape was a miniaturized tensile

specimen and a rectangular specimen with geometry of 5 mm x 16 mm x 0.3 mm. The specimen surface was mechanically and electrically polished into mirror state.

The He implantation test was carried out using the AVF Cyclotron accelerator of Cyclotron and Radioisotope Center of Tohoku University. The implanted particle, implantation temperature and He concentration were 50 MeV He^{2+} ion, about 500°C and about 1, 10, 30 appm, respectively. Helium was uniformly implanted from the specimen surface to about 400 μm in thickness by using a rotating energy degrader consisting of Al foils. Figure 1 shows the depth distribution of He concentration and displacement damage in the specimen calculated by SRIM code. The displacement damage in an iron produced by 50 MeV He^{2+} ion was about 2 x 10^{-4} dpa per 1 appm-He. The implantation temperature was measured using a thermocouple during implantation test, which was spot-welded to one of the implanted specimens.

(2) Tensile Test

Tensile test for the He implanted miniaturized tensile specimen was performed using an Instron-type multi-purpose testing machine (INTESCO Co., Ltd.) at Radio Isotope Laboratory of Tohoku University. The test temperature, test environment and strain rate were about 550°C, vacuum below 1x10^{-3} Pa and about 6.7 x 10^{-4} s^{-1}, respectively. The number of the test was 2 for unimplanted specimen and the He implanted specimen up to 1 and 10 appm and 1 for the He implanted specimen up to 30 appm.

(3) Hardness Measurement

The Vickers hardness measurement for the He implanted miniaturized tensile specimen and rectangular specimen was performed using a Vickers hardness tester (Shimadzu Corp., Micro Hardness Tester type M) at Radio Isotope Laboratory of Tohoku University. The number of the test was 5~10 for each specimen. The test temperature, indentation load and dwell time was room temperature, 200 gf and 15 sec, respectively.

(4) Microstructure Observation by TEM

Microstructural observation for the He implanted specimen was performed using a transmission electron microscope (TEM, JEOL Ltd., JEM-2000FX) at International Research Center for Nuclear Materials Science of Tohoku University. The specimen tested was the He implanted miniaturized tensile specimen of the 316FR steel up to about 1 appm. Thin foil preparation for TEM observation was performed by electro-polishing

using electrolyte solution with acetic acid and perchloric acid.

Results and Discussion

(1) He Implantation using Cyclotron

Table 2 shows the summary of the He implantation test in this year. The He implantation at 550°C up to about 1, 10 and 30 appm has successfully finished for the 33 specimens including 16 miniaturized tensile ones and 17 rectangular ones. The rectangular specimens were provided to JAEA for Positron Annihilation Lifetime Spectroscopy.

Table 3 shows the summary of the comparison between expected He concentration of the He implantation test and the He concentration analyzed by NFD (Nippon Nuclear Fuel Development Co., Ltd.). The latter analysis is the measurement of He gas released from the He implanted specimen during melting it using a quadrupole mass spectrometer. Almost all the implanted He atoms can be detected using this method. The results indicated that the expected He concentration was achieved with accuracy of +/– 40% by using the Cyclotron. This error might occur due to the scatter of He-ion current and He-ion implanted region.

(2) Tensile Test

Figure 2, table 4, figure 3, figure 4, figure 5, figure 6 and figure 7 show the stress-strain curves for the He implanted miniaturized tensile specimen, the summary of the yield stress, tensile strength, uniform elongation, total elongation and reduction in area, the dependence of the yield stress on the He concentration, the dependence of the tensile strength on the He concentration, the dependence of the uniform elongation on the He concentration, the dependence of the total elongation on the He concentration and the dependence of the reduction in area on the He concentration, respectively. About 15% reduction of the tensile strength was observed due to He implantation up to about 1 appm in comparison with the unimplanted value for both steels. The tensile strength of the He implanted specimen up to about 10 and 30 appm was almost the same as that of the He implanted specimen up to about 1 appm. About 20% increment of the yield stress due to the He implantation up to about 1 appm, about 40% reduction due to about 10 appm implantation and about 10% reduction due to about 30 appm implantation in comparison with the unimplanted value were observed for the 316FR steel. While, about 20% reduction of the yield stress due to the He implantation up to about 1 appm, about 24%

reduction due to about 10 appm implantation and about 16% reduction due to about 30 appm implantation in comparison with the unimplanted value were observed for the HCM12A steel.

(3) Hardness Measurement

The summary of the Vickers hardness and the dependence of the Vickers hardness on the He concentration for the He implanted miniaturized tensile specimen were shown in table 5 and figure 8, respectively. The results indicated that the hardness change due to He implantation was very small for both steels. About 20~30 Hv increment in the hardness was observed even after about 30 appm implantation.

(4) Microstructure Observation by TEM

The microstructure of the He implanted 316FR steel up to about 1 appm is shown in figure 9. The peculiar microstructure of He implanted materials such as He bubble was not observed though dislocation was observed in matrix. Almost no difference of the microstructure was observed between the unimplanted specimen and He implanted one up to about 1 appm. The thermal desorption spectrometry indicated that most amounts of the implanted He atoms might remain in the specimen after annealing up to 1300°C. Thus, most amounts of the implanted He atoms might exist in the matrix and grain boundary of the specimen.

Summary

Evaluation of the short time mechanical properties such as the tensile property and the hardness and observation of microstructure for He implanted materials (316FR and HCM12A steel) using Cyclotron was carried out in order to clarify the relation between He and their changes due to He implantation. The database of these properties was established for the He implanted specimen up to about 1, 10, 30 appm at the implantation temperature of 550°C in this year.

Acknowledgement

Present study is the result of R&D Project on Irradiation Damage Management Technology for Structural Materials of Long-life Nuclear Plant entrusted to Japan Atomic Energy Agency (JAEA) by the Ministry of Education, Culture, Sports, Science and Technology of Japan (MEXT). The authors are grateful to the staffs of CYRIC of Tohoku

University relating to the accelerator operation and the irradiation experiments.

Table 1. The chemical composition of the 316FR steel and the HCM12A steel.

	Fe	C	Si	Mn	P	S	Cu	Ni	W	Cr	Mo	V	Nb	N
316FR	Bal.	0.01	0.59	0.84	0.026	0.003	0.26	11.19	-	16.87	2.23	0.08	-	0.08
HCM12A	Bal.	0.11	0.27	0.64	0.016	0.002	1.02	0.39	1.89	10.83	0.30	0.19	0.054	0.063

Table 2. The summary of the He implantation test in this year.

Material	Specimen Shape	Number of Specimen	He Concentration [appm]	Implantation Temperature [°C]
316FR	Rectangular	4	1	550±10
HCM12A	Rectangular	4	1	550±10
316FR	Tensile	3	1	550±10
HCM12A	Tensile	3	1	550±10
316FR	Rectangular	4	10	550±10
HCM12A	Rectangular	3	10	550±10
316FR	Tensile	4	10	550±10
HCM12A	Tensile	4	10	550±10
316FR	Rectangular	1	30	550±10
HCM12A	Rectangular	1	30	550±10
16FR	Tensile	1	30	550±10
HCM12A	Tensile	1	30	550±10

Table 3. The summary of the comparison between expected He concentration of the He implantation test and the He concentration analyzed by NFD.

Material	Expected He concentration	He concentration analyzed by NFD	
	[appm]	[atom]	[appm]
316FR	1	2.53×10^{15}	1
	10	2.63×10^{16}	14

Table 4. The summary of the yield stress, tensile strength, uniform elongation, total elongation and reduction in area.

	He Concentration [appm]	Yield Stress [MPa]	Tensile Strength [MPa]	Uniform Elongation [%]	Total Elongation [%]	Reduction in area [%]
SUS316FR	0	139.8	368.0	31.6	34.8	99.5
	1	171.8	342.0	20.9	23.1	96.7
	10	91.8	354.7	40.8	46.1	95.3
	30	134.7	379.8	35.3	40.0	97.0
HCM12A	0	405.0	436.8	3.1	16.0	66.4
	1	349.7	378.5	3.6	19.8	52.8
	10	308.9	363.9	3.0	24.6	65.7
	30	340.2	384.7	4.0	21.0	61.1

Table 5. The summary of the Vickers hardness.

Material	He Concentration [appm]	Vickers Hardness, Hv	
		Average	Standard Deviation
316FR	0	172.7	16.3
	1	176.3	8.8
	10	169.0	17.2
	30	188.2	7.8
HCM12A	0	259.5	9.6
	1	279.1	14.5
	10	264.4	8.5
	30	289.6	6.9

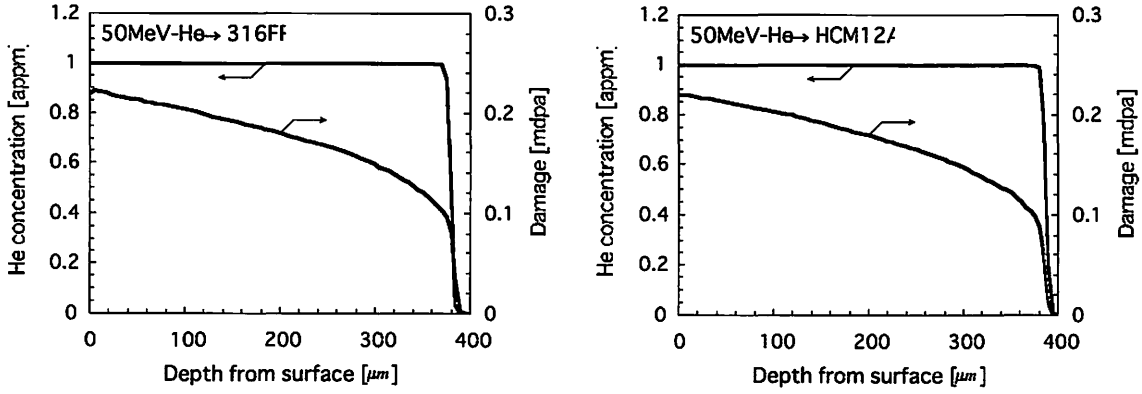

Figure 1. The depth distribution of He concentration and displacement damage in the 316FR steel and the HCM12A steel calculated by SRIM code.

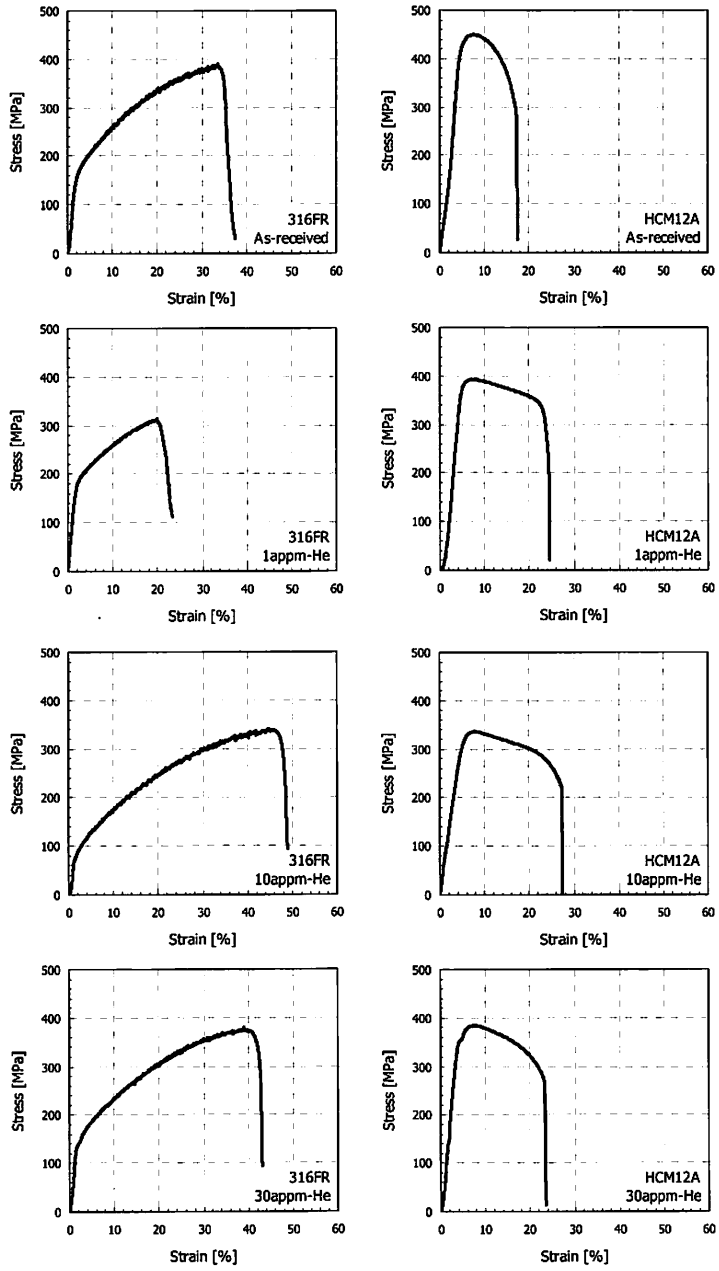

Figure 2. The stress-strain curves for the He implanted miniaturized tensile specimen.

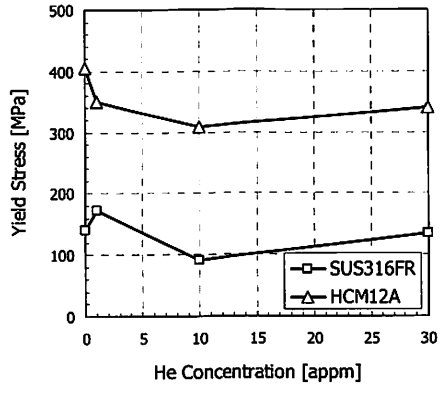

Figure 3. The dependence of the yield stress on the He concentration.

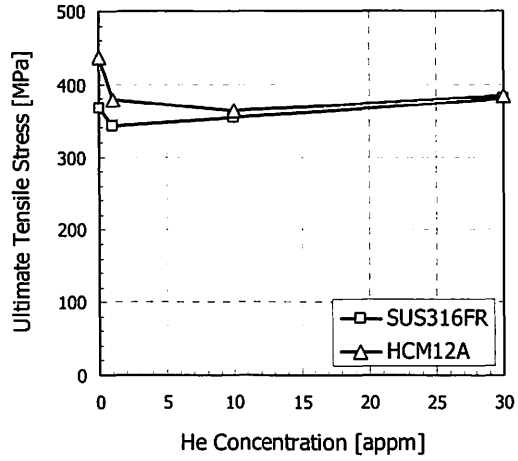

Figure 4. The dependence of the tensile strength on the He concentration.

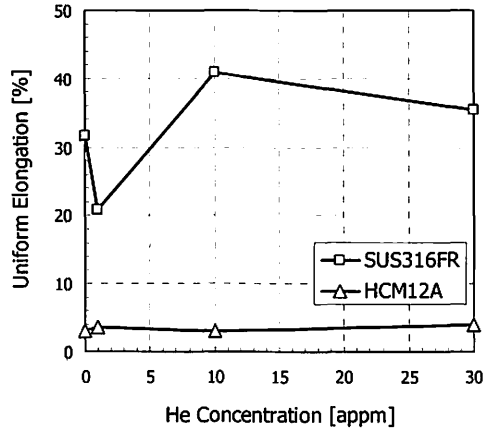

Figure 5. The dependence of the uniform elongation on the He concentration.

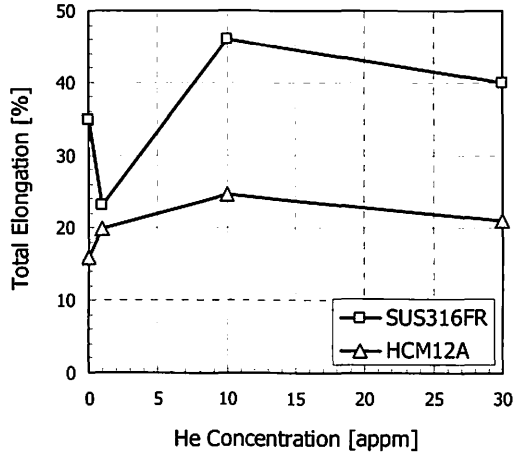

Figure 6. The dependence of the total elongation on the He concentration.

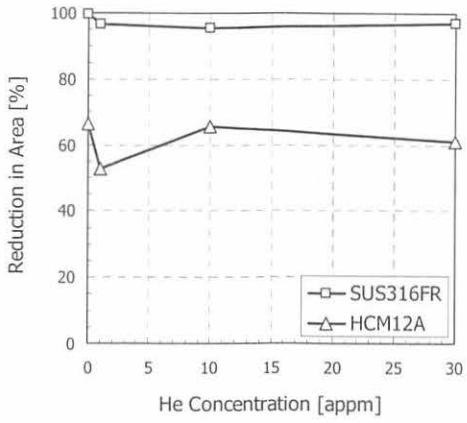

Figure 7. The dependence of the reduction in area on the He concentration.

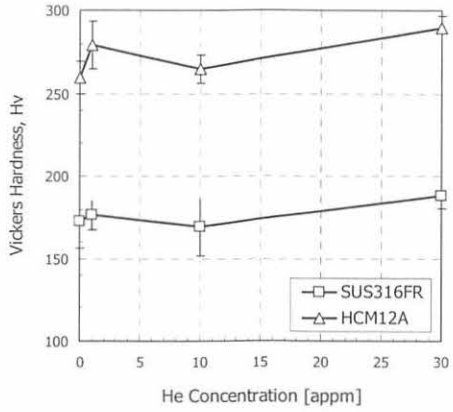

Figure 8. The dependence of the Vickers hardness on the He concentration for the He implanted miniaturized tensile specimen.

Figure 9. The microstructure of the He implanted 316FR steel up to about 1 appm.

III. 3. Development of a High Count Rate Gaseous Neutron Detector

Nakhostin M. and Baba M.

Cyclotron and Radioisotope Center, Tohoku University

We are developing a high-rate neutron detector for use at high-flux neutron facilities. The detector concept is based on the combination of a ^{6}Li solid neutron converter with a micromegas[1] detector operating at low gas pressures.

Figure 1 shows a schematic representation of the detector. The detector comprises an ionization and drift region of depth 7 mm and a single avalanche region 500 μm deep. The two regions are separated by a solid stainless steel wire mesh with 30 μm diameter and a pitch of 50 μm. The anode plane is made of a thin nickel foil (20 μm thick) and the drift electrode is defined by a 50 μm thick aluminum foil. A layer of LiF enriched to 95% by ^{6}Li was deposited by vacuum evaporation on the inside face of the drift electrode. Two glass epoxy spacers maintain two gaps between the three electrodes. The various elements of the detector are placed in a gas-tight aluminum chamber equipped with a thin aluminum window. The detector active area is 5× 5 cm^2.

The detector is operated at low gas pressures (5-50 Torr). The low-pressure operation enables to have high-count rate capability with relatively larger amplifications gaps (500μm) compared to the standard micromegas detectors operating at normal pressures. The gas pressure is maintained using a mass flow controller and a mechanical pump.

Figure 2 shows signals recorded for neutron detection in two different operating conditions. In Fig. 2a, voltage of the drift electrode (HV_2) is slightly higher than that of the wire mesh plane (HV_1) so that the electron multiplication is limited to the amplification gap. The signal duration is very short ~ 500 ns. This confirms that the detector enables high counting rates. When the electric field in the first stage is further increased the drift velocity of primary electrons increases and the first gap operates at some gains. In this case, a sharp component due to electrons contribution clearly appears and the signal duration is further shortened (~ 250ns). This electron component can be used for timing

applications.

An example of the detector pulse height distribution, obtained with a ^{252}Cf neutron source is reported in Fig. 3. The detector was operated at 8 Torr of gas pressure. The shape of the spectra arises from the fact that in each neutron absorption event the amount of energy deposition varies with the type of emerged particle from the converter and the ionization path of the particle in the conversion gap. The low energy continuum in the pulse height distribution is due to the insufficient ionization of some of the triton events as well as the recoil protons emitted from the detector structure.

The preliminary results presented above confirm the detector properties such as high rate capability, fast response and low gamma sensitivity. The latter is due the low-mass structure of the detector resulting from low-pressure operation.

The described properties make the detector a good candidate for neutron detection in various neutron fields that require a high-count rate neutron detector. Nevertheless, more beam test experiments are necessary to optimize the detector performance.

Reference

1) Giomataris Y., et al., Nucl. Instr. Meth. **A 376** (1996) 29.

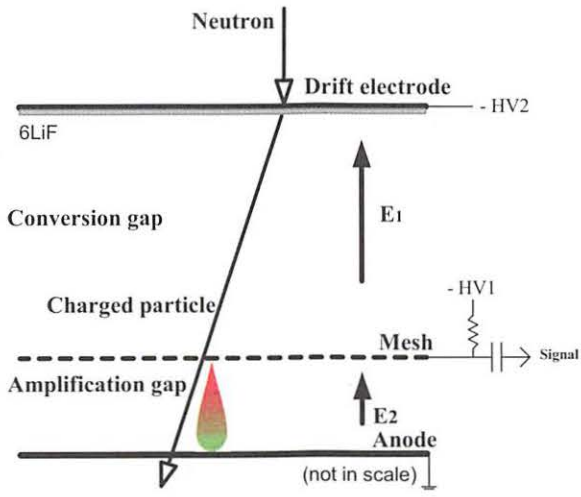

Figure 1. Principle of the detector.

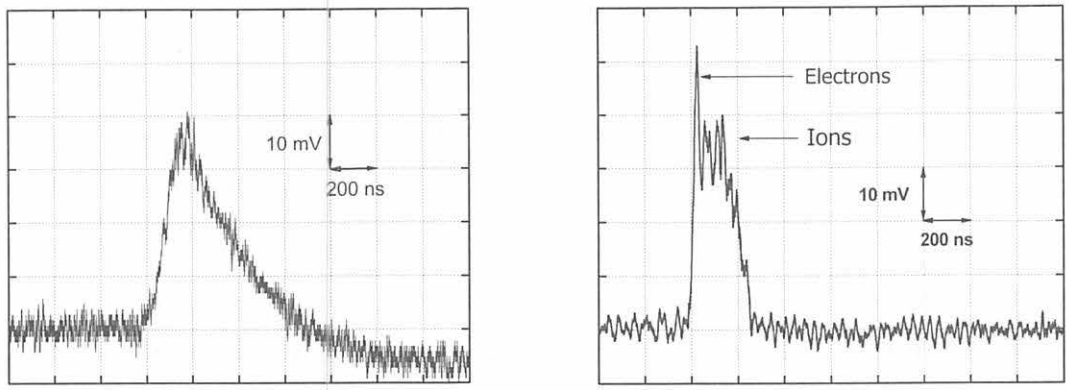

Figure 2. The current signal of double-stage avalanche counter when (a) first gap is in ionization mode and (b) both gaps work at avalanche regime.

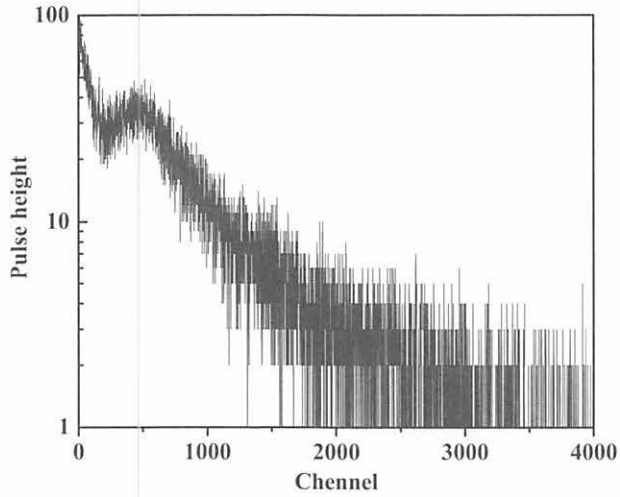

Figure 3. An example of pulse height spectrum.

III. 4. Development of Pileup Separation Method Using Digital Signal Processing

Oishi T. and Baba M

Cyclotron and Radioisotope Center, Tohoku University

High purity germanium (HPGe) detectors are used very widely owing to very high energy resolution. To achieve high energy resolution, usually linear amplifiers are used with long shaping time. However, the long shaping time amplifier leads to a wider output pulse and easily induces overlap between signals, i.e., signal pileup. The pileup causes the spectrum distortion and may mask low intensity gamma-rays.

To avoid the problems pileup rejection methods have been developed which eliminate all the signals overlapped within some duration. In this method, the dead time of the measurement becomes longer at the best improvement of the spectrum. Therefore separation of pileup events instead of rejection is highly desirable which can improve the energy resolution and the count rate concurrently.

We developed new method of pile up separation using the digital signal processing (DSP) technique by newly introducing timing signal which provide information on the number and timing of pulses. The technique could be applied successfully for a HPGe gamma-ray detector. The method can be applied to almost all radiation detectors.

In the DSP technique, signals are digitized by a high speed flash-type analog-to-digital converter and the digitized signal waveform data is stored and processed by a computer. This technique enables us to carry out complex and flexible data processing because the full signal waveform is acquired[1].

We newly introduce "a timing pulse" which is obtained from an amplifier with a short time constant. As shown in Fig. 1, since the output signal of the short time amplifier goes back to the baseline much faster than that of the long shaping time, the probability of pileup occurrence is much lower. Therefore, short shaping time amplifier gives us the correct information about timing and the number of pulses even if the signal of the long shaping time amplifier pile up closely. Furthermore, in the case of HPGe detector, we

observed that almost all signals are described with the same signal shape as shown in Fig. 2. Since the timing and shape of each pulse are known, the pulse height can be easily determined by the linear least square fitting technique. The separated pulses are reconstructed on the basis of the pulse height, timing and pulse shape.

Figure 3 shows an example of pileup event which looks like a single pulse without pileup. It is difficult to recognize as the pile up signal without the TFA signal (circle). Applying the present method, the measured amplifier signal (dot) is separated into two signals (broken line). The sum of the separated pulses agrees with the original amplifier signal very well. Figure 4 shows another example which is a multiple pileup event. The separation can be carried out successfully even in such a case of many pulses involved.

A test experiment was carried out using a source placed in front of the HPGe detector enclosed with lead blocks. Figure 5 shows the energy spectrum of ^{137}Cs: 1) raw data by a conventional MCA method and 2) analyzed one by the separation method. The spectrum from TFA is also shown for reference. They are normalized by total counts.

The pileup events observed above ~620 keV (higher energy than the photopeak) are completely eliminated by the separation, although the pileup peak around ~1200 keV cannot be eliminated because the TFA signal itself overlapped.

In addition, the count in the continuous part due to the Compton scattering and the photo peak (below ~600 keV) increased in the spectrum after separation. In particular, the photo peak height increased about one and half times after the separation. This means that the separation procedure will be helpful to find a small peak masked with pile up events.

In view of the energy resolution, the separation method has 0.47 %, the normal method has 0.75 %, and the TFA has 4.4 % in FWHM. Thus, the energy resolution is also improved by the fitting procedure. We can see from the comparison of the spectra that the separation method can correct the distortion and improve the resolution.

References

1) Oishi T., Yamaguchi T., Hagiwara M., Baba M., Yuki H., Otsuki T., Hori J., Proceedings of Science, FNDA2006,067 (2006).
2) Knoll G. F., Radiation Detection and Measurement, Third ed., Wiley, New York, (2000).
3) Mark A. Nelson, Brian D. Rooney, Derek R. Dinwiddie and Glen S. Brunson, Nucl. Instr. and Meth., **A505** (2003) 324.

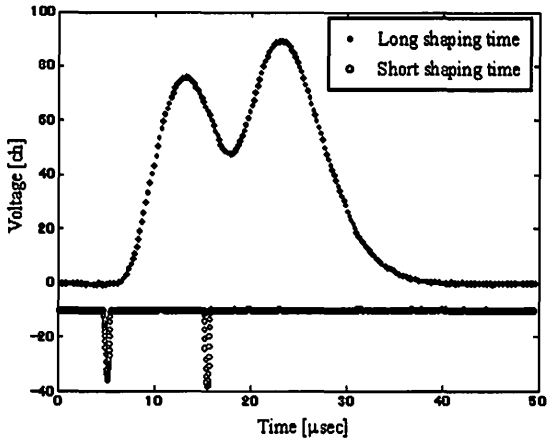

Figure 1. Different shapping time signals.

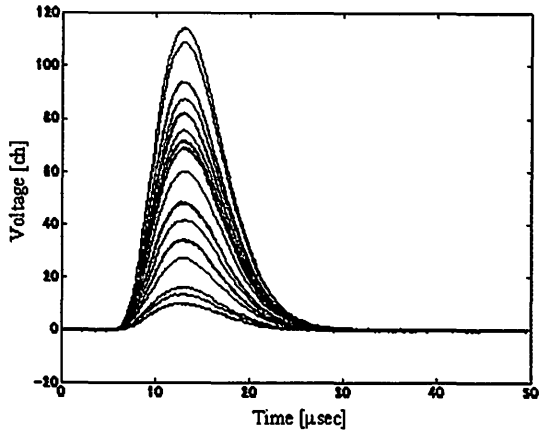

Figure 2. Pulse shape of HPGe with long shaping time.

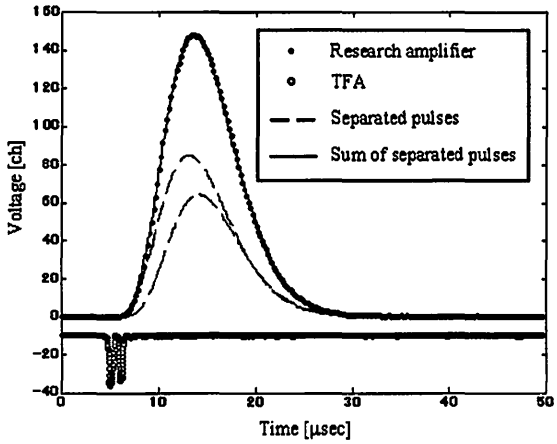

Figure 3. Separation of very close pulses.

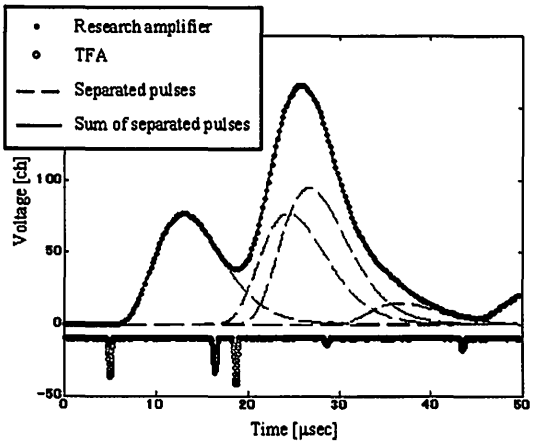

Figure 4. Separation of multiple pileup event.

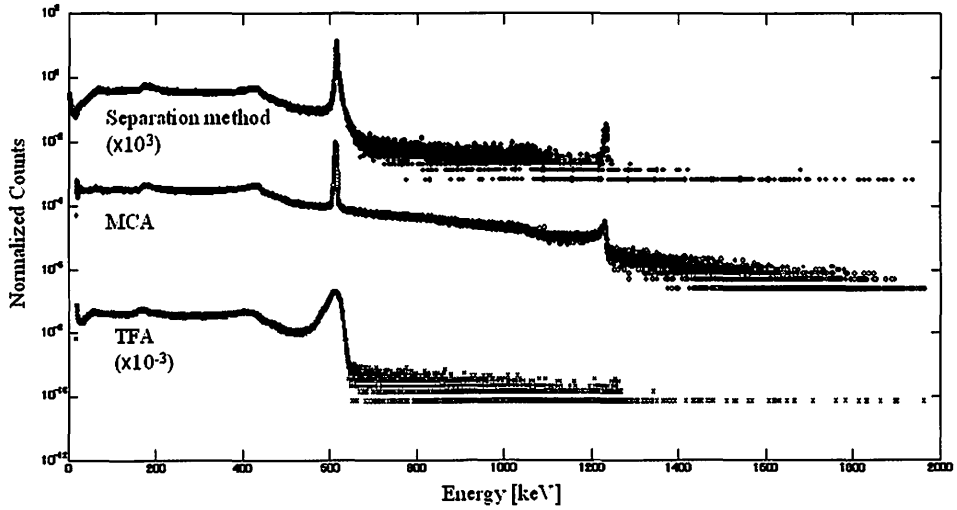

Figure 5. Distorted and Corrected spectrum of ^{137}Cs.

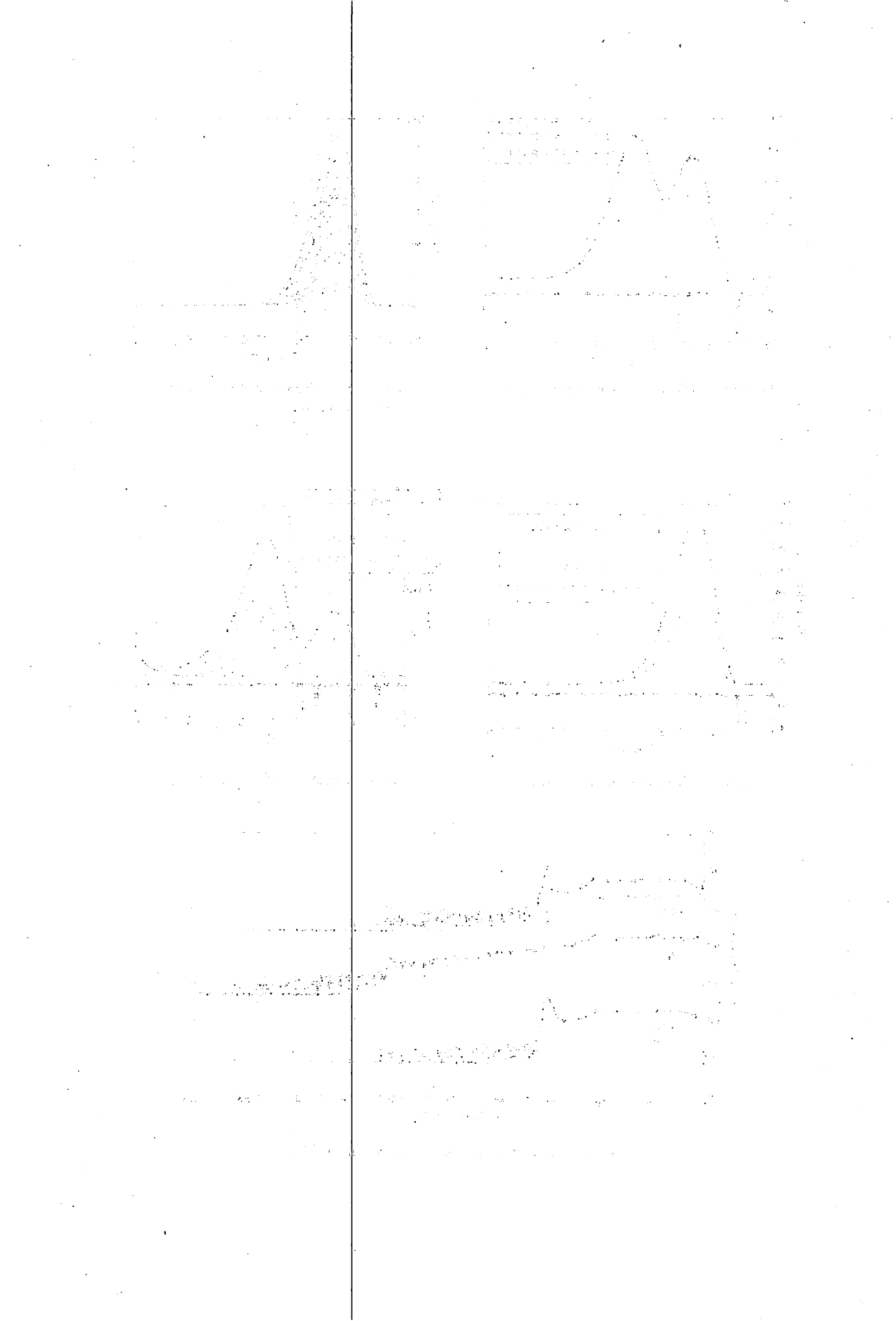

IV. NUCLEAR MEDICAL ENGINEERING

IV. 1. Current Status of the Proton Therapy System at CYRIC

Terakawa A.[1], Ishii K.[1], Chiba T.[1], Miyashita T.[1], Yamamoto T.[1], Arikawa J.[1], Togashi T.[1], Yamashita W.[1], Akiyama H.[1], Koyata H.[1], Fujita Y.[1], Ishizaki A.[1], Totsuka Y.[1], Honda T.[1], Itoh N.[2], Sano T.[2], Wada S.[2], and Orihara H.[3]

[1]*Department of Quantum Science and Energy Engineering, Tohoku University*
[2]*School of Veterinary Medicine and Animal Sciences, Kitasato University*
[3]*Department of Interigent Electronics, Tohoku Institute of Technology*

The beam irradiation system to research for proton therapy using small animals was constructed at the AVF cyclotron facilities of CYRIC. Test experiments using an 80-MeV proton beam were successfully performed. Preliminary results of the beam tests have already been reported[1]. In this report basic specifications and current status of the proton therapy system will be described.

A photograph of the proton therapy facilities at CYRIC is shown in Figure 1. The beam irradiation system consists of two dipole magnets, a scatterer, a ridge filter, beam monitors, a range shifter and a patient bolus and collimators. Recently, a patient couch was installed at about 4 m downstream of the magnet. The beam delivery can be made in wobbler mode[2,3] or in scanning mode. Laminated-core design has been employed for the dipole magnets to reduce eddy currents. Basic specification of the dipole magnets is summarized in Table 1.

The wobbler mode provides a large irradiation field with uniform beam intensity up to about 10 cm in diameter for a 90-MeV proton by using a lead scatterer and an annular beam profile which is generated from alternating current (AC) of 10 Hz with phase difference of $\pi/2$ between the two magnets. In order to generate an appropriate dose distribution the ridge filter, patient collimator and bolus are needed.

In the scanning mode the pencil beam from the AVF cyclotron is laterally scanned with the magnets for which direct current (DC) settings are done under the programmable control while range scanning (energy scanning) is performed with the range shifter by controlling depth dose to generate a 3-dimentinal dose distribution for the target volume. The range shifter consisting of six PMMA plates of 1, 2, 4, 6, 8 and 10 mm thickness

reduces the range in water for an 80-MeV proton (51 mm) up to 31 mm in about 1 mm interval.

The target position can be adjusted with the patient couch whose table can move in both lateral and range directions. The target positioning is carried out by comparing X-ray transmission images of the target animal on the couch with reference images for the treatment plan.

The control system is based on the PLC modules (Yokogawa FA-M3 controllers[4]) which consist of CPUs and several modules such as input/output (I/O), analog-to-digital (A/D) and digital-to-analog (D/A) modules. Positioning modules are also used for controlling motors of movable devices. A schematic layout of the control system is illustrated in Figure 2. The control signals are distributed between the irradiation system and the PLC modules via an assembled control unit which includes terminal blocks, relays, pulse motor drivers, DC power supplies for electric circuits and related devices. In addition, the cable or fiber-optic I/O bus modules (FA-bus or fiber optic FA-bus modules) and local area network (LAN) modules have been employed for data communication between the control room and the experimental rooms. Control programs written in the structured-ladder programming method using the WideField software[4] are downloaded from the personal computers (PC) on the LAN into the CPU module. The graphical user interface (GUI) of the control system has been built using the LabVIEW software[5].

In the next research programs we are planning to perform proton therapy experiments using the present system for tumor cell lines implanted into mice or rats.

References

1) Terakawa A., CYRIC Annual Report (2005) 41.
2) Akagi T., et al., Phys. Med. Biol. **48** (2003) N301.
3) Tamura H., et al., Japan. J. Med. Phys. **18** (1998) 42.
4) IT Machine Controllers (PLC) FA-M3R, YOKOGAWA Co. Ltd., URL: http://www.yokogawa.com/itc/itc-index-en.htm
5) LabVIEW graphical development environment, National Instruments Co. Ltd., URL: http://www.ni.com/labview/

Table 1. Basic specification of the dipole magnets.

Pole length	Pole gap	Maximum field	Field stability	Maximum magnet current
130 mm	105 mm	0.1 T for scanning (DC) 0.1 T (0-peak) for wobbler (AC)	$<10^{-3}$	DC 10 A AC 20A (0-peak, 10Hz)

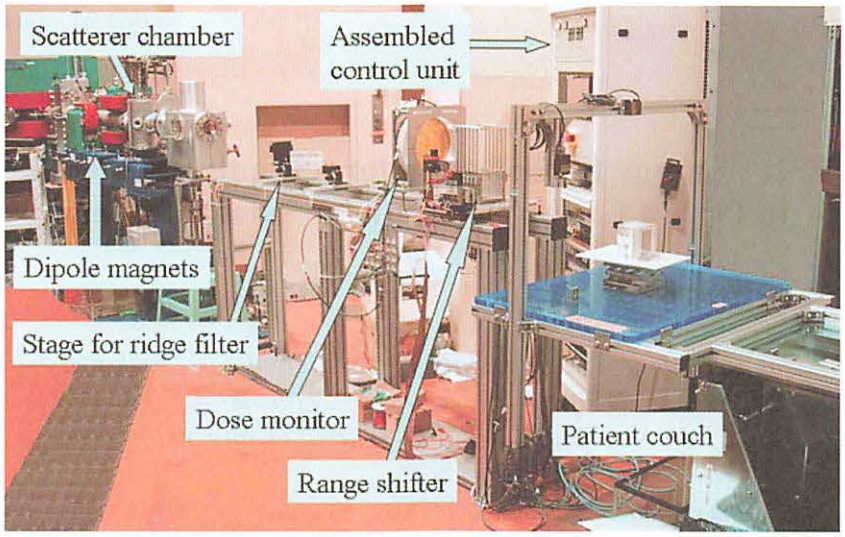

Figure 1. Photograph of the beam irradiation system for proton therapy at CYRIC.

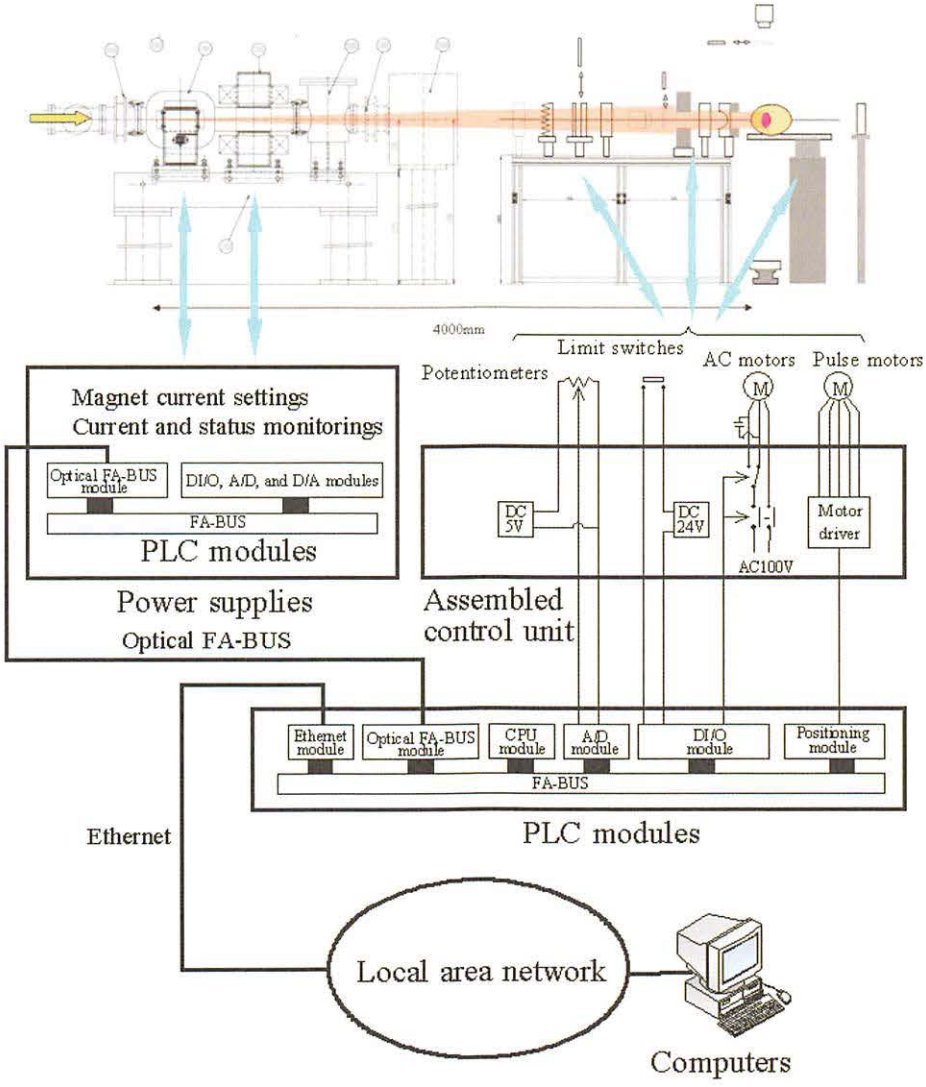

Figure 2. Schematic layout of the control system for the proton therapy facilities.

IV. 2. Energy Filter Design for a Depth Dose Profile in Proton Cancer Therapy for Small Animals

Terakawa A.[1], Ishii K.[1], Chiba T.[1], Miyashita T.[1], Yamamoto T.[1], Arikawa J.[1], Togashi T.[1], Yamashita W.[1], Akiyama H.[1], Koyata H.[1], Fujita Y.[1], Ishizaki A.[1], Totsuka Y.[1], Honda T.[1], Itoh N.[2], Sano T.[2], Wada S.[2], and Orihara H.[3]

[1]*Department of Quantum Science and Energy Engineering, Tohoku University*
[2]*School of Veterinary Medicine and Animal Sciences, Kitasato University*
[3]*Department of Interigent Electronics, Tohoku Institute of Technology*

In radiation therapy heavy ion beams have advantages over an X-ray such as large energy deposition at the end of their path, the so-called Bragg peak and superior radiobiological properties. We are developing new treatment methods based on proton therapy combined with other treatments. Thus, proton therapy experiments using small animals provide a good place for exploring their therapeutic effects and side effects. When using mice or rats in which tumor cell lines are implanted, local dose control for the small target volume is needed. In this report we will describe energy filter designs for an 80-MeV proton beam provided from the wobbler system[1)] at CYRIC to generate spread-out Bragg peaks (SOBP) with narrow widths from 5 to 20 mm at 5-mm intervals.

Figure 1 shows the energy filter which is composed of many PMMA bars. A basic design of the energy filter was determined so that the SOBP could approximately be generated from several depth dose distributions of mono-energy beams. After measuring a depth dose distribution generated with the energy filter, the basic design was modified to obtain the appropriate dose distribution. The designs of each PMMA bar for SOBPs with 5 and 20 mm widths are represented in Fig. 2.

Measured depth-dose distributions are shown in Fig. 3. The uniformities of 5 – 10% in the maximum dose region are larger than those of the designed SOBPs. The actual dose distribution depends on some beam profiles which are not included in the basic design, such as scattering effects due to the filter and other devices, the annual profile of the wobbled beam. In order to improve the uniformity (< 5%), the energy filter designs will be modified in a series of the experiments.

Reference

1) Terakawa A., CYRIC Annual Report (2005) 41. The current status of the proton therapy system at CYRIC will be described in the present CYRIC Annual Report.

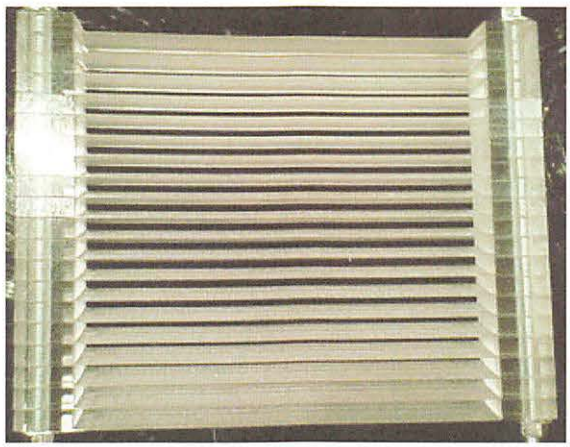

Figure 1. Photograph of the energy filter.

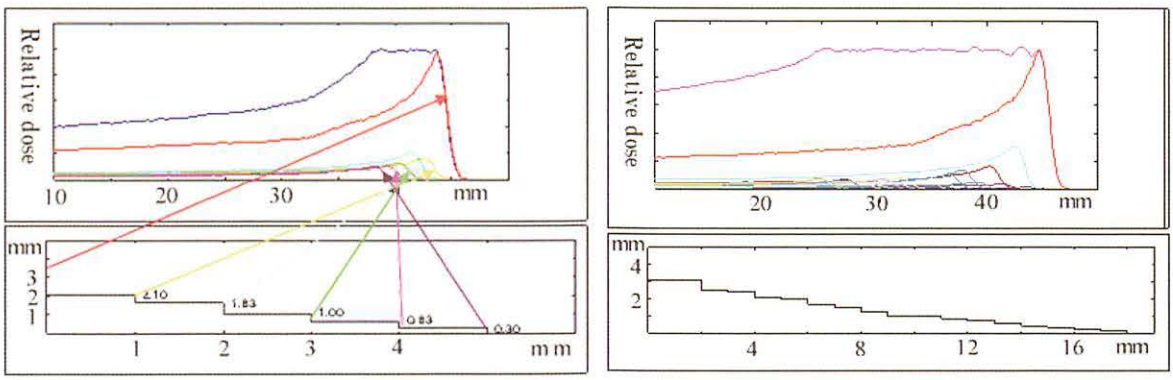

Figure 2. Cross sectional shapes of energy filters and the designed SOBPs.

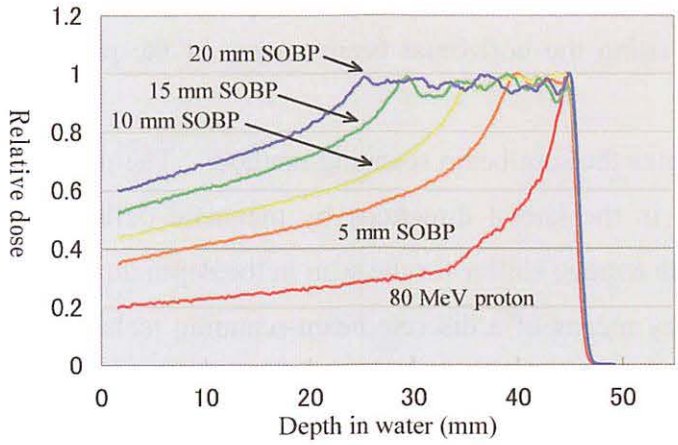

Figure 3. Measured depth-dose distributions in PMMA generated with the energy filters. Depth in PMMA is converted to the water-equivalent depth.

IV. 3. Spot-beam Scanning Technique Developed at the CYRIC Proton Therapy Facilities

Terakawa A.[1], Honda T.[1], Miyashita T.[1], Ishii K.[1], Chiba T.[1], Yamamoto T.[1], Arikawa J., Togashi T.[1], Yamashita W.[1], Akiyama H.[1], Koyata H.[1], Fujita Y.[1], Ishizaki A .[1], Totsuka Y.[1], Itoh N.[2], Sano T.[2], Wada S.[2], and Orihara H.[3]

[1]*Department of Quantum Science and Energy Engineering, Tohoku University*
[2]*School of Veterinary Medicine and Animal Sciences, Kitasato University*
[3]*Department of Interigent Electronics, Tohoku Institute of Technology*

Conventional irradiation techniques in charged-particle therapy such as wobbler and scattering methods spread the dose of a pencil beam from the accelerator over a target volume, and provide an appropriate dose distribution in a tumor with an energy filter, a bolus and a collimator. However, the maximal dose of the so-called spread-out Bragg peak (SOBP) is given to normal tissue outside the tumor because the SOBP is designed to cover the maximum width of the target volume in the beam direction.

A scanning method of the pencil beam can provide a conformal dose profile in the target volume without high dose in the surrounding normal tissue. Unfortunately, the scanning technique is applied to limited cases[1)] in actual treatments because patient safety concerning the beam delivery and the treatment plan has not fully been established at present. In this report we will describe preliminary results for beam tests of the scanning technique developed using the horizontal beam course of the proton therapy system[2)] at CYRIC.

Figure 1 illustrates the spot-beam scanning method. The pencil beam from the AVF cyclotron is scanned in the lateral directions by magnetic deflection whereas the beam energy is changed with a range shifter for the scan in the depth direction. The dose control has been performed by means of a discrete beam-scanning technique in which the pencil beam is delivered into the target volume spot by spot to generate a designed dose distribution for the tumor.

Test experiments for the discrete beam-scanning technique were successfully performed using an 80-MeV proton. Figure 2 shows the lateral dose distributions

measured with the imaging plate[3] (IP) concerning the conformal irradiation (Fig. 2(b)) and the intensity modulated irradiation (Fig. 2(c)), together with the spot beam profiles (Fig. 2(a)). The spot-beam size is currently more than 10 mm (FWHM) in diameter. We plan to reduce the beam size up to about 5 mm in diameter by improving the beam transport optics upstream of the irradiation system.

In order to provide the SOBP with the scanning technique, the energy scanning with the range shifter was performed using a 70-MeV proton based on the SOBP designed with 11 depth-dose profiles of mono energy protons (Bragg peaks : BP) measured with the IP. Figure 3 shows the depth dose distribution measured with the ionization chamber[4] and the designed SOBP. The experimental result does not agree with the designed SOBP at the end of the range. This discrepancy is probably ascribed to the energy dependence[5] in dose measurement with the IP.

References

1) Pedroni., et al., Med. Phys. 22 (1995) 37.
2) Terakawa A., et al, CYRIC Annual Report **41** (2005) The current status of the proton therapy system at CYRIC will be described in the present CYRIC Annual Report.
3) Fuji Photo film CO., LTD., http://www.fujifilm.co.jp/bio/si_imgplate/imgplate.html
4) The 0.6 cm^3 PTW Farmer chamber type 30013, PTW, Freibrug, Germany, http://www.ptw.de/
5) Nohtomi A., et al. Nucl. Instrum. and Methods A **424** (1999) 569.

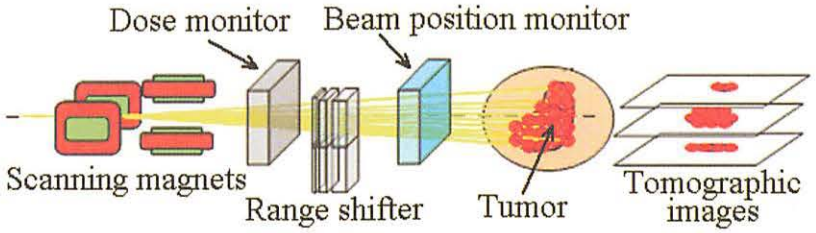

Figure 1. Discrete spot-beam scanning technique.

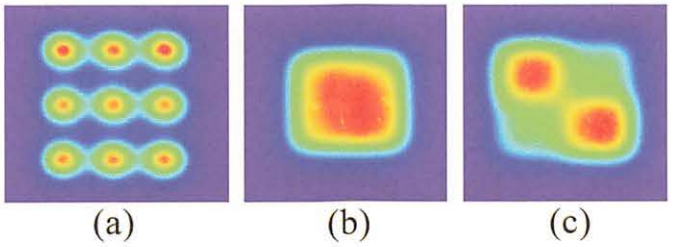

Figure 2. Lateral intensity distributions using the spot-beam scanning method.

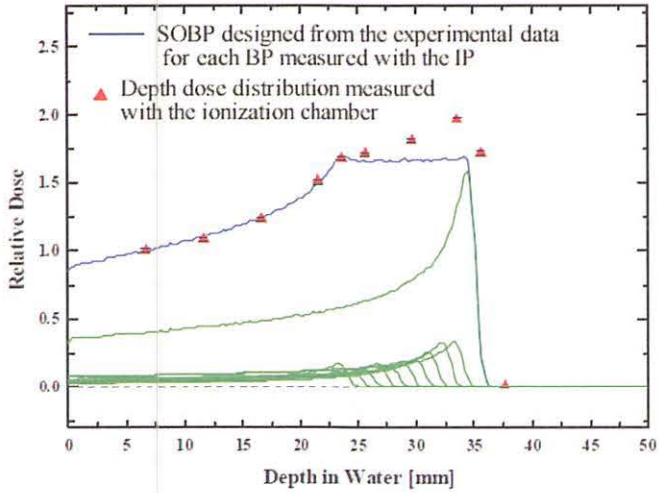

Figure 3. Depth dose distribution generated in PMMA with the scanning method based on the SOBP designed from each Bragg peak. Depth in PMMA is converted to the water-equivalent depth.

IV. 4. Treatment Planning System Developed for Proton Therapy at CYRIC

Terakawa A.[1], Totsuka Y.[1], Chiba T.[1], Ishizaki A.[1], Miyashita T.[1], Yamamoto T.[1], Arikawa J.[1], Togashi T.[1], Yamashita W.[1], Akiyama H.[1], Koyata H.[1], Fujita Y.[1], Honda T.[1], Ishii K.[1], Itoh N.[2], Sano T.[2], Wada S.[2], and Orihara H.[3]

[1]*Department of Quantum Science and Energy Engineering, Tohoku University*
[2]*School of Veterinary Medicine and Animal Sciences, Kitasato University*
[3]*Department of Interigent Electronics, Tohoku Institute of Technology*

In recent years the proton irradiation system has been developed[1)] at CYRIC for research programs of proton therapy using small animals and their clinical application to cancer treatment for companion animals. During the construction of the proton irradiation system, we have developed a treatment planning system for simulating a depth-dose distribution of a therapeutic proton beam as well.

The depth dose generated in a patient from the proton irradiation can approximately be estimated based on computer tomography (CT) through the conversion of the CT number into the proton stopping power ratio as shown in Fig. 1. Thus, the depth dose along the proton path is calculated pixel by pixel for each slice image. Three-dimensional dose simulation has been obtained using a pencil-beam algorithm in which depth and lateral dose profiles of the mono energy beam is approximately described with an analytical function[2)] and a Gaussian distribution, respectively. The treatment plan for the patient animal is done with the help of graphical user interfaces (GUI) developed with the Lab-view soft ware[3)] (Fig. 2).

The validity of the simulation was checked by comparing the simulation results in the case of two phantoms (Phantom-1 and Phantom-2) with measured dose distributions. The Phantom-1 is composed of PMMA, water-equivalent material and bone-equivalent material and equipped with a collimator. The dose distribution generated in water-equivalent material located downstream of the Phantom-1 was measured with the imaging plate[4)] (IP). The Phantom-2 is a circular cylinder of PMMA with a collimator and a bolus. Dose control was made so that the maximal dose was delivered into a spherical target volume

near the surface of the Phantom-2. The dose distribution in the Phantom-2 was measured with the IP. In both cases an 80-MeV proton beam with the spread-out Bragg peak was provided from the wobbler system[1].

In Figs. 3-5, the phantom designs and comparisons between the dose predictions and the experimental results are summarized. Good agreement has been obtained in both cases. Figure 6 shows examples for treatment plan in proton therapy for a mouse and a dog. We are planning to perform proton therapy experiments on mice or rats by using the present treatment planning system in the next phase.

References

1) Terakawa A., et al., CYRIC Annual ReportT **41** (2005) The current status of the proton therapy system at CYRIC will be described in the present CYRIC Annual Report.
2) Bortfeld T., Med. Phys. **24** (1997) 2024.
3) LabVIEW graphical development environment, National Instruments Co. Ltd., URL: http://www.ni.com/labview/
4) Fuji Photo film CO., LTD., http://www.fujifilm.co.jp/bio/si_imgplate/imgplate.html.

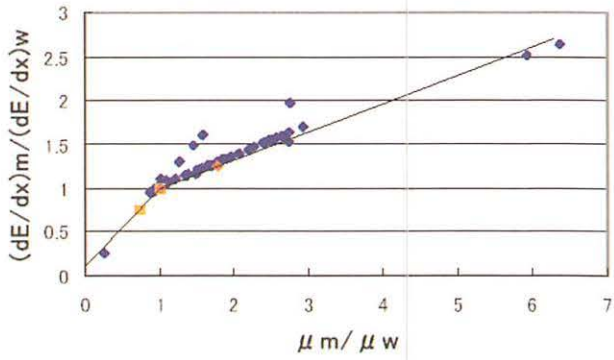

Figure 1. Relation between attenuation-coefficients of an X-ray used in CT-scan for various materials relative to that for water (μm/μw) and the corresponding proton stopping powers relative to that for water {(dE/dx)m/(dE/dx)w}.

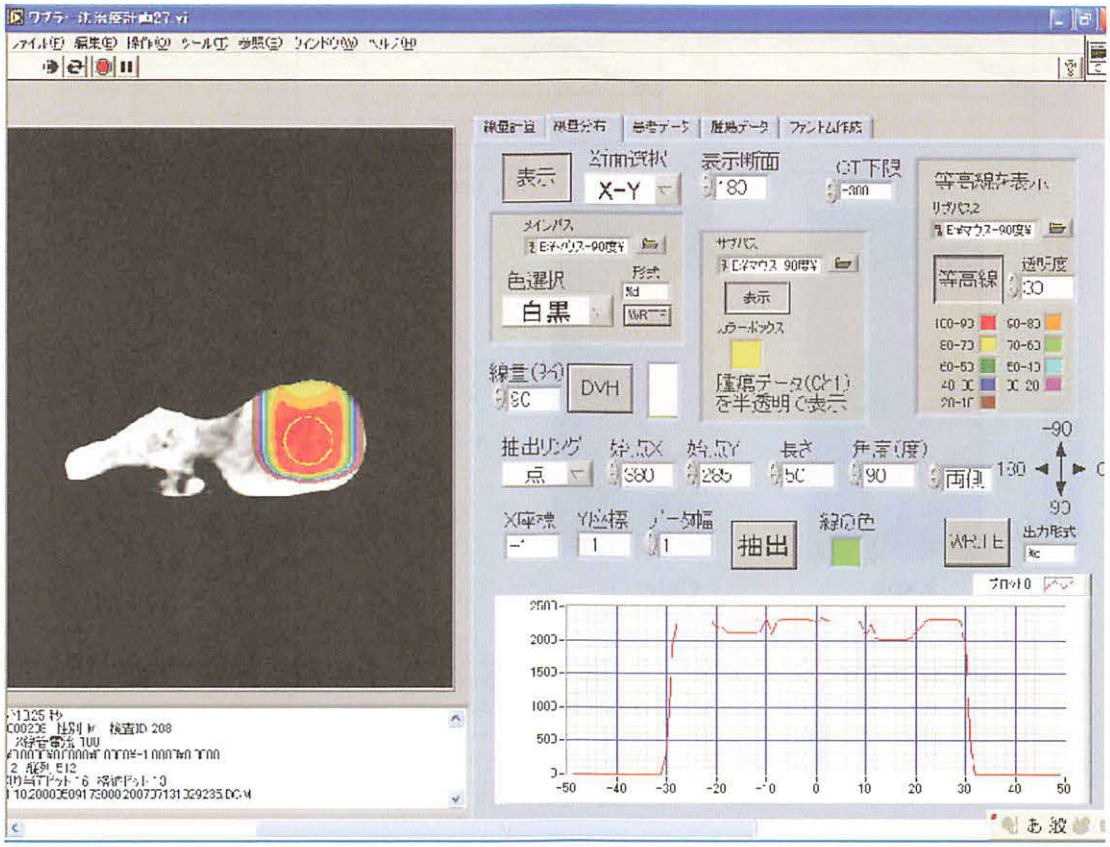

Figure 2. GUI of the treatment planning system.

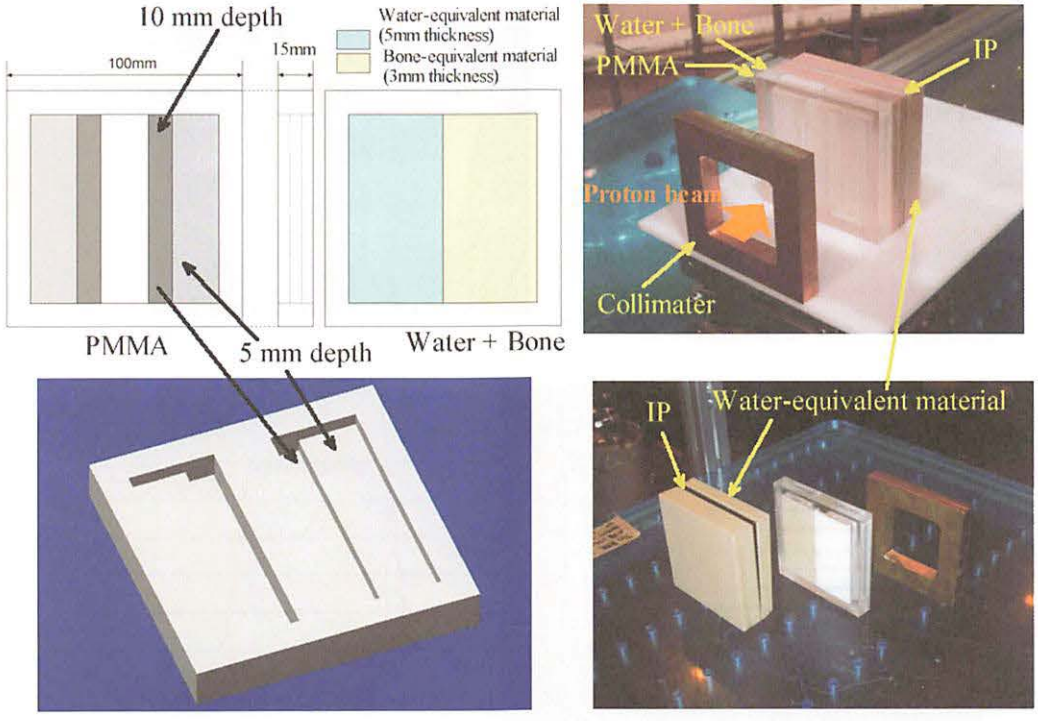

Figure 3. Design and photographs of the phantom-1.

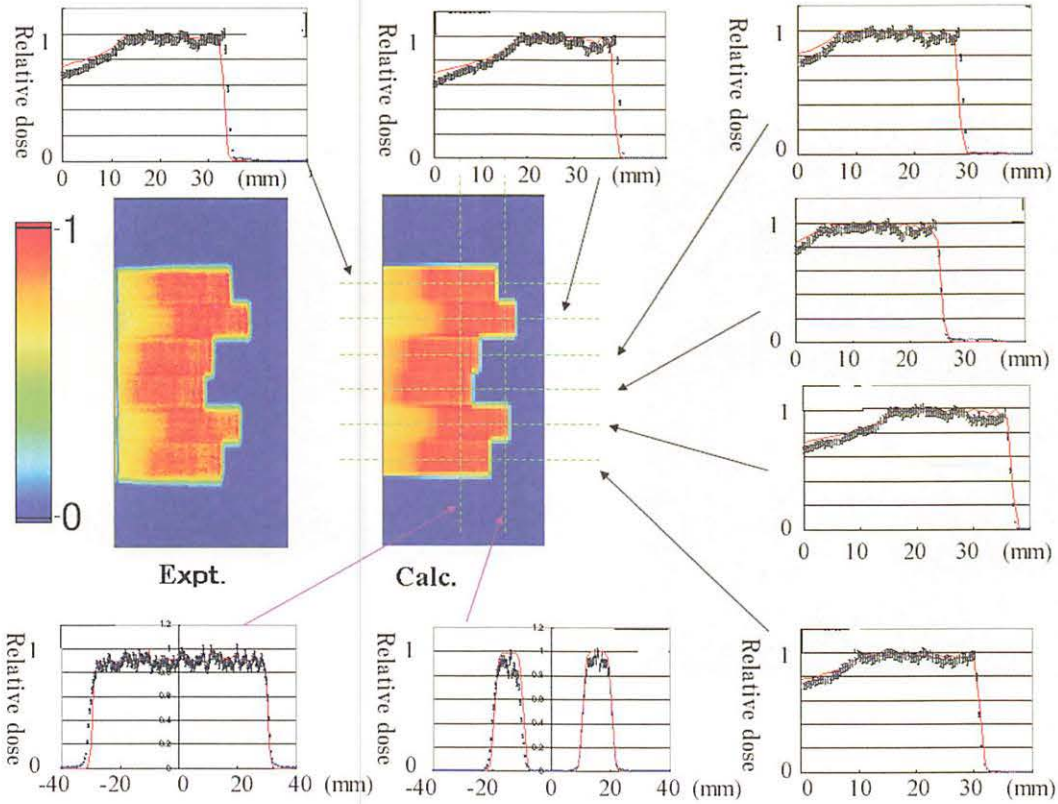

Figure 4. Comparison between the simulation and the measured dose distributions in the water-equivalent material located downstream of the phantom-1.

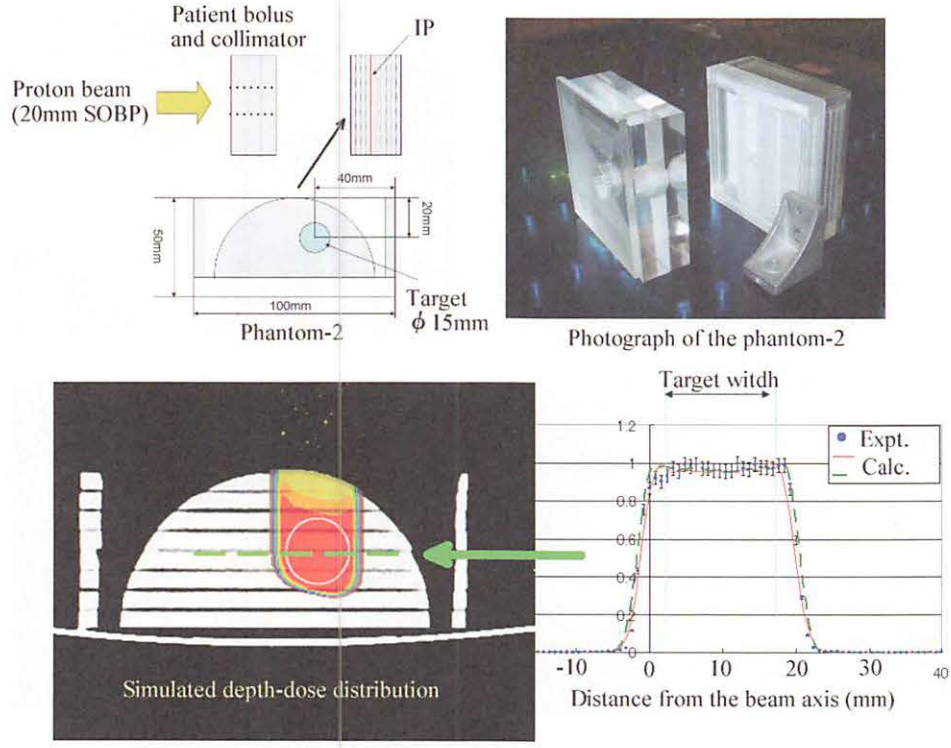

Figure 5. Design of the phantom-2 and simulated dose distribution compared with the experimental result.

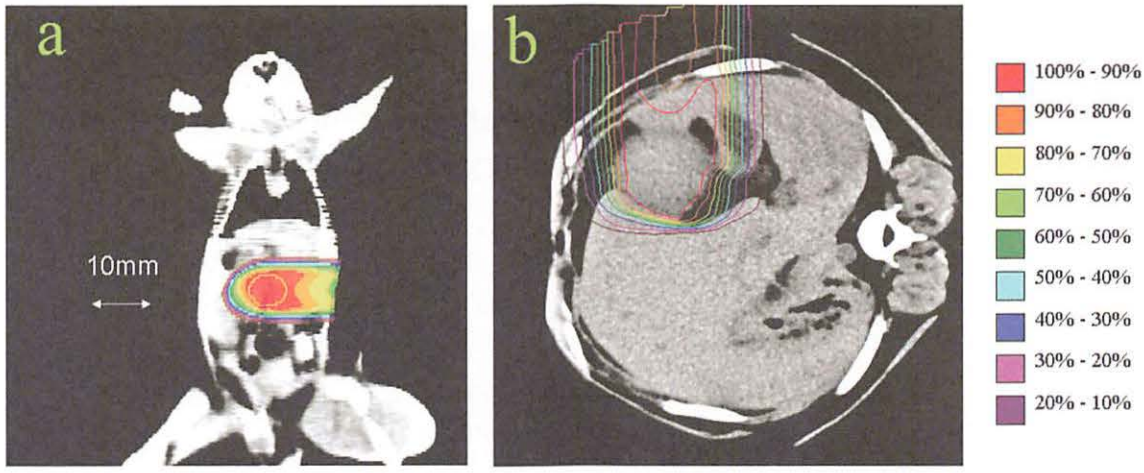

Figure 6. Depth dose simulations in proton therapy for a mouse (a) and a dog (b).

IV. 5. Skin Dose Measurement for Patients Using Imaging Plates in Interventional Radiology Procedures II

Ohuchi H.[1], Kaga Y.[2], Arai T.[2], and Suzuki S.[2]

[1]*Graduate School of Pharmaceutical Sciences, Tohoku University*
[2]*Sendai Kousei Hospital*

Introduction

Fluoroscopically-guided interventional radiology (IR) procedures have been under increased scrutiny in recent years. However, reports of radiation-induced severe injuries to patients' skin have steadily increased since the early 1990's[1,2]. To prevent patients from suffering radiation skin injuries, estimating the radiation dose delivered to the skin of patients during IR procedures should be important.

According to ICRP Publication 85[3], the patient dose of priority concern is the absorbed dose in the area of skin that receives the maximum dose during an interventional procedure. The easiest way to determine the entrance skin dose (ESD) is a direct measurement by using small dosimeters such as thermoluminescence (TL) dosimeters and photoluminescence glass dosimeter (PLD) chips. However, these methods using a limited number of dosimeters possibly miss spots of the maximum cumulative dose, resulting in underestimation of the maximum ESD. This is so because the points that receive the maximal ESD might vary widely and unexpectedly with individual procedures, and they could be widely scattered; additionally, radiation fields may overlap during IR procedures. We therefore proposed to use imaging plates (IPs) for mapping skin doses of patients in IR procedures. The ESD was measured by fitting a 40 × 40 cm IP sheet around a patient's back using a corset in clinical studies of a patient who underwent IR procedures at Sendai Kousei Hospital. The corset can minimize a geometric discrepancy in the dose estimate by putting an IP sheet between sheets during the procedure. At the same time, the ESD was measured using a commercially available PLD. PLDs were held in the holes of the polyurethane sheet in the corset. The results of ESDs thus obtained by IPs and PLDs were compared.

Materials and methods

Imaging plate and readout technique

A 20 cm × 40 cm BAS-TR type IP (Fuji Film Co., Ltd.) was used. It has a 50-μm-thick photostimulable phosphor ($BaFBr:Eu^{2+}$) affixed to a 250-μm--thick polyethyleneterephthalate layer as support and has no protective surface layer. The phosphor, whose density is 2.61 g/cm^3, contains Ba (37.82%), F (5.23%), Br (22.01%), and I (34.94%) by weight. BAS-TR type IP can accurately measure X-ray doses ranging from 1 μGy to 100 Gy and the dose-response is linear up to about 10 Gy[4]. IPs show the same response in the range between 100 μGy/min and 3.73 Gy/min without a counting loss. For measuring the ESD in a patient, to cover the whole area of a patient's back, a 40 × 40 cm IP was formed by coupling together two BAS-TR sheets. The IPs were wrapped in black polyethylene to shield them from light during irradiation and put inside a corset to make IPs fit to the patient's back. The IPs were scanned within a few hours after irradiation using a coloredcellophane technique[4,5] and a 200 × 200 μm BAS-1000 readout system (Fuji Film Co., Ltd.). The IPs were then rescanned after annealing at 100°C for 70 h to minimize the effect of fading and estimate a quantitative dose precisely.

Photoluminescent Glass Dosemeter and Corset

The GD-302M (Asahi Technoglass Corp.) consists of a silver-activated photoluminescence glass dosemeter (PLD) chip. Each PLD chip is encapsulated within glass and is cylindrical, 1.5 mm in diameter and 12 mm in length and then fixed in a plastic holder, 2.8 mm in diameter and 13 mm in length. The corset consists of four 450 mm x 600 mm polyurethane sheets, three are 2-mm thick and one is 4-mm-thick. The 4-mm-thick sheet has 13 mm × 14 mm holes at 5-cm intervals in an 11 × 8 grid for placing the PLD chips inside. The corset has three sets of Velcro bands on both sides to hold it close to patient's body by fastening the ends of bands together. It can be easily worn and fit to the body. For measuring a patient's ESD, the IP was placed between two 2-mm-thick sheets and 48 PLD chips were distributed inside 48 discrete holes at 5-cm intervals in an 8 × 6 grid one by one, as shown in Fig. 1. By fastening Velcro bands, IPs and PLD chips were held steady inside the corset. This made it possible to match each corresponding measuring region in IP images with that of PLD chips.

X-ray irradiation

The ESDs of patients during IR procedures in clinical studies were measured. An X-ray unit, KX0-100G (Toshiba Medical Systems Co.) with 2.6-mm-thick Al filter was used. The tube voltage, tube current, and exposure time were recorded at 3 min intervals during fluoroscopy. The effective conditions of X-ray irradiation were estimated from these records. The dose response of IPs and PLD chips in the range from 1 mGy to 2 Gy was evaluated with the X-ray unit by placing IPs and PLD chips on the tabletop immediately under an acrylic phantom (i.e., entrance skin location) and providing the X-ray beam from under the table with tube voltages of 60, 80, 100, and 120 kV. The acrylic phantom was 20 cm thick and had a 33 × 33 cm front face. Two 1 × 1 cm IPs, which were cut from a 20 x 40 cm IP sheet, and four PLD chips were irradiated at each tube voltage and each exposure was determined by placing an ionization chamber in the center of IPs and PLD chips. Ionization chambers, the VICTOREEN model 500 of 3.26 ml effective volume (Elimpex-Medizintechnik) was used. It is traceable to the Japanese national standard maintained by the Japan Quality Assurance Organization (JQA) in Tokyo, Japan.

Results and discussion

The PSL density (PSL/mm^2) and PLD response (mGy) for tube voltages of 60, 80, 100, and 120 kV on the acrylic phantom are obtained as a function of the dose (mGy) and plotted in Fig. 2a and 2b. Both variations of the measured values between two IPs or among four PLD chips at each irradiated dose or tube voltage were within about ±2.5%. Each relationship has linearity in the measured range.

A case of a 66-year-old male patient who underwent Percutaneous Coronary Intervention (PCI) is exhibited as an example of entrance skin dose monitoring with IPs and PLD chips. Neither the joint formed by coupling together two IP sheets nor the corset interfered with diagnosis. The average tube voltage was calculated to be 81.0 kV and the ESDs were calculated using an equation obtained from the regression line in Fig. 2a and 2b. Distributions of the ESD were thus obtained from the PSL density in IP images and PLD chips and both mapped dose distributions showed quite similar shape. The 3-D and 2-D contour dose maps obtained with IPs are shown in Fig. 3a and 3b, respectively, giving 1,400 mGy as the peak skin dose. Each value of ESD estimated by IPs and PLD chips in a region where the ESDs were rather high (including hot spot) is given in Table 1. The number and alphabet of measuring regions in Table 1 correspond to those exhibited in Fig.

1 and 3b. The spatial relative dose profiles from both dose estimates showed generally good agreement. However, the doses obtained with PLD chips are consistently lower than those obtained with IPs except a few cases. The highest dose was observed at region B1 and the difference of the doses measured with the two dosemeters was 34%.

One reason for this discrepancy is the radiation shielding effect for X-rays by the IP. As PLD chips were distributed on the reverse of the IP sheet in this study, a portion of the X-rays might have been absorbed by the IPs during IR procedures. The absorption was estimated to be 7.7% at a tube voltage of 80 kV[6]. Another reason may be associated with differences in angular response between them for low-energy X-rays. Fig. 4 shows an angular response of PSL signals of IPs for X-rays with tube voltages of 60, 80, 100, and 120 kV. The angular dependence was determined by rotating the IP along the source-to-detector axis in the directions of -90° to 90° in 15° step. Two 2 x 3 cm IPs were irradiated in air at each irradiation and each point on the graph corresponds to the average value of them. The maximum variations among individual readings of two IPs are 1.6%, 2.6%, and 2.1% at tube voltages of 60, 80, and 100 kV, respectively, except -90° to 90°. The results revealed that the IP has an almost isotropic efficiency within ± 75° at all tube voltages. Relatively low responses of the IP are observed at ± 90°, because large numbers of incidences might not hit the surface of the thin IP and/or X-rays might be attenuated by the IP itself as they traverse the IP. The corset can offer advantages of minimizing not only a geometric discrepancy between the IP and the patient body reducing effects of large angle incidence when the X-ray tube rotates during the IR procedure.

The angular dependence of PLD chips was determined in the same way and exhibited in Fig. 5a. The maximum variations among individual readings of two PLD chips are 6.4%, 6.2%, and 2.0% at tube voltages of 60, 80, and 100 kV, respectively, except -90° to 90°. The results revealed that the angular dependence of the radio-photo luminescence (RPL) signal of PLD chips becomes large as the incidence angle increases especially more than ±45°, and the largest decrease is observed at 60 kV. A decrease of the RPL signal at ± 70° is estimated to be 24-28% at 80 kV and 40% at 60 kV, respectively, by expressing the RPL signal as a fraction of an intensity measured at angle 0°. The cylindrical shape of the PLD chip and the readout way using the FDG-1000 reader can explain this result. Schematic diagram of the readout of a PLD chip is given in Fig.5b. The FDG-1000 reader uses pulsed UV laser excitation (narrow beam; ϕ1.0 mm) and the UV beam comes into a chip horizontally, then, the RPL from the 6-mm aperture is collected

into a photomultiplier tube. As the energy of incident X-rays decreases, thus, the angular dependence increases because of the attenuation by the dosemeter itself whose effective atomic number is 12.04. Besides, the thickness of PLD chips might cause the self-shielding of both the excitation and the emitted light during the reading process. This large angular dependence of the PLD chip might result in underestimation of the ESD including scattered X-rays with various angles during IR procedure.

Comprehensive results of this study demonstrated that IPs were able to measure ESD in even small high dose regions with steep dose gradients in all ranges used during IR procedures without an angular dependence by using the corset and then determine the peak skin dose without missing hot spots.

References

1) Vano E., Arranz L., Sastre J.M., Moro C., Ledo A., Garate M.T., Minguez I., Br. J. Radiol., **71** (1998) 510.
2) Faulkner K., Vano E., Radiat.Prot.Dosim.**94** (2001) 95.
3) International Commission on Radiological Protection (ICRP). Avoidance of radiation injuries from medical interventional procedures. Oxford: Pergamon Press; ICRP Publication 85; Ann ICRP **30** (2); 2000.
4) Ohuchi H., Yamadera A., Nucl.Sci.Technol.Suppl. **4** (2004) 140.
5) Ohuchi H., Yamadera A., Jpn. J. Health Phys. **39** (2005) 198.
6) Ohuchi H., Satoh T., Eguchi Y., Mori K., Radiat.Prot.Dosim. **117** (2005) 432.

Table 1. Comparison of ESD (mGy) obtained by IPs and a PLD chip at the same measuring region.

Measuring regions	ESD obtained by IPs (mGy)	ESD obtained by a PLD chip (mGy)
A1	130	78
A2	86	60
A3	31	37
B1	1,400	930
B2	740	460
B3	56	56
C1	140	200
C2	300	320
C3	43	52

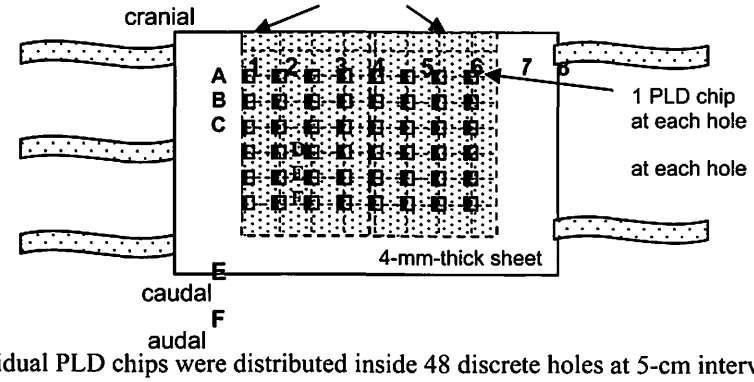

Figure 1. Individual PLD chips were distributed inside 48 discrete holes at 5-cm intervals in an 8 × 6 grid.

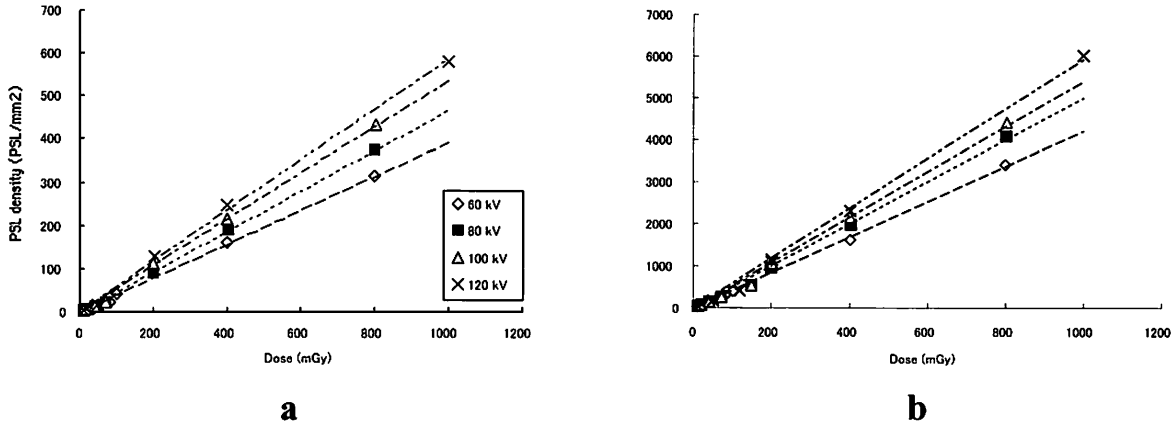

Figure 2. Dose response of (a) IPs and (b) PLD chips using using KX0-100G at Sendai Kousei Hospital, respectively, evaluated by placing IPs and PLD chips on the acrylic phantom and providing the X-ray beam with tube voltages of 60, 80, 100, and 120 kV.

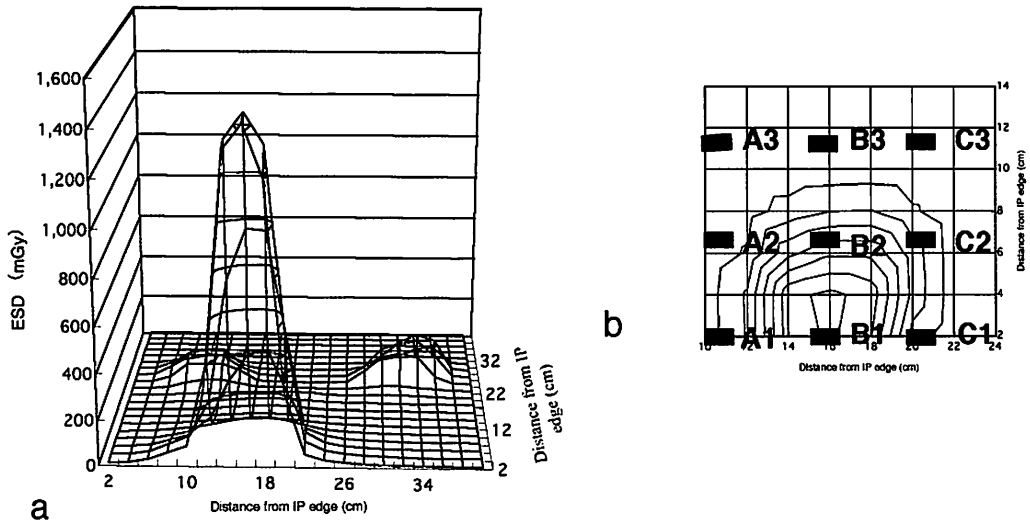

Figure 3. Contour dose map obtained by scanning of IPs. (a) 3-D and (b) 2-D mapped images of ESDs. In Fig. 3b, measuring points where PLD chips were placed are exhibited by superposing on the IPs' image.

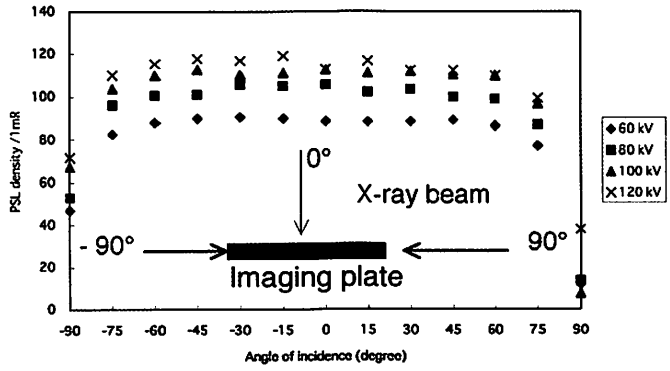

Figure 4. Angular response of PSL signals of IPs for X-rays with tube voltages of 60, 80, 100, and 120 kV.

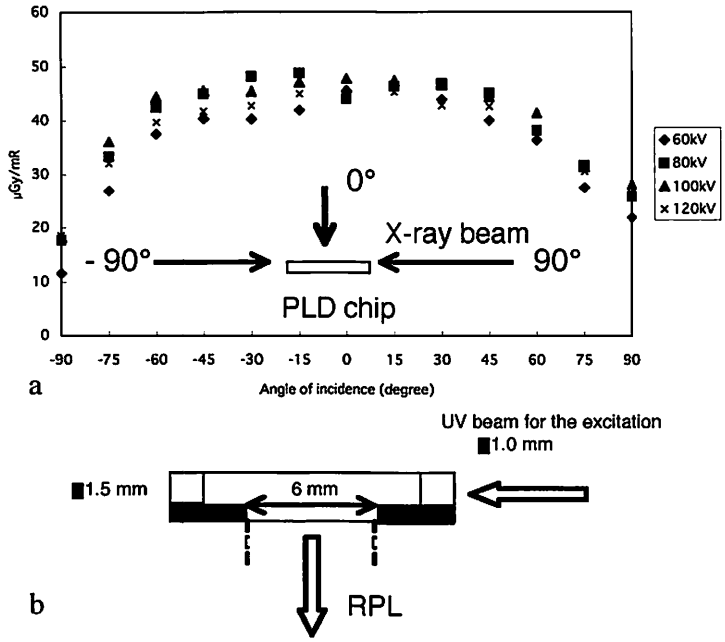

Figure 5. (a) Angular distribution of PLD chips for X-rays with tube voltages of 60, 80, 100, and 120 kV. (b) Schematic diagram of the readout of a PLD chip.

IV. 6. On the Use of a Thick Carbon Target in the 90° Compton Spectroscopy for the Measurement of Diagnostic X-rays

Mohammadi A.[1], *Baba M.*[1], *and Ohuchi H.*[2]

[1]*Cyclotron and Radioisotope Center, Tohoku University*
[2]*Graduate School of Pharmaceutical sciences, Tohoku University*

Radio-diagnostic technologies are widely used in medical fields. In order to perform quality assurance and quality control of the X-ray radiographic systems, we studied the Compton spectroscopy using scatteres with various shape and size to find optimum condition of scattere in terms of efficiency and energy broadening[1, 2]. For the purpose, simulation was made for Compton scattered photons at 90° after the secondary collimator in the experimental setup (Fig. 1, without the detector) using the MCNP4C code.

The flux of 90° scattered photons was calculated for different shapes of carbon scatterers including a cylinder with height and diameter of 2 cm, and five cylinders with the same diameter of 2 cm but cut at 15°, 30°, 45°, 60° and 75° respectively.

Figure 2 shows simulation photon spectrum at 90° for 100 keV monoenergetic photons at x-ray focal spot from a cylinder and the scatterers with cutting angle of 15° and 30°. The energy broadening is shown in Fig. 3 for primary photon energy of 100 keV. From Fig. 2 and Fig. 3, it is clear that smaller cutting angle leads to lower values of energy broadening and multiple scattering. However, from the viewpoint of fabrication and practical use, this cutting angle is not convenient. Fortunately, the energy broadening and fraction of multiple scattering are weak functions of the cutting angle; hence we adopted two carbon scatterers with cutting angle of 30° and 45° in our experiments.

Compton scattered photon spectrum of an x-ray unit (Hitachi Medico Machine) at 70 kV and 5 mA was measured in experimental set up of Fig. 1. The scattered photon spectrum was deduced by the stripping method and then the primary x-ray spectrum was calculated using Compton scattering cross section with Klein-Nishina formula[3]. Measured and reconstructed x-ray spectra are shown in Fig. 4 and Fig. 5 from scatterers with 30° cutting angle and 45° cutting angle, respectively.

For validation of reconstructed spectra, the exposure at a distance of 50 cm was measured using an ion chamber (Radiation Monitor Controller, Model 9015, 6 cc chamber) and was compared with calculated exposure from reconstructed spectra. The measured exposure was compared with calculated exposures in table 1 at an X-ray tube voltage of 70 kV. The calculated exposure results based on the Compton spectroscopy using two scatteres, were confirmed by the results of the measured exposure. Therefore, Compton scattering measurements using thick carbon scatterers can be effectively used to evaluate the performance of radio-diagnostic systems.

Acknowlegement

The authors would like to express their gratitude to operating crew of Sendai Kousei hospital for the kind cooperation, especially Mr. Kaga and Mr. Yamada.

References

1) Yaffe M., Taylor K.W., Hohns H.E., Medical Physics, **3** (1976) 328.
2) Matscheko G., Carlsson G.A., Ribberfors R., Phys. Med. Biol., **34** (1989) 199.
3) Maeda K., Matsumoto M., Taniguchi A., Med. Phys., **32** (2005) 1542.

Table 1. Comparison of measured exposure and calculated exposures for tube voltage of 70 kV.

Method	Exposure (mR)
Reconstructed spectrum from scatterer with 30° cutting angle	669.9
Reconstructed spectrum from scatterer with 45° cutting angle	680.3
Ionization chamber	690.0

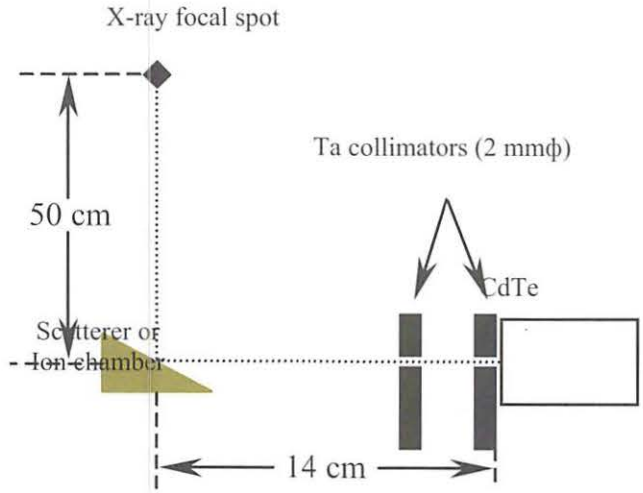

Figure 1. Experimental setup for Compton scattering measurement.

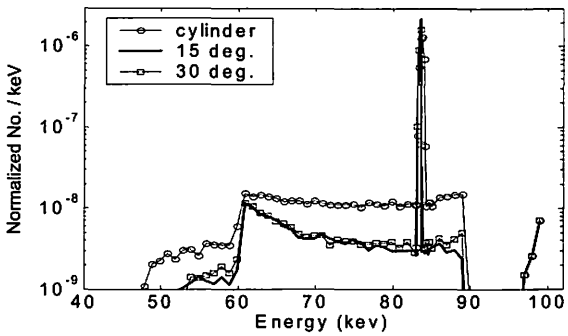

Figure 2. Calculated spectra of Compton scattered photons for primary photons of 100 keV for threeScatterers.

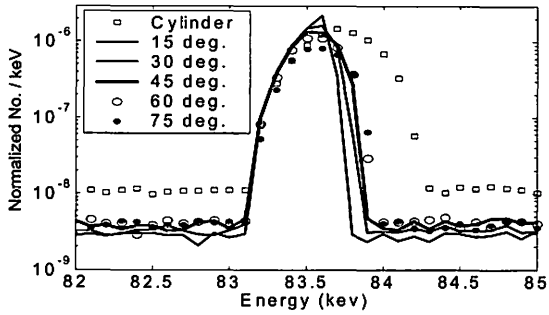

Figure 3. Energy broadening of Compton scattered photons for primary photons of 100 keV.

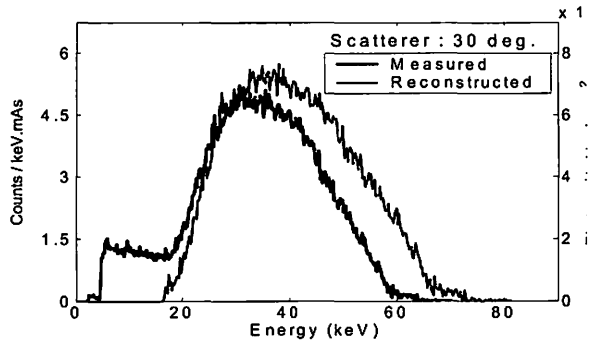

Figure 4. Measured and reconstructed spectra using a scatterer with 30° cutting angle for 70 kV tube voltage.

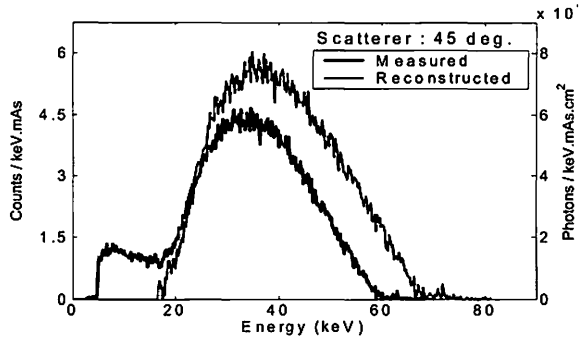

Figure 5. Measured and reconstructed spectra using a scatterer with 45° cutting angle for 70 kV tube voltage.

IV. 7. Prototype of High Resolution PET Using Resistive Electrode Position Sensitive CdTe Detectors

Kikuchi Y.[1], Ishii K.[1], Yamazaki H.[2], Matsuyama S.[1], Sakai T.[1], Kouno M.[1], and Nakamura K.[1]

[1]Graduate School of Engineering, Tohoku University
[2]Cyclotron and Radioisotope Center, Tohoku University

We developed a prototype of high resolution PET using position sensitive CdTe detectors. A resistive electrode is needed for a position sensitive detector. We developed a method to make a resistive electrode on a CdTe crystal and made one dimensional position sensitive CdTe detectors experimentally. The position resolution of 1.2 mm (FWHM) was obtained. We constructed a prototype of PET using position sensitive CdTe detectors, which has a high resolution of ~1 mm (FWHM).

Resistive electrode on CdTe crystal

Performance of semiconductor detectors depends on electrode structures. The Schottky type CdTe detector whose electrode structure is In(anode)/CdTe/Pt(Cathode) has a good reverse bias performance. Hence, a high bias voltage (several hundred V/mm) can be applied to the detector and a good time resolution can be obtained compared with other CdTe detectors. So, position sensitive and Schottky type detectors are suitable for PET.

Supposed that the resistivity of the electrode depends on its thickness, we obtained a relation between the thickness and resistance.

Figure 1 shows a relation between In electrode thickness and resistance. The resistance is inversely proportional to the electrode thickness. So, the resistivity of In electrode can be increased by thinning the electrode thickness. This results that the Schottky type detector with high resistive electrode can be made.

One-Dimensional position sensitive CdTe detector (1D-PSD)

Figure 2 shows a photo and a schematic image of a 1D-PSD made experimentally

with a 20 × 10 × 1.0t mm^3 crystal. The In electrode thickness is 750 Å, and the resistance is about 150 kΩ. Two signals from a anode are denoted by signal 1 and signal 2 and that of a cathode by signal 3.

We measured a position resolution of the detector using β rays from a collimated Am source. The surface of the detector was irradiated with β rays. Figure 3 shows position spectra of the signal 1 / the signal 3. A good position resolution of about 1.2 mm (FWHM) at the center of the detector was obtained.

Prototype of PET using position sensitive CdTe detectors

We constructed a prototype of PET using position sensitive detectors. The prototype consists of 2 detector units which includes 16 1D-PSDs and a preamplifier circuit respectively (Fig. 4 (right)). A ^{22}Na point source (active area: about 0.5 mm diameter) was placed on a rotating stage. The reconstructed images of the point source and their profiles are shown in Fig. 5 (transaxial) and Fig. 6 (axial). The transaxial spatial resolution of 0.75 mm (FWHM) and the axial one of 1.5 mm (FWHM) were obtained.

The axial resolution (1.5 mm) is larger than the position resolution of PSD (1.2 mm). This result is due to the thickness of CdTe detectors (1 cm) and can be improved by using DOI information. Development of two dimensional position sensitive detectors is in progress in our laboratory.

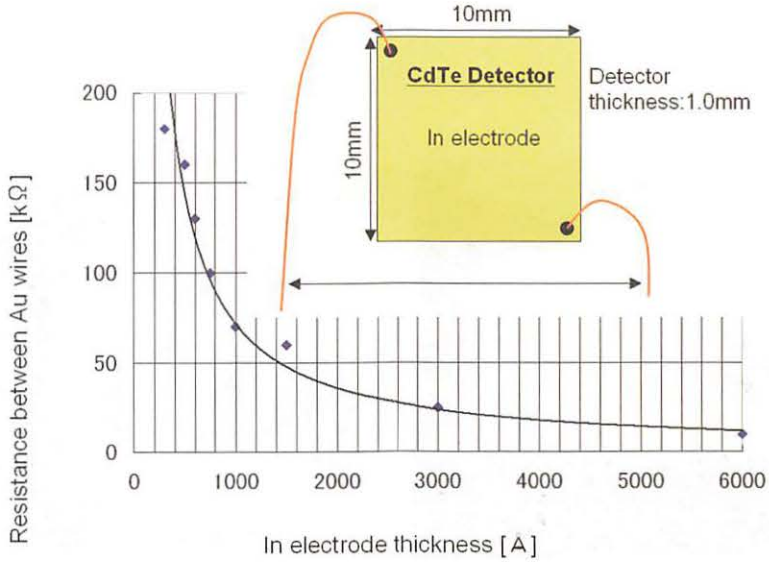

Figure 1. Resistance of In electrode as a function of its thickness.

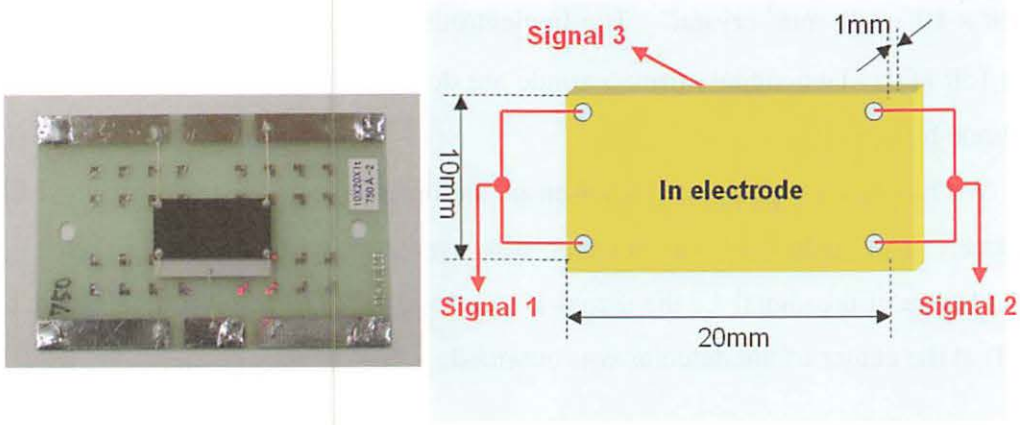

Figure 2. Photo and schematic image of 1D-PSD.

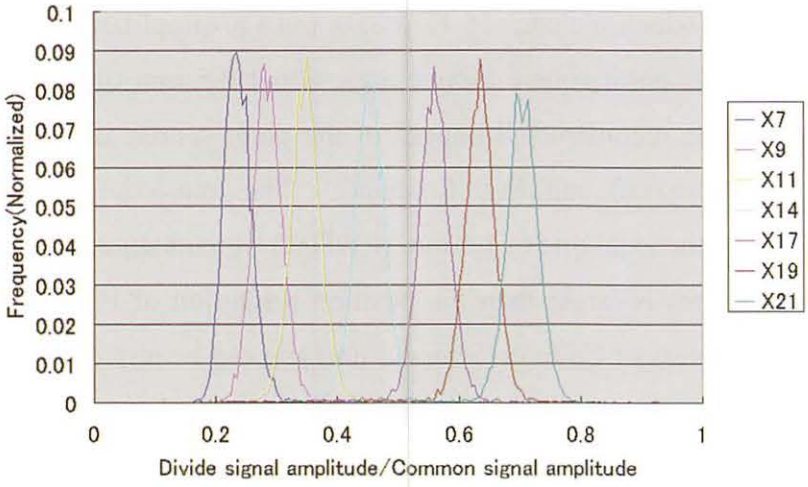

Figure 3. Position profiles of 1D-PSD.

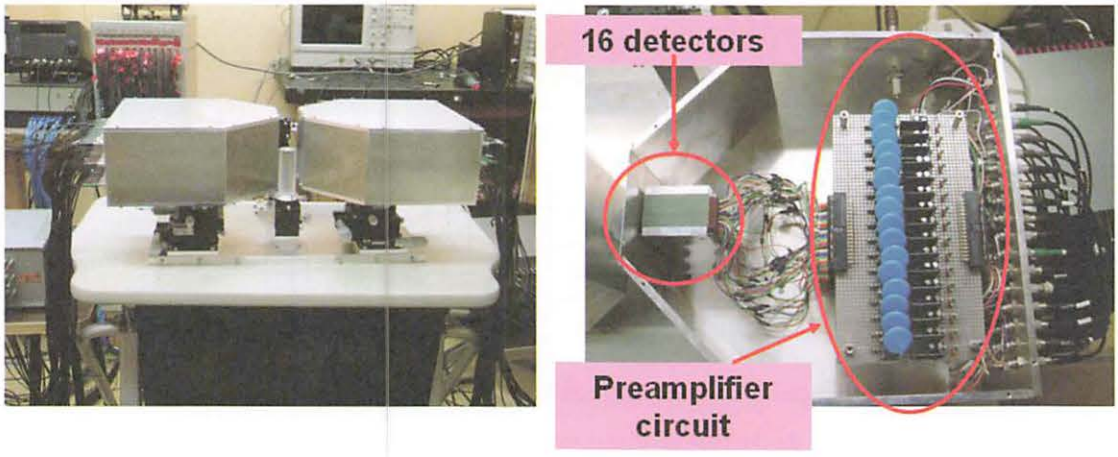

Figure 4. Detector units (left) and the inside of the unit (right).

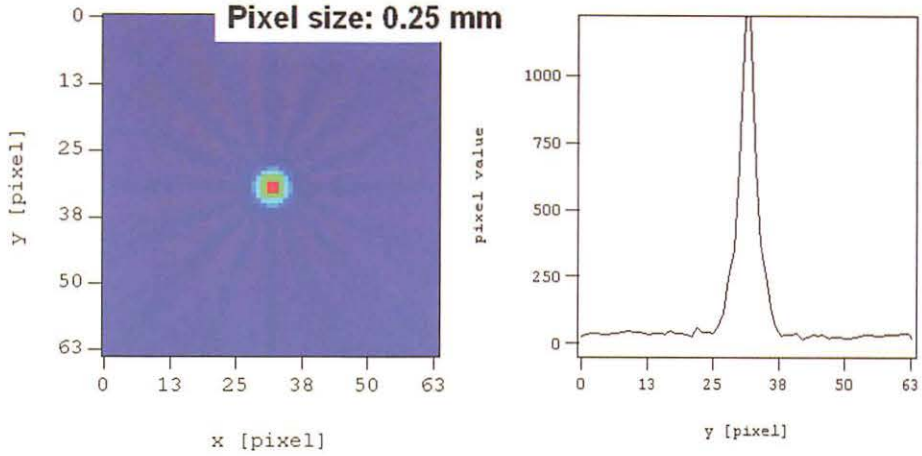

Figure 5. Reconstructed image and profile (transaxial).

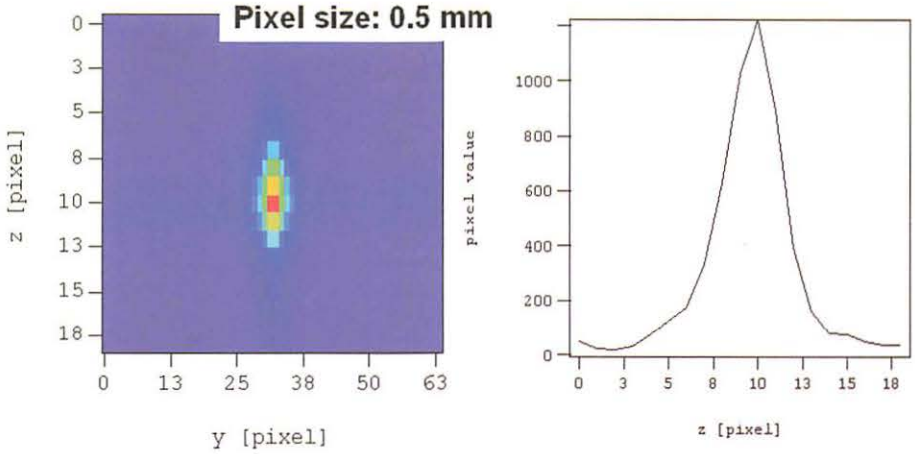

Figure 6. Reconstructed image and profile (axial).

V. PIXE AND ENVIRONMENTAL ANALYSIS

V. 1. Chemical State Analysis of Fe Compounds Using Heavy Ion PIXE

Matsuyama S., Ishii K., Yamazaki H., Kikuchi Y., Kawamura Y., Yamanaka K., and Watanabe M.

Graduate School of Engineering, Tohoku University

Introduction

Particle induced x-ray emission (PIXE) is a powerful technique for quantitative analysis. Usually proton beams with an energy around 3 MeV are used in PIXE offering high sensitivity[1]. Since chemical shift is very small and difficult to measured with conventional Si(Li) detector, high sensitive measurement with chemical state is impossible in this condition. The sensitivity of PIXE strongly depends on the X-ray production cross-sections, which are proportional to the square of the projectile charge[2], it can be expected that the use of heavy ion beams will improve the sensitivity of the analysis considerably. The lower limit of detection (LLD) in the PIXE analysis using 70 MeV carbon ions is improved 2-4 times compared to that using proton bombardment for heavier elements[3].

Since chemical change due to chemical state of the elements will be expanded due to multiple ionization, it may be measured with a conventional Si(Li) detector. In the last report, the three parameters, the relative change of an intensity ratio of k_β and k_α (Intensity Ratio), a ratio of k_β and k_α line width (line width ratio) and an energy difference between k_β and k_α line (relative energy shift), were measured using 70 MeV carbon ions and 78 MeV Ar ions. Changes in those parameters were corresponds to their chemical state. It shows that PIXE with heavy ions will lead to chemical state analysis with high-sensitivity. In this study, we applied the method to the chemical state analysis of irons. The chemical state of iron in steel will lead to the prediction of stress corrosion cracking.

Experimental

Experiment was carried out at Cyclotron Radioisotope Center. Samples are FeO, FeOOH, Fe_2O_3, Fe_3O_4. The targets were placed at an angle of 45° with respect to the

beam direction to reduce X-ray absorption in the sample. X-rays emitted from the target were measured at an angle of 90° with respect to the beam direction, by a Si(Li) detector. One mm Mylar film was placed in front of the Si(Li) detector to reduce pile-up events. The energy calibration was obtained with characteristic x-rays from a ^{241}Am source.

Results

The relative change of an intensity ratio of k_β and k_α (Intensity Ratio), a ratio of k_β and k_α line width (line width ratio) and an energy difference between k_β and k_α line (relative energy shift) is shown in Figs. 1 and 2 for carbon and Ar ion, respectively. The changes in intensity ratio are corresponding to the chemical states of the elements, while the other parameters are difficult to specify chemical state. Tendency of these parameter changes corresponds to chemical state is similar for carbon and Ar ions. Since these measurements were carried out within a few minute, PIXE with heavy ions will lead to chemical state analysis with high-sensitivity.

Acknowledgements

The authors thank the working group of the Cyclotron Radioisotope Center, Tohoku University for the operation and maintenance of the accelerator.

References

1) Johansson S.A.E., Campbell J.L., PIXE A Novel Technique for Elemental Analysis, John Wiley & Sons Ltd., (1988) p.32-33.
2) Ishii K., Orihara H., Iwata Y., Bessho K., Int. J. PIXE, **4** (1994) 1.
3) Amartaibvan Ts., Ishii K., Yamazaki H., Matsuyama S., Suzuki A., Yamaguchi T., Abe S., Inomata K., Watanabe Y., 823.1~3, http//pixe2004.ijs.si/, Proceedings of 10th international conference on PIXE and its applications, Portoroz, Slovenia, June 4-8, 2004.

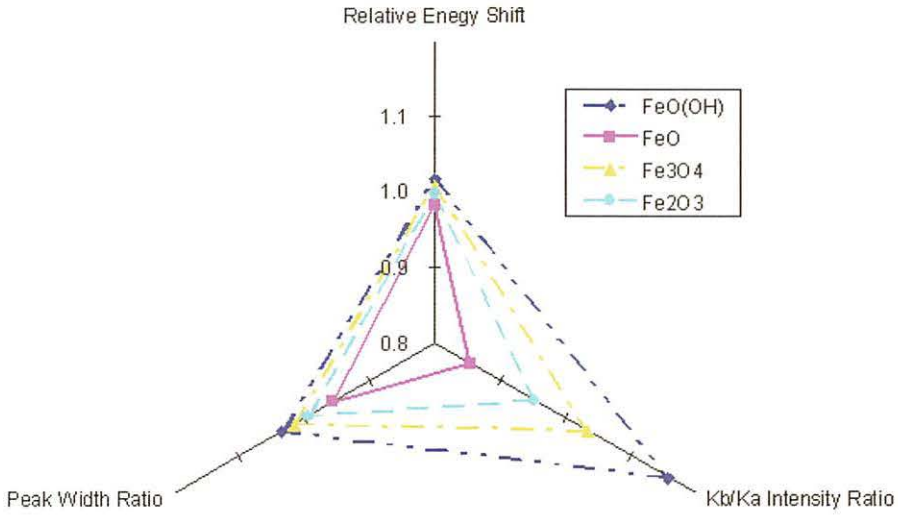

Figure 1. The relative change of an intensity ratio of k_β and k_α(Intensity Ratio), a ratio of k_β and k_α line width (line width ratio) and an energy difference between k_β and k_α line (relative energy shift) for carbon ions.

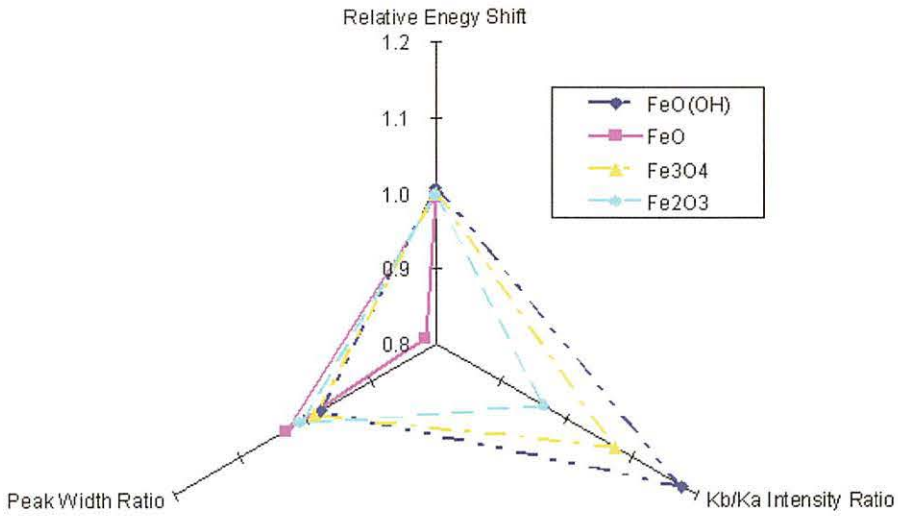

Figure 2. The relative change of an intensity ratio of k_β and k_α (Intensity Ratio), a ratio of k_β and k_α line width (line width ratio) and an energy difference between k_β and k_α line (relative energy shift) for carbon ions.

V. 2. Micro-beam Analysis of Single Aerosol Particles at Tohoku University

Matsuyama S.[1], Ishii K.[1], Yamazaki H.[1], Kikuchi Y.[1], Amartaivan Ts.[1], Abe S.[1], Inomata K.[1], Watanabe Y.[1], Ishizaki A.[1], Oyama R.[1], Kawamura Y.[1], Suzuki A.[1], Momose G.[1], Yamaguchi T.[1], and Imaseki H.[2]

[1]*Graduate School of Engineering, Tohoku University*
[2]*National Institute of Radiological Science*

Introduction

Aerosol particles are caused by sandy dust, smoke from factories, exhaust gas of cars etc., and are thereafter often deformed by photo-chemical reactions in the atmosphere[1-3]. They are characterized by physical and chemical factors such as size, volume and chemical composition, and therefore carry information on the source of origin and the kind of generating process. Especially, elemental concentrations in atmospheric aerosol reflect the pollution sources and the processes generating air pollution. Therefore, elemental analysis of atmospheric aerosols is useful to search for the sources of aerosols. The combination of aerosol collection on thin filters and PIXE analysis is one of the most effective methods for analyzing atmospheric aerosols[1)] and many studies have focused on aerosol monitoring[1-5)]. These studies were carried out analyzing bulk samples thereby averaging over many single particles. In this case, statistical models, such as the principal components analysis (PCA) and the chemical mass balance (CMB), are needed to determine the contribution of different aerosol sources[5-8)]. Therefore, analysis of single aerosol particles is superior for obtaining information on source identification and for understanding the aerosol formation mechanism[6)]. In this study, we have developed a microbeam analysis system in order to analyze the elemental composition of single aerosol particles as well as their density with 1μm spatial resolution. Furthermore, by combining PIXE with RBS, off-axis STIM and STIM methods, we are capable of analyzing all elements and can determine the chemical composition of single aerosol particles.

Experiments

Aerosol samples were collected at the campus of Tohoku University for 3 days. The sampling position is located 10 m from a road traversing Aoba campus. Sampling times were ~6 hours in daytime and ~12 hours at night. In total 6 samples were collected. Aerosol particles were impacted on a thin polycarbonate film[7] at flow rates of 0.5*l*/min (face velocity: 265 cm/sec). The effective 50% cut-off diameter is estimated to be ~3 μm. Elemental concentrations and ratios in the polycarbonate film were obtained by fitting the RBS spectrum with the SIMNRA software[8]. Thickness of the film was estimated to be less than 0.3 μm, which is consistent with the one derived from the direct STIM measurements. The uniformity of the film is better than 10%. The thin polycarbonate film allows to measure protons scattered from the sample without spectral distortion by the film in RBS and off-axis STIM measurements as well as characteristic X-rays in PIXE.

Analysis was made using the microbeam analysis system at Tohoku University. Technical details of the microbeam and analysis system were presented in previous papers[9,10] and further development was carried out for the analysis of single aerosol particles. A schematic diagram of the improved setup is shown in Fig. 1. The system is composed of two X-ray Si(Li) detectors for PIXE analysis, an annular Si surface barrier detector for RBS analysis and a Si-PIN photodiode for direct and off-axis STIM analysis. Two X-ray detectors are set in vacuum at 115 degree with respect to the beam axis. The first one has large sensitive area (60 mm^2) and is suitable for trace elemental analysis. To reduce pile-up events or deformation of the spectrum by recoil protons, a Mylar filter (200 μm) was attached to the front of the detector. Maximum solid angle is ~0.13 sr. The second detector has a high-energy resolution (~136 eV), a thin Be entrance window (7.5 μm) and ~0.02 sr and is used to detect low energy X-rays. The system is capable of detecting X-rays ranging from 1 to 30 keV with good energy resolution and detection efficiency. The annular detector is very efficient, improving solid angle (~0.15 sr) without deteriorating angular spread and without interfering with the Si(Li) detectors. Mean scattering angle is 170 degree. A Silicon PIN-photodiode, a Faraday cup and a scintillator are attached to a detector wheel off center of the beam axis (see Fig. 1) for direct and off-axis STIM measurements. In direct STIM, the wheel is turned until the detector is centered on the beam axis. Scattering angle in off-axis STIM can be changed from 10 to 35 degree by rotating the wheel.

Analysis employed the following procedure. At first, direct STIM was carried

out in a 500 × 500 μm^2 area defining the analysis area. After that, simultaneous PIXE/RBS/off-axis STIM measurements used a scanning area of 40 × 40 μm^2 to 100 × 100μm^2. Energy of the proton beam is 3 MeV and beam spot size is 1 × 1 μm^2 with a beam current of 50~100 pA. Total accumulated charge was 0.1~0.5 μC. After the measurement, direct STIM is employed once more for the same position to check for deformation of the sample. Two or three positions were analyzed for 1 sample.

Quantitative PIXE analysis was performed using the GeoPIXEII software[11]. After generating the elemental maps, particles to be analyzed were selected from these maps and PIXE, RBS and off-axis STIM spectra were extracted. Elemental composition for elements heavier than Na was deduced from fitting of the extracted PIXE spectra of single aerosol particles. In total 270 particles were analyzed and Na, Mg, Al, Si, P, S, Cl, Ca, Ti, Mo, Fe, Ni, Cu, Zn and Br elements were quantified.

Quantitative analysis of hydrogen was carried out by analyzing the extracted off-axis STIM spectra. Figure 2 shows typical off-axis STIM spectra from an aerosol particle compared with spectra from the backing film. The intensity of protons scattered from the backing is very low compared to scattering from aerosol particles and is thus easily subtracted. The scattering angle was set to 28 degrees, which suffices to separate proton peaks scattered from heavy elements and from hydrogen even in a thickness of 50 μm of organic film. While intensity of scattered protons decreases with increasing scattering angle, the counting rate of hydrogen at 28 degrees is sufficient for analysis. For the quantitative analysis of hydrogen, intensities of hydrogen were calibrated by measuring hydrogen yields from polycarbonate films of different thickness. The relation between hydrogen peak yield and hydrogen quantity is linear and is used to calibrate the quantitative analysis of hydrogen.

Light elements (C,N,O) were quantified by analyzing the extracted RBS spectra. Figure 3 shows RBS spectra for an aerosol particle compared with spectra from the backing. For the analysis of single aerosol particles, a similar analysis by using SIMNRA software might be efficient for quantitative analysis. However, samples might not be uniform even in a single aerosol and experimental scattering cross sections are scarce for major elements of aerosols. Therefore, concentration of carbon and oxygen were derived from peak yields which were calibrated by measuring peak yields from polycarbonate films of known thickness. Since scattering cross section of C(p,p)C and O(p,p)O for 3 MeV to 2.8 MeV are constant within 5%[12], this method is effective for quantitative analysis if peaks from the

sample are well separated and nitrogen is thus not included in yields. Since carbon peak and oxygen peak in the RBS spectra overlap when energy loss is larger than 100 keV, particles whose energy losses were larger than 100 keV were excluded. Even if energy loss was below 100 keV, spectra with overlapping peaks were excluded as nitrogen may be included. In the present analysis, 70 particles were excluded.

Results

Figure 4 shows typical elemental and direct STIM maps with a micrograph and scale. The direct STIM map shows the density distribution corresponding to the micrograph. Direct STIM is then used to define the position of analysis. Elemental loss was not observed. The elemental distribution of Al equals to the one of Si, originating mainly from soil dust of Alumino-Silicate particles. Ca and S elements also show similar distributions and may originate from $CaSO_4$ particles. Na, Mg and Cl elements come from marine aerosols, and shows similar distributions. The light elements, hydrogen and carbon show similar distribution, and all these particles are clustered into Si-rich, Ca-rich and Fe-rich and marine aerosols groups, according to their major elements. The soil and marine aerosols are 60% and 20% of total particles, respectively.

Correlation functions between Ca and S and between Ca and O are shown in Figs. 5 and 6. As Ca increases, both S and O increase. Especially, particles whose sum of Ca and S mass is higher than 50% of the total mass are well correlated. Correlation between Ca and H also shows similar trend. Ca, S, O and H are well correlated and atomic ratio of Ca:S:O:H is 1:0.7:12:12 for these particles. These particles appear to contain $CaSO_4$ particles. Since $CaSO_4$ is stable in the presence of H_2O, the ratio of O to Ca is higher than 4, because H_2O is also present in $CaSO_4(H_2O)_n$.

Figure 6 shows correlation between H and C. C increases as H increases and the atomic ratio is around 1. Figure 7 shows atomic percentage of H and C. Total mass of aerosol particles was derived from the sum of H, C and O mass after background subtraction of polycarbonate backing. Data are distributed around the line which shows atomic ratio of 1. Atomic ratio of oxygen is 0.1 to 0.5. It may imply that organic material is based on aromatic series mixed with -COOH radical.

Conclusions

We have developed a microbeam analysis system in order to analyze single aerosol particles with 1μm spatial resolution. By combining PIXE with RBS, off-axis STIM and

direct STIM methods and by using thin backing film, we can quantify single aerosol particles containing elements from hydrogen to heavy metals, thus revealing the chemical composition of these particles. The chemical composition provides information on source identification and leads to better understanding of the aerosol formation mechanism. The described micro-beam analysis system represents a powerful research tool for aerosol particles, emission source identification and for a better understanding of the aerosol formation processes.

Acknowledgements

This study was partly supported by Grant-in-Aid for Scientific Research (S) No. 13852017 and Grant-in-Aid for Scientific Research in Priority Areas under Grant No.14048213 from the Ministry of Education, Culture, Sports, Science and Technology, Japan. The authors would like to thank Mr. K.Komatsu, T.Nagaya and C.Akama for their help in constructing the microbeam and target system.

References

1) Ariola V. et. al., *Nucl. Instr. and Meth.*, **B190** (2002) 471.
2) Parti P. et. al., *Atmospheric Environment*, **34**, 3 (2000) 149.
3) Bongiovanni S.F. et. al., *Nucl. Instr. and Meth.*, **B161-163** (2000) 786.
4) Cohen D.D, *Nucl. Instr. and Meth.*, **B136-138** (1998) 14.
5) Formenti P., Annegarnand H.J., Piketh S.J., *Nucl. Instr. and Meth.*, **B136-138** (1998) 948.
6) Orlic I., Osipowicz T., Watt F., Tang S.M., *Nucl. Instr. and Meth.*, **B104** (1995) 630.
7) Yamazaki H., Tsutsumi K., Ishii K., Matsuyama S., Murozono K., Inoue J., Iwasaki S., *Int. J. of PIXE*, **7**(1&2) (1997) 101.
8) Mayer M., SIMNRA Users's Guide, Technical Report IPP 9/113, MPI Plasmaphysik, Garching, Germany, 1997.
9) Matsuyama S., Ishii K., Yamazaki H., Sakamoto R., Fujisawa M., Amartaivan Ts., Ohishi Y., Rodriguez M., Suzuki A., Kamiya, T. Oikawa M., Arakawa K., Matsumoto N., *Nucl. Instr. and Meth.* , **B210** (2003) 59.
10) Matsuyama S., Ishii K., Yamazaki H., Barbotteau, Y. Amartivan Ts., Izukawa D., Hotta K., Mizuma K., Abe, S. Oishi Y., Rodriguez M., Suzuki A., Sakamoto R., Fujisawa M., Kamiya T., Oikawa M., Arakawa K., Imaseki H., Matsumoto N., *Int. J. of PIXE*, **14** (1&2) (2004) 1.
11) Ryan C.G., Van Achterbergh E., Yeats C.J., Drieberg S.L., Mark, G. McInnes B.M., Win T.T., Cripps G., Suter, G.F., *Nucl. Instr. and Meth.*, **B188** (2002) 18.
12) Amirikas R., Jamieson D.N., Dooley S.P., *Nucl. Instr. and Meth.*, **B77** (1993) 110.

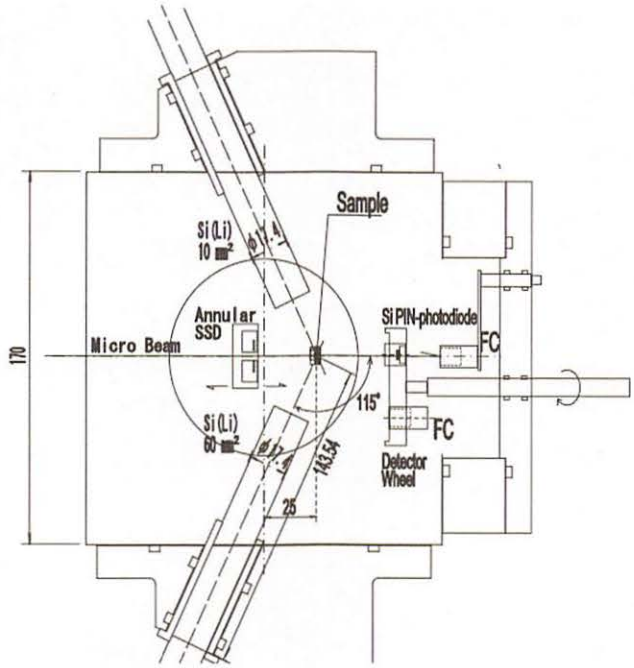

Figure 1. Schematic diagram of the analysis system.

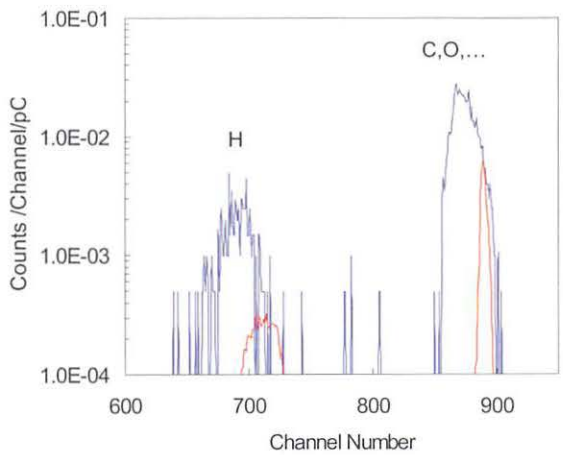

Figure 2. Typical off-axis STIM spectra from an aerosol particle (-) and from a backing film (-).

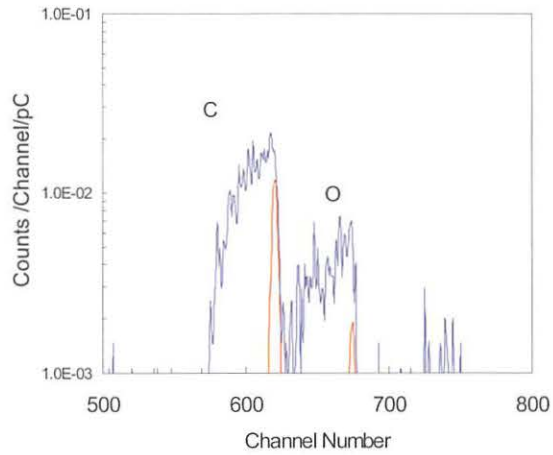

Figure 3. RBS spectra from a aerosol particle (-) and from a backing film (-).

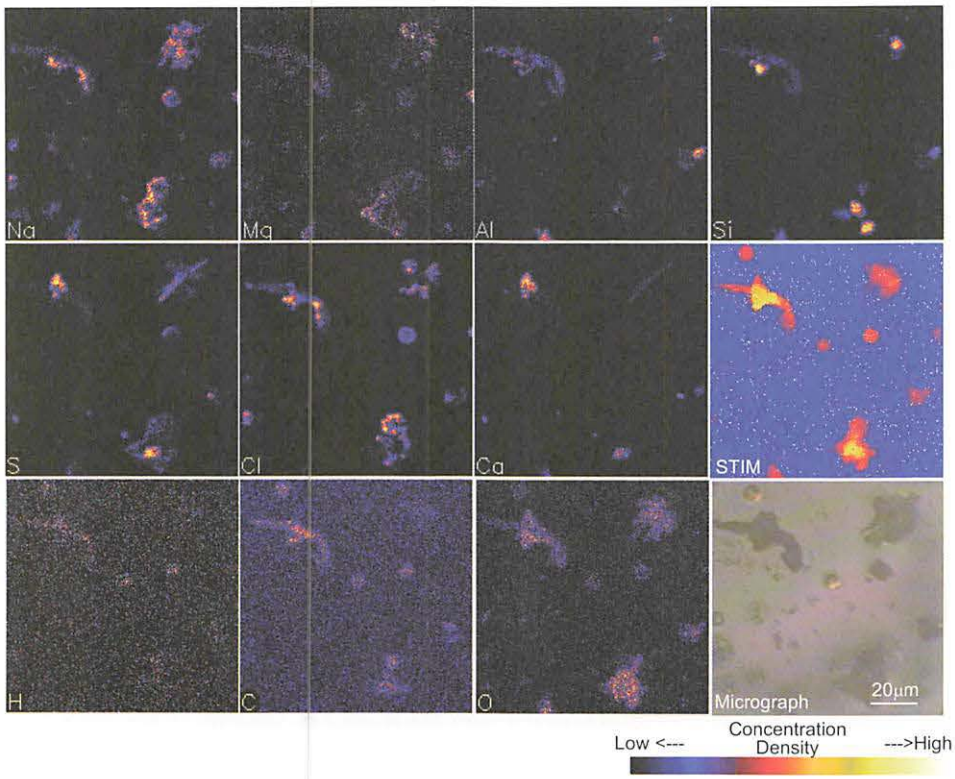

Figure 4. Typical elemental maps with a micrograph.

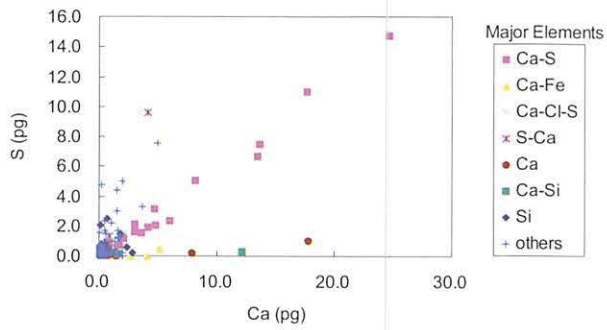

Figure 5. Correlation between Ca and S.

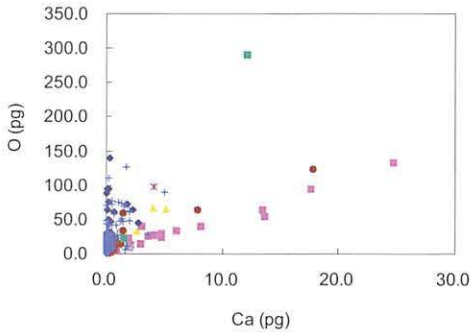

Figure 6. Correlation between Ca and O.

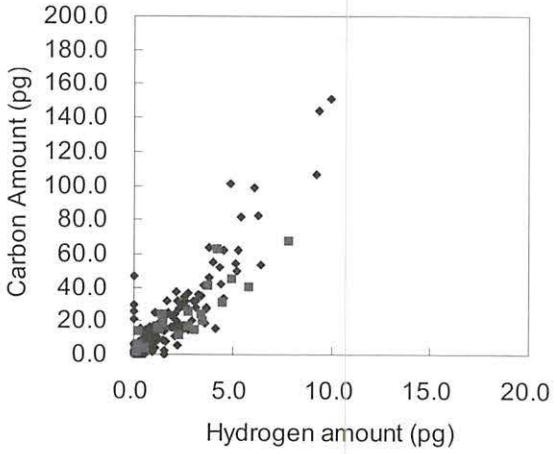

Figure 7. Correlation between H and C.

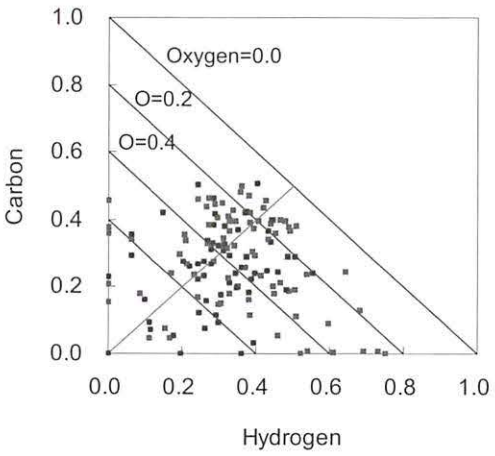

Figure 8. Atomic percentage of H and C.

V. 3. Development of an In-air on/off Axis STIM System for Quantitative Elemental Mapping

Inomata K.[1], Ishii K.[1], Yamazaki, H.[1], Matsuyama, S.[1], Kikuchi Y.[1], Watanabe Y.[1], Ishizaki A.[1], Oyama R.[1], Kawamura Y.[1], Yamaguchi T.[1], Momose G.[1], Sakurai E.[2], Yanai K.[2], Kamiya T.[3], Sakai T.[3], Satoh T.[3], Oikawa M.[3], and Arakawa K[3].

[1]Department of Quantum Science and Energy Engineering, Tohoku University,
[2]Department of Pharmacology, Tohoku University
[3]Takasaki Advanced Radiation Research Institute, Japan Atomic Energy Agency

Introduction

Micro-PIXE has been recognized as a powerful tool for analyses of single-cell and tissue sections in biological and biomedical studies[1-3]. We have developed in-air micro-PIXE systems at the Japan Atomic Energy Agency (JAEA) Takasaki[4,5] and at Tohoku University[6,7] and have analyzed bovine aortic endothelial (BAE) cells, rat basophilic leukemia (RBL) cells, and tumor cells AH109A implanted into Donryu rat[8-10].

Micro-PIXE allows quantitative analyses of spatial distribution of elements in the microscopic region if physical parameters such as the X-ray production cross-sections, the efficiency and the solid angle of an detector are known. In this case, spatial distribution of elements is shown as areal density with appropriate units (e.g. $\mu g/cm^2$). For analysis of biological samples, mass normalization is necessary because of the difference in shape or thickness. Furthermore, it is necessary to correct X-ray self-absorption considering elemental concentrations, thickness, and sample density. Although in-air analysis imparts less damage during beam irradiation[11], morphological changes occasionally occur by beam irradiation. In our previous study, cell thickness or density is reduced to ca. 60% of the initial value after beam irradiation (beam currents of ca. 40 pA, a beam spot size of 1×1 μm^2, scanning area of 20×20 μm^2 and accumulated charge of 177 nC)[12]. In this case, the cell density should be monitored simultaneously using PIXE analysis and the yield correction of X-rays should be done according to the irradiation dose. Therefore, the shape of samples must be monitored during analysis, which should be reflected in the yield correction.

Micro-Rutherford Backscattering Spectroscopy (Micro-RBS) and Scanning Trans

Transmission Ion Microscopy (STIM) are widely used for those purposes. Micro-RBS shows the distribution of light elements as well as the thickness distribution in the sample. However, the inhomogeneous distribution of the thickness engenders a large spread in the RBS spectrum and prevents rapid and simple analysis[13]. For density mapping, STIM is also useful. Transmitted ions are detected directly. For that reason, a very low current is sufficient for structural mapping. Hence, elemental mapping and density mapping cannot be carried out at the same time. Using off-axis and on/off axis geometry for STIM, we can perform simultaneous density mapping in PIXE analysis[14]. In the off-axis geometry, a detector is set off-axis to the beam direction. In on/off-axis geometry, scattered ions from a thin scattering foil downstream of the sample are detected. The off-axis STIM has an inherent disadvantage in spectrum deformation by kinematics. The on/off axis STIM geometry combines advantages of both STIM and off-axis STIM[15].

In the present study, an on/off axis STIM system is newly combined with our in-air micro-PIXE systems and is used for the yield correction of X-rays and for mass normalization.

In-Air On/Off axis STIM System

Details of the in-air PIXE system are presented in previous papers[5,8,9]. Proton beams of 3 MeV are extracted through a polycarbonate film (5 μm), which serves as a backing film of the sample. Beam broadening through the film is estimated to be less than 0.01 μm and does not degrade beam quality to any great degree. Fig. 1. shows a schematic diagram of the in-air on/off axis STIM system. In on/off axis STIM, transmitted ions are scattered by a scatterer downstream and detected by a particle detector. A thin foil of a heavy metal is favorable as a scatterer to reduce energy broadening by kinematics and energy straggling. However, the heavy metal element causes X-ray background in PIXE analysis. Carbon (50 $\mu g/cm^2$) or aluminum (177 $\mu g/cm^2$) foils were used in this study. The thin scattering foil is placed 13-mm downstream of the sample. Scattered protons are detected by a Si-PIN photodiode that is set at 30 degrees with respect to the beam axis. A 1 mm ϕ and 20 mm long collimator was used to define the scattering angle. These components were set in a chamber filled with He gas to reduce energy loss, scattering and sample damage[11,16].

Figure 2. shows typical on/off axis STIM spectra of 5 μm polycarbonate film scattered by carbon and Al foils. Total accumulated charges were 2.3 μC and 7.6 μC,

respectively, for carbon and Al foils. Two scattered proton peaks are visible in both spectra. These peaks respectively correspond to the protons scattered by He gas and the scattering foil. The scattering angle of 30 degrees suffices to separate proton peaks scattered from He and from foils. The intensity of the scattered protons from Al is higher than that from carbon, which corresponds to the difference of scattering cross sections and foil thickness. Measured energy broadening of scattering protons from carbon and Al foils were, respectively, 41 keV and 38 keV, including an energy resolution of Si-PIN photodiode (ca. 14 keV). Energy broadening is caused mainly by energy straggling in He gas. Proton peak scattered by He gas is shown in both spectra. Intensity of the peak scattered by He gas is higher than that from carbon. However, energy broadening is 48 keV; He gas is not useful as a scatterer. The Al foil is superior to the carbon foil in both energy spread and intensity. Therefore, we used the Al foil as a scatterer.

Figure 3 depicts the PIXE spectrum of RBL-2H3 cells measured simultaneously with on/off axis STIM. Neither characteristic X-rays nor the Compton background caused by Al(p,γ) reaction deform the PIXE spectrum.

The sample mass is obtained by converting transmitted ion energy based on scattering geometry. For a microbeam analysis, transmitted ion energy must be determined pixel by pixel. Considering low counting statistics for each pixel, spectrum fitting is not effective. The median value of the peak energy represents practical energy for the analysis of a low statistical spectrum. Therefore, we use the median value for determination of transmitted ion energy[17]. Transmitted ion energy is converted into the sample mass using Bethe's rule if the chemical composition of the sample is known. Composition of the biological sample is mainly light elements, as measured using RBS. The amount of hydrogen, which can not be determined by RBS, was referred to the value from ref[18]. In the case of biological samples composed of light elements, Z/A of the light elements equals 1/2, except for hydrogen. Since the mass concentration of hydrogen is on the order of 10%[18], areal density ($\mu g/cm^2$) can be determined within an error of 15% even if the sample composition is not known. The thickness is determined from the transmitted ion energy and the resolution of areal density is estimated from the error in determining peak energy that depends strongly on counting statistics. Figure 4. shows variation of the energy determined by median values for different counts of 1, 3 and 11, which was measured with the on/off axis geometry for polycarbonate film of constant thickness of 5 μm. The standard deviation of the determined energy decreases as the counts increase.

Even for 11 counts, the standard deviation is 6 keV, which corresponds to 50 μg/cm^2.

The mass loss of polycarbonate film by beam irradiation was measured using the on/off axis STIM system. The behavior of polymer film under beam irradiation is comparable to biological samples[19]. Therefore, the measurement is suitable to check the applicability to damage monitoring in cell analysis. Measurement was carried out with 3 MeV proton beams, beam current of 500 pA, a beam spot size of 2 × 2 μm^2 and scanning area of 200 × 200 μm^2. The shift of transmitted ion energy as a function of irradiated charge is shown in Fig. 5. Although the standard deviation is rather large, increase of the transmitted ion energy is apparent as an increase of irradiated charge. It shows that the system is applicable to damage monitoring in cell analysis.

Quantitative imaging

The areal density map of RBL-2H3 cells is obtained using the on/off axis STIM system (Fig. 6). Measurement was carried out with beam spot size of 1 × 1 μm^2, beam currents of 100 pA and scanning area of 100·100 μm^2. The total accumulated charge was 790 nC. The density is high in the cell center, indicating that the cells maintain a round shape. The cells distribute in the density of 500–900 μg/cm^2. The yield correction of X-rays should be performed pixel by pixel considering the varied areal densities. Changes in X-ray production cross section corresponding to energy loss in the sample must also be considered. However, the variation of the cell density is, at most, 500 μg/cm^2, which corresponds to an energy change of less than 50 keV in the cells. Therefore, the change in X-ray production cross section is negligible and the X-ray yield (Y) with self-absorption in the sample is given as the following.

$$
\begin{aligned}
Y &= \frac{Y_0}{\Delta X}\int_0^{\Delta X} \exp(-\mu_m \cdot \rho \cdot t/\cos\theta)\cdot dt \\
&= \frac{Y_0}{\Delta X}\left[\frac{1-\exp(-\mu_m \cdot \rho \cdot \Delta X/\cos\theta)}{\mu/\cos\theta}\right] \\
&\cong Y_0\left[1-\frac{\mu_m \cdot \rho \cdot \Delta X}{2\cos\theta}\right]
\end{aligned}
$$

In that equation: Y_0, initial X-ray yield; μ_m, sample mass attenuation coefficient; ρ, density; ΔX, sample thickness; and θ is the exit angle. In this calculation, the mass attenuation coefficient μ_m of the sample must be known as well as density. The mass attenuation

coefficient of the sample is obtainable considering the matrix of the sample. Composition of the sample was measured using RBS. The amount of hydrogen was referred to the value from ref.[18]. Figure 7 shows typical transmittance from RBL-2H3 cells for characteristic X-rays of Na, Al, P, and Ca. The transmittance is strongly dependent on the sample shape and X-ray energies. Although the X-ray yield from Ca is not affected by self-absorption, more than 50% of X-rays from Na is absorbed in the sample because transmittance of P X-rays is around 80–90%, which depends on the sample thickness. Yield correction is effective for such light elements.

The areal density maps of elements [μg/cm^2] were converted into the mass concentration map [μg/g] by dividing them by the measured matrix distribution. Figure 8 shows the areal density and the mass concentration maps of P, Ca, and Br for RBL-2H3 cells. The distribution of P is strongly related to the cell density. Therefore, concentration of P is uniform in the cell region. On the other hand, Br is concentrated in the nucleus, even in the mass concentration map. The Br accumulation in the nucleus is first confirmed in mass concentration using the on/off axis STIM and PIXE system.

Summary

We have developed the in-air on/off axis STIM system for simultaneous density mapping with PIXE and RBS, which will be useful for damage monitoring, for yield correction of X-rays, and for mass normalization in cell analysis. Using this system, areal density mapping is carried out in this study for RBL-2H3 cells simultaneously with PIXE and RBS. Correction for self-absorption is performed and the areal density map of elements is converted into a mass concentration map using the measured matrix density. The areal density distribution of P corresponds to that of the matrix and the mass concentration of P is uniform in the cell region. On the other hand, Br is concentrated in the nucleus even in the mass concentration map. The Br accumulation in the nucleus is first confirmed in the mass concentration using the on/off axis STIM and PIXE system. The in-air on/off STIM system will be effective for monitoring changes in cell density during beam irradiation.

Acknowledgements

This study was partly supported by Grants-in-Aid for Scientific Research (S) No. 13852017, (C) No. 16560731, and a Grant-in-Aid for Scientific Research in Priority Areas

under Grant No. 14048213 from the Ministry of Education, Culture, Sports, Science and Technology, Japan. The authors appreciate the help of K. Komatsu, T. Nagaya and C. Akama in constructing the on/off STIM system.

References

1) Moretto Ph., Y.Labador, Nucl. Instr. and Meth. **B130** (1997) 324.
2) Labador Y., Ph.Moretto, Applications of Nuclear Microprobes in the Life Science, Singapore: World Scientific, 1998.
3) Hogarth A.N., Thong P.S.P., Lane D.J.W., Watt F., Nucl. Instr. and Meth. **B130** (1997) 402.
4) Matsuyama S., Ishii K., Sugimoto A., Satoh T., Gotoh K., Yamazaki H., Iwasaki S., Murozono K., Inoue J., Hamano T., Yokota S., Sakai T., Kamiya T., Tanaka R., Int. J. of PIXE **8** (1998) 203.
5) Sakai T., Hamano T., Hirao T., Kamiya T., Murozono K., Inoue, J. Matsuyama S., Iwasaki S., Ishii K., Nucl. Instr. and Meth. **B136-138** (1998) 390.
6) Matsuyama S., Ishii K., Yamazaki H., Sakamoto R., Fujisawa M., Amartaivan Ts., Ohishi Y., Rodoriguez M., Suzuki A., Kamiya T., Oikawa M., Arakawa K., Matsumoto N., Nucl. Instr. and Meth. **B210** (2003) 59.
7) Matsuyama S., Ishii K., Yamazaki H., Barbotteau Y., Amartivan Ts., Izukawa D., Hotta K., Mizuma K., Abe S., Oishi, Y. Rodriguez M., Suzuki A., Sakamoto, R. Fujisawa M., Kamiya T., Oikawa M., Arakawa K., Imaseki H., Matsumoto N., Int. J. PIXE **14** (2004) 1.
8) Ishii K., Sugimoto A., Tanaka A., Satoh T., Matsuyama S., Yamazaki H., Akama C., Amartiva T., Endoh H., Oishi Y., Yuki, H. Sugihara, S. Satoh M., Kamiya T., Sakai T., Arakawa K., Saidoh M., Oikawa S., Nucl. Instr. and Meth. **B181** (2001) 448.
9) Sugimoto A., Ishii K., Matsuyama S., Satoh T., Gotoh K., Yamazaki H., Akama C., Int. J. PIXE **9** (1999) 151.
10) Tanaka A., Ishii K., Komori Y., Matsuyama S., Satoh T., Gotoh K., Yamazaki H., Akama, C. Int. J. PIXE **12** (2002) 79.
11) Komori H., Mizuma, K. Ishii, K. Yamazaki H., Matsuyama S., Amartaivan Ts., Ohishi Y., Rodriguez M., Suzuki A., Satoh, M. Kamiya T., Sakai, T. Satoh T., Oikawa M., Arakawa K., Int. J. of PIXE **14** (2004) 75.
12) Matsuyama S., Ishii K., Abe, S. Ohtsu H., Yamazaki H., Kikuchi Y., Amartaivan Ts., Inomata K., Watanabe Y., Ishizaki A., Barbotteau Y., Suzuki A., Yamaguchi T., Momose G., Imaseki H., Int. J. PIXE **15** (2005) 41.
13) Moretto Ph., L.Razafindrabe, Nucl. Instr. and Meth. **B104** (1995) 171.
14) Pallon J., Elfman M., Kristiansson P., Malmqvist K., Graneli E., Sellborn A., Karlsson C., Nucl. Instr. and Meth **B158** (1999) 312.
15) Pallon J., Auzelyte V., Elfman M., Garmer M., Kristiansson P., Malmqvist K., Nilsson C., Shariff A., Wegden M., Nucl. Instr. and Meth. **B219-220** (2004) 988.
16) Barbotteau Y., Ishii K., Mizuma K., Yamazaki H., Matsuyama S., Sakai T., Satoh T., Kamiya T., Int. J. PIXE **14** (2004) 19.
17) Maetz M., Przylowicz W.J., Mesjasz-Przybylowicz J., Schubler A., Traxel K., Nucl. Instr. and Meth. **B158** (1999) 292.
18) Frausto da Silva J.J.R., Williams R.J.P., The Biological Chemistry of the Elements, The Inorganic Chemistry of Life, Oxford, U.K., Clarendon Press, 1991.
19) Themner K., Spanne P., Jones K.W., Nucl. Instr. and Meth. **B49** (1990) 52.

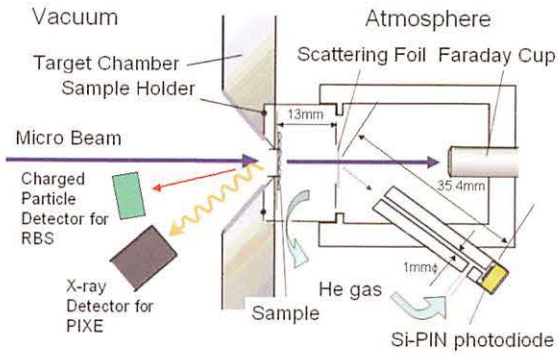

Figure 1. Schematic Diagram of on/off axis STIM.

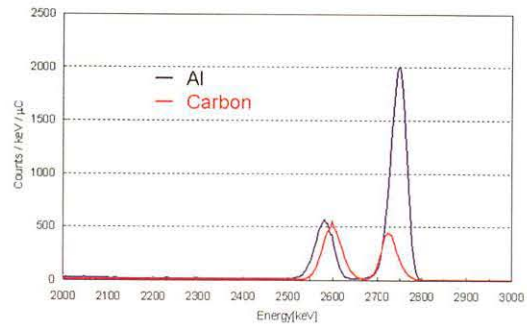

Figure 2. On/off axis STIM spectra for different scattering foil.

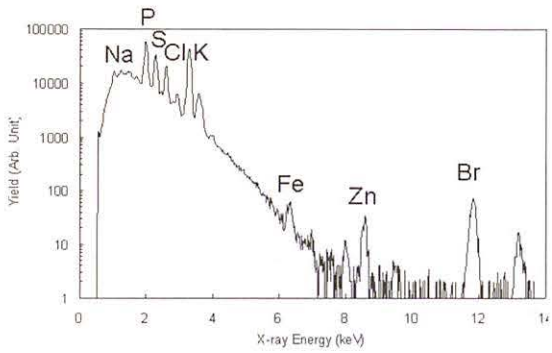

Figure 3. PIXE spectrum of RBL-2H3 cell measured simultaneously with on/off axis STIM.

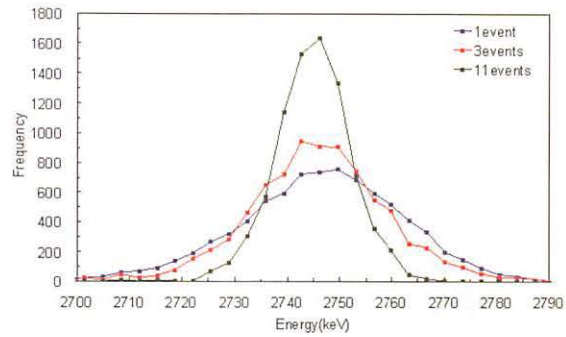

Figure 4. Variation of peak energy for different counting statistics.

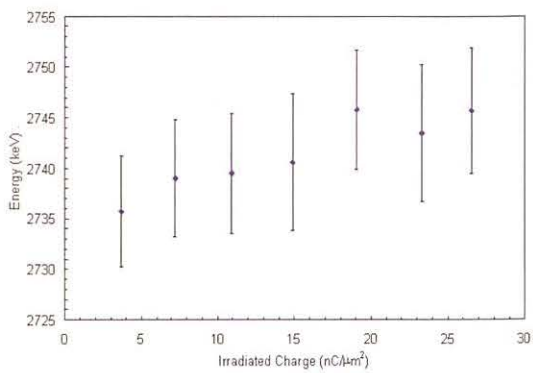

Figure 5. Shift of transmitted ion energy during beam irradiation.

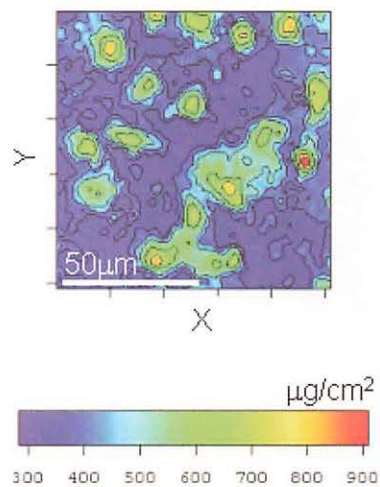

Figure 6 . Areal density map of RBL-2H3 cells.

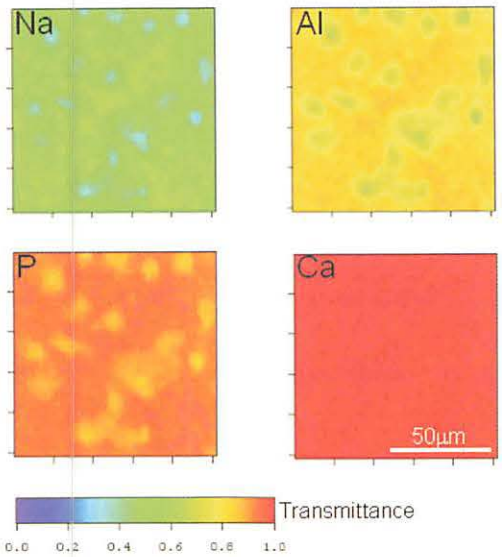

Figure 7. Transmittance from RBL-2H3 cells for characteristic X-rays of Na, Al, P, and Ca.

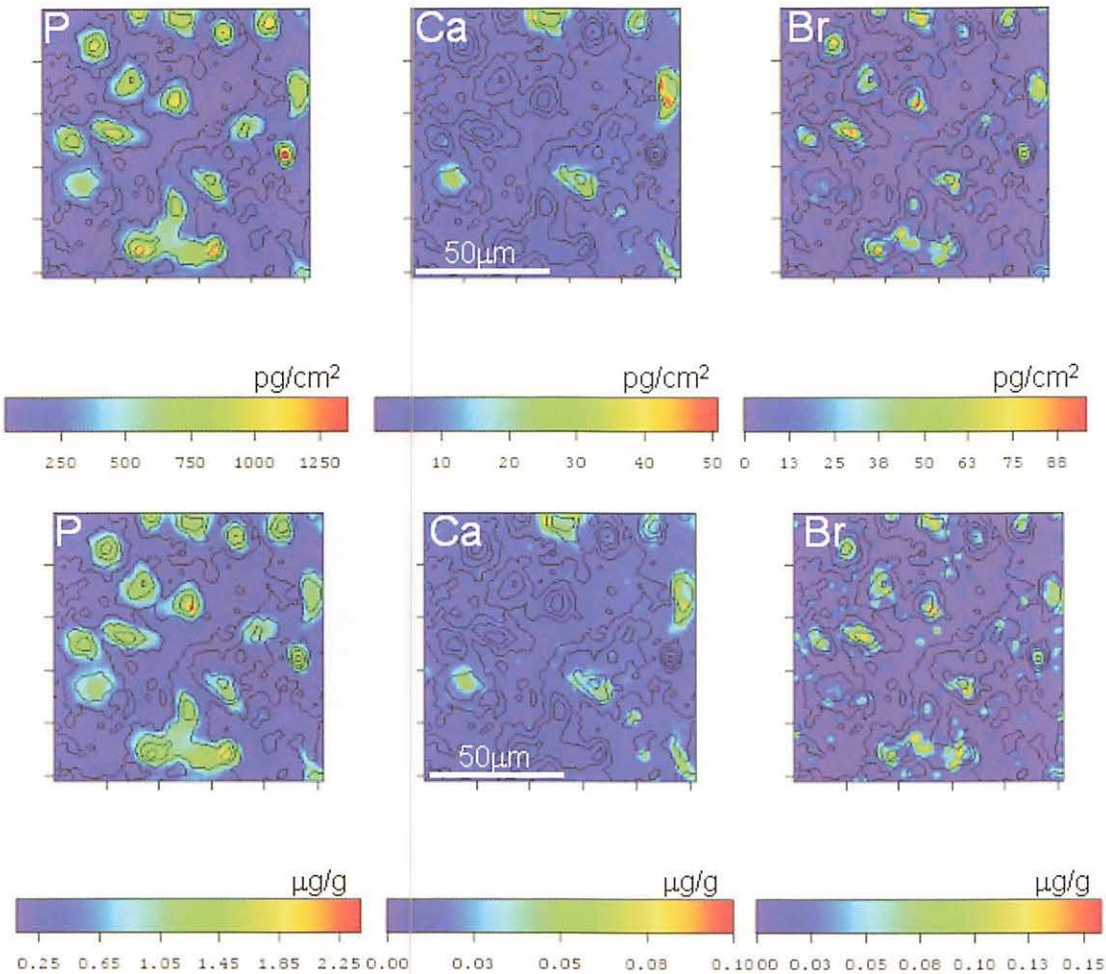

Figure 8. Elemental distribution images.

(Upper, areal density map of elements [μg/cm²]; lower, mass concentration map [μg/g])

VI. RADIOCHEMISRTY AND NUCLEAR CHEMISTRY

VI. 1. Half-life Measurement of ^{7}Be in Different Chemical and Physical Environments

Ohtsuki T. and Kasagi J.

Laboratory of Nuclear Science, Tohoku University

The constancy of nuclear half-life has been firmly established experimentally as an exponential decay law. However, in one of β-decay modes, electron-capture (EC) decay rate depends on the density of atomic electrons within the nucleus as first suggested by Segr'e et al[1]. The general understanding is that the wave function of the initial and final states between atomic electrons and the nucleus, respectively, should be considered in the EC decay. Therefore, external factors such as chemical form, metal host, pressure, and even temperature may alter the densities of the electron overlap with the nucleus, and thus, affect the EC decay rates. A long-standing debate exists regarding to what degree nuclear decay rates can be changed artificially. The EC decay nucleus ^{7}Be has been used to look for effects of external-electron density on decay half-lives, because of its simple electronic structure ($1s^2 2s^2$) in neutral Be atom and its adequate half-life for measurement. So far, the success of the ^{7}Be endohedral C_{60} (^{7}Be@C_{60}) and ^{7}Be in Be metal [Be metal (^{7}Be)] has allowed us to measure the half-life of ^{7}Be. Then, we have measured the half-life of ^{7}Be in the sample of ^{7}Be@C_{60} and Be metal (^{7}Be) by using a reference method and standard clock time. It was revealed that the half-life of ^{7}Be inside C_{60} was almost 1 % shorter than that in Be metal in room temperature. This fact implied that the ^{7}Be atoms are located in a unique environment inside C_{60}[2].

Several factors contribute to this environment: the many π electrons and dynamic motion etc. inside fullerenes (at room temperature). Therefore, it is intriguing to study the temperature and the cage (C_{60}, C_{70}) dependence of the half-life of ^{7}Be inside C_{60} (and C_{70}). In the present study, in order to look for the effects of the dynamic motion of ^{7}Be inside C_{60} (C_{70}), we measure the half-life of ^{7}Be in the sample of ^{7}Be@C_{60} and ^{7}Be@C_{70} that had been cooled to a temperature close to liquid helium (T=5K).

One way to produce atom endohedral C_{60} (C_{70}) is to insert foreign atoms into preexisting C_{60} (C_{70}). We produced an endohedral C_{60} (C_{70}) by nuclear recoil implantation[3,4]. Recently, we developed a reference method to measure the half-life of ^{7}Be inside C_{60} (C_{70}) and that in Be metal. The method used to produce the ^{7}Be@C_{60} (C_{70}) and ^{7}Be reference samples (Be metal (^{7}Be) has been described elsewhere[2]. In order to measure the half-life at T=5K, the ^{7}Be@C_{60} (C_{70}) sample was placed in the top of a He closed-cycle cryostat. The two samples, ^{7}Be@C_{60} (C_{70}) (fastened in the cryostat) and Be metal (^{7}Be), were placed in a computer-controlled sample changer, which moved the samples precisely in front of a γ-ray detector. The measurement was started after the ^{7}Be@C_{60} (C_{70}) sample underwent sufficient cooling at T=5K in the vacuum state. This arrangement allowed the decay rates of the two samples to be measured in a consistent fashion while reducing systematic errors. In the system, the internal clock time of the computer for data acquisition was constantly calibrated by a time-standard signal distributed via a long-wave radio center in Japan. The 478 keV γ-rays emanating from the EC-decay daughter (the first excited state of ^{7}Li) of ^{7}Be were measured using a HPGe detector coupled to a 4096-channel pulse-height analyzer. Here, we set the specific measurement duration to 21600 seconds (21480 seconds for the live measurement time and 120 seconds for the dead-time of the measurement system plus the sample exchange) for one data point. The amount of radioactivity associated with the decay of ^{7}Be (E_γ=478 keV) could be uniquely analyzed through the identification of characteristic γ-rays. The decay curves obtained in the present measurements were fitted, by use of the MINUIT program distributed by the CERN Program Library. The uncertainty of our measurement corresponds to that of the slope of the straight line fitted to the logarithm of the counts (i.e., counts per second) of the decay curve. The reduced chi-square values of the exponential fits are between 0.9 and 1.1. The uncertainty due to the dead time was estimated to be less than 0.04%, and the systematic error in the measurements was estimated to be less than half of the statistical errors.

We have measured the decay rates and deduced the corresponding half-lives of ^{7}Be in samples of ^{7}Be@C_{60} at T=5K and 293K, ^{7}Be@C_{70} at T=293K and in Be metal(^{7}Be) at T=293K with durations of almost three half-lives of ^{7}Be. In Fig. 5, the open circles indicate the half-lives obtained for the ^{7}Be@C_{60} sample at T=5K and the closed squares for the ^{7}Be@C_{60} at T=293K, the closed circle for the ^{7}Be@C_{70} at T=293K, further, the cross symbols for the Be metal(^{7}Be) at T=293K. The half-lives in these samples are indicated in

the figure. It was surprising to note that the half-life of ^{7}Be in the ^{7}Be@C_{60} at T=5K and that in the Be metal(^{7}Be) at T=293K was dramatically different by almost 1.5% as shown in Fig. 1[5]. It can be clearly seen in the figure that the half-life of ^{7}Be in the ^{7}Be@C_{60} at T=5K is 0.34% shorter than that in the ^{7}Be@C_{60} at T=293K. Furthermore, we newly found that the half-life of ^{7}Be in the ^{7}Be@C_{70} at T=293K is almost corresponding to that of the ^{7}Be@C_{60} at T=5K. Now we are continue to measure the half-life of ^{7}Be in the ^{7}Be@C_{70} at T=5K.

References

1) Segr'e E., Phys. Rev. **71** (1947) 274.
2) Ohtsuki T., et al., Phys. Rev. Lett. **93** (2004) 112501.
3) Ohtsuki T., et al., Phys. Rev. Lett. **77** (1996) 3522.
4) Ohtsuki T., et al., Phys. Rev. Lett. **81** (1998) 967.
5) Ohtsuki T., et al., Phys. Rev. Lett. **98** (2007) 252501.

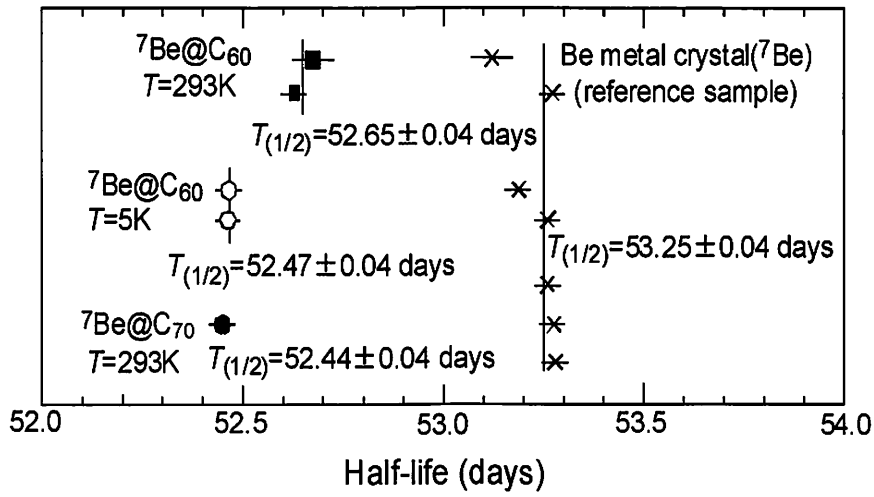

Figure 1. Half-lives are plotted: the open circles indicate the half-lives obtained for the ^{7}Be@C_{60} sample at T=5K, the closed squares for the ^{7}Be@C_{60} at T=293K, the closed circle for the ^{7}Be@C_{70} at T=293K, the cross symbols for the Be metal(^{7}Be) at T=293K.

VI. 2. Production and Chemical Separation of "No Carrier Added" Iodine-124 from a Reusable Enriched Tellurium-124 Dioxide / Aluminum Oxide Solid Solution Target

Yamazaki H.[1], Funaki Y.[1], Horiuchi Y.[1], Ishii K.[2], Kanai Y.[2], Kikuchi Y.[2], and Matsuyama S.[2]

[1]*Cyclotoron and Radioisotope Center, Tohoku University*
[2]*Graduate School of Engineering, Tohoku University*

Introduction

The development of PET from a predominantly neuroscience tool to a routine oncological investigation climaxed about 6 years ago, when PET/CT imaging become clinically available. However, this development had gathered momentum only slowly, as most of radiopharmaceuticals were labeled with short-lived nuclides and could not be distributed. Therefore experience with newly developed radiopharmaceuticals was acquired locally, and the spread of new tracers was hampered.

Iodine-124 is one of alternative long-lived PET nuclides attracting increasing interest. For example, the half-life of 4.2 days allows ^{124}I to be used in long-term PET studies of small animals. Further, ^{124}I can be used in PET scanners that are located distant from the producing cyclotron facility. Established methods in the chemistry of radioiodinations can be easily translated to ^{124}I. In general, ^{123}I and ^{131}I have been used in conjunction with a gamma camera. The former is short lived but yields reasonable scintigrams with low radiation exposure, while the latter has a longer half-life but yields poor images and entails comparatively high radiation exposure. As regards image quality and radiation exposure, ^{124}I is close to optimal. Although there are some limitations such as a low positron abundance (22-25%) and a rather complex decay scheme,[1-2] ^{124}I is still useful for medical PET imaging[3-4]. Some applications of ^{124}I in oncology have been reviewed recently[5]. The preferred production route for ^{124}I is the ^{124}Te(p,n)^{124}I process[6]. This nuclear reaction leads to good target yields with a ^{124}I product of the highest radionuclidic purity[7]. Iodine-125 ($T_{1/2}$=60 d) is the only significant impurity after the decay of ^{123}I ($T_{1/2}$=13 h). The radioactivity level of ^{125}I depends on the quality of enriched [^{124}Te]TeO_2 target

material.

This study details the essential elements for the complete production and separation by thermal processing of iodine-124 in high radionuclidic purity from the low energy, proton irradiation of an enriched tellurium-124 dioxide/aluminum oxide glassy solid solution matrix target.

Material and methods

Chemicals and solvents used were obtained from Aldrich and Wako Pure Chemicals. The enriched ^{124}Te was purchased as tellurium dioxide in 98.5% purity from Trace Sciences International. Radionuclide purity was measured using closed-end coaxial Ge-detector (EURISYS MEASURES, EGPC50-195-R) with PC-based multichannel analyzer and Aptec software. The system was calibrated using ^{152}Eu standard source (Amersham International Limited, QCR.Q8435).

Target design and irradiation conditions

The existing aluminum target holder was modified in order to accommodate a platinum disk with an outer diameter of 20 mm. The disk has a cavity of 10 mm diameter and 1.5 mm depth. The target itself consisted of an admixture of 0.280 grams of tellurium-124 dioxide and 6% by weight of aluminum dioxide. The glassy target matrix was formed at 720°C by allowing the admixture to be melted within the platinum cavity, the base of which had been roughened by random scratches in order to improve the adhesion of the target material. The physical thickness of the target was 350 mg/cm^2. The disk was covered with an aluminum foil (40 μm thickness) held down by a clamping plate. The target was manually assembled into aluminum target holder, which was compatible with the automated transfer system at the beam line.

We used 14 MeV proton beams of 10 mm spot size. It was calculated using range / energy data (SRIM-2003.26 version) that after passing the aluminum foil the incident beam was 13.7 MeV on the target and the energy decreased 4.0 MeV in the tellurium dioxide of 350 mg/cm^2 thickness. This energy range was also confirmed as being an optimum from our preliminary measurements using natural TeO_2 target of the same surface density. The target was irradiated at 1-4 μA beam current depending on the aimed production yield of ^{124}I.

Dry distillation of radioiodine-124

The distillation apparatus was similar to the one reported by Glaser *et al.*[8] with slight modification (Fig. 1). Briefly, the target holding part named as the "spoon" was stabilized and served as an inlet for the carrier O_2 gas. The male ground glass joint of the spoon had a frit attached to the main quartz tube. The other end of main tube was reduced to 0.25in tube for connecting to the trap containing 0.5 mL of 0.1 M NaOH. When attached to the furnace, the flat plate at the end of the spoon was positioned at the center of the furnace. The irradiated target was placed on the plate during the dry distillation procedure.

An irradiated target was placed in the distillation apparatus. The flow of O_2 gas was adjusted 12.5 mL/min, and the oven was turned on. Initially the temperature was set at 650°C. Once the oven set point was reached, the temperature was increased to the maximum of 710°C and the maximum temperature was kept for 30 min. The total distillation time was about 75 min. The radioiodine started releasing at around 550°C. The activity in the NaOH trap was monitored by NaI scintillation detector. Once the activity reached a flat level, after 10 min the distillation was stopped by turning off the oven. The gas flow was continued while the oven was cooling below 400°C, and then the trap was transferred to another hot cell for chemical preparation. The distillation efficiencies were 94-97% and the recovery yields of radio distilled were 82-88% (n=4) for irradiated natural TeO_2.

Quality assurance

The iodine-124 production cycle was repeated using tellurium-124 oxide target (admixture of 6 wt% Al_2O_3) of 350 mg/cm^2 density and 14 MeV proton beam of 2-4 μA. Following the recovery of the iodine-124 solution, an aliquot of the solution was assayed for gross nuclide composition. Figure 2 shows the high resolution gamma spectrum at 95 hours after end of bombardment (EOB). Due to the high isotopic enrichment of the tellurium-124 oxide used for the target preparation, the isotopic composition calculated to 95 hours after EOB was found to be ^{124}I at 98% and concurrently produced ^{123}I was 1%. Trace amount of ^{124}Sb, which may be produced by a subsequent (*n, p*) reaction of tellurium-124 by neutrons produced in the target matrix, contaminated the recovered iodine-124 solution due to the sublimation at the heating of the production cycle. As the energies of main gamma rays from ^{124}Sb are almost same as those from ^{124}I, the ^{124}Sb content in the recovered iodine-124 solution was determined by checking the decay rate of the radioactivity in the recovered solution. The radionuclide content of ^{124}Sb was calculated

to be 0.6% at 95 hours after EOB. The gamma spectrum of dry-distilled target after cooling of 635 hours showed the production of ^{126}I impurity ($T_{1/2}$=13 *d*). The radionuclide content of ^{126}I was calculated to be around 0.3% at 95 hours after EOB.

Typical batch yields for iodine-124 were estimated at 380-420 MBq at EOB based on 85% recovery for the dry distillation process. Calculated yields in this target matrix for the production of iodine-124 are in excellent agreement with the literature value of 20 MBq/μAhr on a thick target of a glassy tellurium-124 oxide target (admixture of 6 wt% Al_2O_3)[8].

References

1) Herzog H.T.L., Qaim S. M., Spellerberg S., et al., Appl. Radiat. Isot. **56** (2002) 673.
2) Qaim S.M., Hohn A., Bastian T., et al., Appl. Radiat. Isot. **58** (2003) 69.
3) Pentlow K.S., Graham M.C., Lambrecht R.M., et al., Med. Phys. **18** (1991) 357.
4) Pentlow K.S., Graham M.C., Lambrecht R.M., et al., J. Nucl. Med. **37** (1996) 1557.
5) Glaser M., Luthra S.K., Brady F., Int. J. Oncology **22** (2003) 253.
6) Scholten B., Kovacs Z., Tarkanyi F., et al., Appl. Radiat. Isot. **46** (1995) 255.
7) Bastian T., Coenen H.H., Qaim S. M., Appl. Radiat. Isot. **55** (2001) 303.
8) Glaser M., Mackay D.B., Ranicar A.S.O., Radiochim. Acta. **92** (2004) 951.

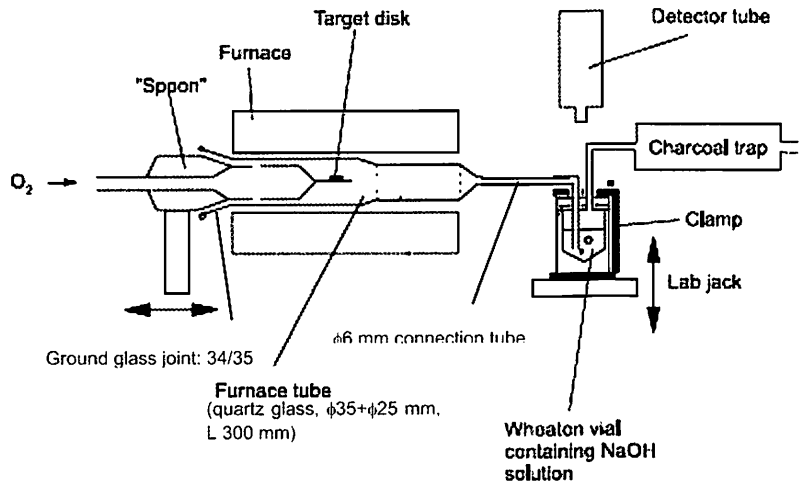

Figure 1. General scheme showing a cross-section of ^{124}I distillation apparatus.

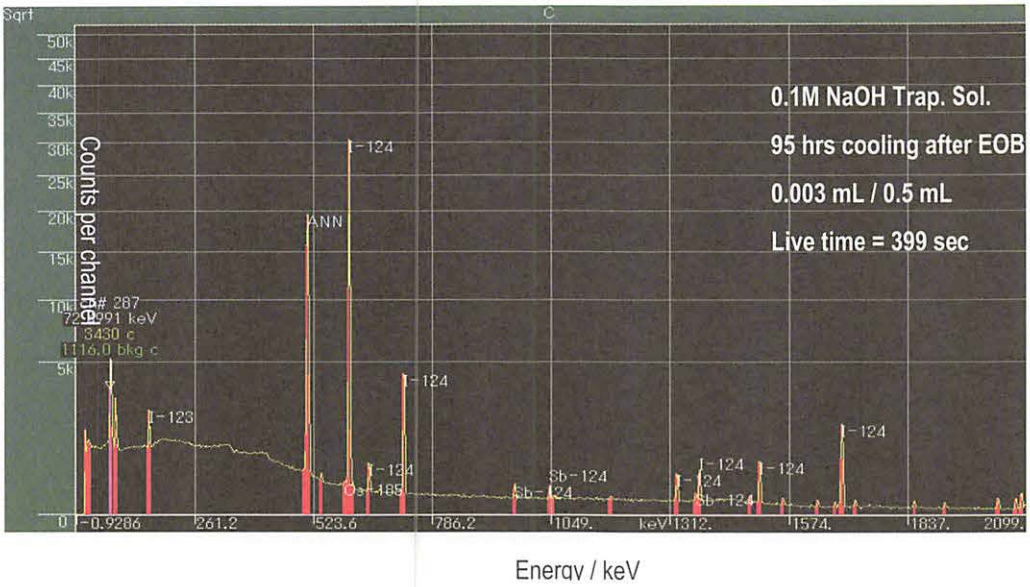

Figure 2. Gamma spectrum of the recovery of iodine-124 in a 0.1 M NaOH trap.

VII. RADIOPHARMACEUTICAL CHEMISTRY AND BIOLOGY

VII. 1. Evaluation of the Binding Characteristics of [^{18}F]Fluoroproxyfan in the Rat Brain for In Vivo Visualization of Histamine H_3 Receptor

Funaki Y.[1], Sato K.[1], Kato M.[1], Ishikawa Y.[1], Iwata R.[1], and Yanai K.[2]

[1]*Cyclotron and Radioisotope Center, Tohoku University*
[2]*Department of Pharmacology, Tohoku University Graduate School of Medicine*

Introduction

Histamine is well-known neurotransmitter that plays various important roles through four distinct G-protein-coupled receptors named simply as H_1, H_2, H_3 and H_4[1]. The histamine H_3 receptor has been firstly determined to be a presynaptic autoreceptor regulating the synthesis and release of histamine in the central nervous system (CNS) through negative feedback[2,3]. Moreover, H_3 receptors were found to act as a heteroreceptor regulating a modulatory effect on the release of other neurotransmitters in the CNS including dopamine, GABA, serotonin and acetylcholine[4]. Consequently, the H_3 receptor might be a therapeutic target in CNS disorders such as Parkinson's and Alzheimer's diseases, as well as memory, learning and sleep disorders[5,6]. From this point of view, many different leads in the development of H_3 receptor agonists or antagonists are reported to regulate synthesis and release of histamine, and to inhibit the release of various neurotransmitters[7].

It has been reported that 3-(1*H*-imidazol-4-yl)propyl 4-fluorobenzyl ether (fluoroproxyfan) has high selectivity and affinity towards H_3 receptors[8]. Although we already demonstrated that [^{18}F]fluoroproxyfan can be successfully synthesized using [^{18}F]benzyl bromide[9], its binding characteristics and use as an imaging probe have not been evaluated yet.

In the present study, we describe the biological evaluation of *in vitro* and *in vivo* of [^{18}F]fluoroproxyfan.

Methods

Fluoroproxyfan and desbenzylprecursor were synthesized according to our previous article[9]. Male Wistar rats (Japan SLC, Shizuoka, Japan; 5 weeks) were used in these studies. They were fed food and water ad libitum. The animal study was carried out according to the protocol approved by the Animal Care Committees of Cyclotron and Radioisotope Center, Tohoku University.

For *in vitro* autoradiography, Wistar rats were sacrificed and the brains were quickly removed and frozen in powdered dry ice. Serial coronal and sagittal sections, 20 μm in thickness, were cut from the frozen brains in a –20°C cryostat and dried by cold air on glass cover slips for 2-3 min and then stored at –80°C until use. Brain sections were incubated for 30 min at room temperature in the 50 mM Na/K phosphate buffer (pH 6.8) containing [^{18}F]fluoroproxyfan (1.2 MBq; Ca. 0.5 pM). Following incubation, sections were washed twice in the same buffer, and then dipped into water for 2-3 sec. Nonspecific binding was calculated in the presence of fluoroproxyfan (50 μM). Brain sections obtained were exposed to universal-type imaging plates for 10 min (Fuji Photo Film Co., Ltd.). Autoradiographic images were obtained using an imaging plate system (Fujix Bio-Imaging Analyzer BAS5000, Fuji Photo Film Co., Ltd, Tokyo).

For *in vivo* distribution study, the rats were injected intravenously with 1.30-1.85 MBq (35-50 μCi; Ca. 3.5~5 pmol) of [^{18}F]fluoroproxyfan in 0.2 mL of physiological saline via tail vein. The rats were sacrificed at the five time points (5, 15, 30, 60 and 120 min). Samples of blood and eight brain tissues (cerebral cortex, striatum, hippocampus, thalamus, hypothalamus, cerebellum, midbrain and brain stem) were quickly removed, weighed, and counted. The amount of radioactivity was expressed as differential absorption ratio (DAR). The saturation experiments were performed in order to demonstrate the reversibility of [^{18}F]fluoroproxyfan binding in vivo. A large amount of fluoroproxyfan (0.1, 0.5 and 1 mg/kg) was intraperitoneally administered with rats 15 min before [^{18}F]fluoroproxyfan injection. The rats were sacrificed 30 min after the injection.

Results

Autoradiographic demonstration of [^{18}F]fluoroproxyfan binding *in vitro* in the rat brain is shown in Fig. 1. The levels of binding sites of [^{18}F]fluoroproxyfan were higher in the striatum, thalamus and cortex and lowest in the hippocampus and cerebellum (Fig. 1 A and B). These high bindings of [^{18}F]fluoroproxyfan were easily displaced by unlabeled fluoroproxyfan (Fig. 1 C and D).

Table 1 demonstrates the time course of [^{18}F]fluoroproxyfan binding of rat *in vivo* brain. Sixty min after injection, the distribution of [^{18}F]fluoroproxyfan was heterogeneous in the rat brain; it was especially higher in the thalamus, hypothalamus and midbrain. In the blocking study, the distribution was measured 30 min after [^{18}F]fluoroproxyfan injection. Our *in vitro* binding study demonstrated [^{18}F]fluoroproxyfan binding was the lowest in the cerebellum. Therefore, the data of *in vivo* binding was calculated as the ratio of tissue to cerebellum. To confirm the reversibility of [^{18}F]fluoroproxyfan binding *in vivo*, we examined the dose effects on tissue-to-cerebellum ratios 30 min after the injection of [^{18}F]fluoroproxyfan. As shown in Fig. 2, the thalamus-to-cerebellum and hypothalamus-to-cerebellum ratios were reduced with increasing amounts of fluoroproxyfan, whereas the cortex-to-cerebellum ratio did not change with the injected dose.

Disscusion

The binding characteristics of fluoroproxyfan, an antagonist of H_3 receptor, using radioactive tracers, has not been evaluated until now, although its binding action to H_3 receptors has been studied.

First of all, we calculated exact specific activity of [^{18}F]fluoroproxyfan once, that is, after having reported an estimated value of its specific activity (>4 Ci/μmol)[9]. As a result, it became clear that specific activity of this probe is very high (11.1 Ci/μmol).

The autoradiographic study using brain slices successfully confirmed the specific binding of [^{18}F]fluoroproxyfan to H_3 receptors in the rat brain. The autoradiographic localization was almost consistent with the regional distribution of [^{18}F]fluoroproxyfan binding *in vitro*, and a large amount of unlabeled fluoroproxyfan inhibited the *in vitro* [^{18}F]fluoroproxyfan binding. It is already reported that the regional distribution patterns of H_3 receptors[3,10]. The binding of [^{18}F]fluoroproxyfan proved to be almost the same as these reports. This result suggests that it could to be useful in examining *in vitro* bindings toward H_3 receptors.

In experiments *in vivo*, the distribution of [^{18}F]fluoroproxyfan was heterogeneous in the rat brain tissues, and the values of DAR were higher than those in the blood, suggesting that [^{18}F]fluoroproxyfan easily penetrated through the blood-brain barrier. In the metabolic analysis, the detected radioactivity of brain was almost authentic as that of [^{18}F]fluoroproxyfan in the brain (data not shown). In the blocking study, all values of DAR in the brain tissues were increased in every concentration of unlabeled

fluoroproxyfan (0.1, 0.5 and 1 mg/kg). Two hypotheses for the increased uptake of DAR values can be suggested:

1) [^{18}F]Fluoroproxyfan was released from peripheral organs in order to block of possible peripheral binding site[11]. Actually, the DAR values of the lungs in the blocking experiments (5.8 ± 1.2 at 0.1 mg/kg, 2.7 ± 0.2 at 0.5 mg/kg) were more decreased than with the control experiments (89 ± 8).

2) Recently, it was reported that fluoroproxyfan is not an antagonist but rather a protean agonist[12]. Therefore, administration resulted in some biological effects such as angiectasis and up-regulation of H_3 receptors.

Accordingly, the tissue-to-the cerebellum ratio, which was the lowest distribution of [^{18}F]fluoroproxyfan *in vitro* and *in vivo*, was calculated instead of the DAR values. As a result, the *in vivo* bindings in the striatum, thalamus and hypothalamus were displaced dose-dependently by a large amount of unlabeled fluoroproxyfan. This result indicates that [^{18}F]fluoroproxyfan specifically binds to the H_3 receptors. On the other hand, the binding in the cortex was not displaced by unlabeled fluoroproxyfan, indicating the higher nonspecific binding of [^{18}F]fluoroproxyfan to the cortex. These results demonstrated that [^{18}F]fluoroproxyfan could be useful candidate to visualize *in vivo* H_3 receptors. Generally, taking suitable images were closely related with specific activity of the imaging probe. Especially, it is difficult to visualize the distribution of low-density receptors by low specific activity of radiotracers in the brain. Recently, it is reported that low-density receptors successfully visualized by the ultraspecific activity of [^{11}C]Ro15-4513[13]. Therefore, it may be suggested that the reported probes were not suitable as PET ligands for H_3 receptors because of their low specific activity[11,14].

In conclusion, we have successfully synthesized [^{18}F]fluoroproxyfan with high specific activity using [^{18}F]benzyl bromide, and binding of this probe was examined *in vitro* and *in vivo*. It has been suggested that [^{18}F]fluoroproxyfan attaches to specific binding sites of histamine H_3 receptors *in vitro*. *In vivo* brain distribution of [^{18}F]fluoroproxyfan in the rat brain was heterogeneous, and it was displaced by unlabeled fluoroproxyfan. Although further studies such as animal PET or biodistributions using H_3 receptor gene knockout mice are needed, this study clearly demonstrates that this strategy is useful to visualize histamine H_3 receptors in the living human brain in order to evaluate the efficacy of therapy of H_3 antagonists.

Acknowledgements

This study was supported by Grants-in-Aid for Young Scientists (B) (Y.F., No. 16790715) and from the Ministry of Education, Culture, Sports, Science and Technology, Japan.

References

1) Hough L.B., Mol. Pharmacol. **59** (2001) 415.
2) Arrang J.M., Garbarg M., Schwartz J.C., Nature. **302** (1983) 832.
3) Lovenberg T.W., Roland B.L., Wilson S.J., et al., Mol. Pharmacol. **55** (1999) 1101.
4) Watanabe T., Timmerman H., Yanai K., International Congress Series No. 1224 ELSEVIER SCIENCE B.V. Amsterdam The Netherlands 2001.
5) Rizk A., Curley J., Robertson J., et al., Eur. J. Neurosci. **19** (2004) 1992.
6) Passani M.B., Lin J.S., Hancock A., et al., Trends. Pharmacol. Sci. **25** (2004) 618.
7) Dvorak C.A., Apodaca R., Barbier A.J., et al., J. Med. Chem. **48** (2005) 2229.
8) Schunack W., Purand K., Hüls A., et al., XIIth Int Congress Pharmacol 1994:Abst No. P.13.14.001.
9) Iwata R., Horváth G., Pascali C., et al., J. Labelled. Cpd. Radiopharm. **43** (2000) 873.
10) Stark H., Purand K., Hüls A., et al., J. Med. Chem. **39** (1996) 1220.
11) Airaksinen A.J., Jablonowski J.A., Mey M.V.D., et al., Nucl. Med. Biol. **33** (2006) 801.
12) Gbahou F., Rouleau A., Morisset S., et al., Proc. Natl. Acad. Sci. **100** (2003) 11086.
13) Noguchi J., Suzuki K., Nucl. Med. Biol. **30** (2003) 335.
14) Ponchant M., Demphel S., Fuseau C., et al., an abstract in XIIth International Symposium on Radiopharmaceutical Chemistry, Uppsala/Sweden 1997 (June 15 - 19, 1997) 605.

Table 1. *In vivo* distribution of [^{18}F]fluoroproxyfan in the rat blood and brain.

Tissue	Time after injection				
	5 min	15 min	30 min	60 min	120 min
Blood	0.29 ± 0.03	0.39 ± 0.05	0.40 ± 0.03	0.47 ± 0.04	0.33 ± 0.01
Cortex	1.17 ± 0.11	1.00 ± 0.04	1.02 ± 0.07	0.74 ± 0.07	0.30 ± 0.02
Striatum	0.94 ± 0.11	0.94 ± 0.11	0.94 ± 0.08	0.70 ± 0.11	0.31 ± 0.02
Hippocampus	0.86 ± 0.06	0.77 ± 0.07	0.91 ± 0.05	0.69 ± 0.06	0.35 ± 0.02
Cerebellum	0.99 ± 0.05	0.87 ± 0.05	0.73 ± 0.08	0.66 ± 0.13	0.31 ± 0.01
Thalamus	1.02 ± 0.15	1.00 ± 0.14	1.23 ± 0.14	0.91 ± 0.10	0.63 ± 0.13
Hypothalamus	1.18 ± 0.12	1.08 ± 0.13	0.94 ± 0.11	1.25 ± 0.16	0.67 ± 0.06
Midbrain	1.04 ± 0.08	1.05 ± 0.05	1.01 ± 0.07	0.91 ± 0.08	0.42 ± 0.02
Brain stem	0.88 ± 0.08	1.06 ± 0.06	1.01 ± 0.08	0.82 ± 0.08	0.40 ± 0.04
Brain region / cerebellum ratio					
Cortex	1.18 ± 0.13	1.14 ± 0.08	1.40 ± 0.19	1.13 ± 0.24	0.94 ± 0.06
Striatum	0.95 ± 0.12	1.08 ± 0.14	1.29 ± 0.18	1.07 ± 0.27	0.99 ± 0.08
Hippocampus	0.87 ± 0.07	0.88 ± 0.09	1.25 ± 0.15	1.05 ± 0.22	1.13 ± 0.07
Thalamus	1.03 ± 0.16	1.14 ± 0.17	1.70 ± 0.27	1.38 ± 0.30	2.03 ± 0.42
Hypothalamus	1.19 ± 0.13	1.24 ± 0.16	1.30 ± 0.21	1.89 ± 0.43	2.14 ± 0.21
Midbrain	1.05 ± 0.10	1.20 ± 0.09	1.40 ± 0.19	1.37 ± 0.29	1.34 ± 0.08
Brain stem	0.89 ± 0.09	1.22 ± 0.10	1.39 ± 0.19	1.24 ± 0.27	1.29 ± 0.13

DAR values are expressed as means ± S.E.M (n = 4~7)

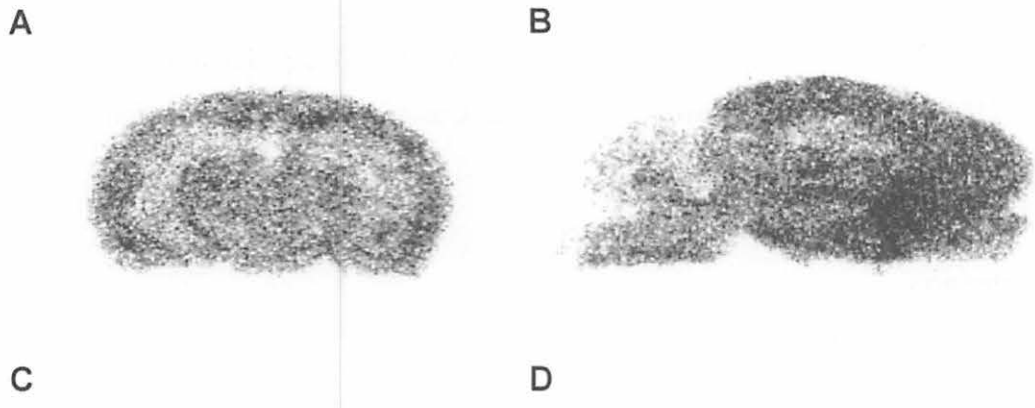

Figure 1. Autoradiographic localization of [^{18}F]fluoroproxyfan binding in the rat colonal (A and C) and sagittal (B and D) brain slices. The blocking of [^{18}F]fluoroproxyfan binding by unlabeled 50 μM fluoroproxyfan (C and D; Nonspecific binding).

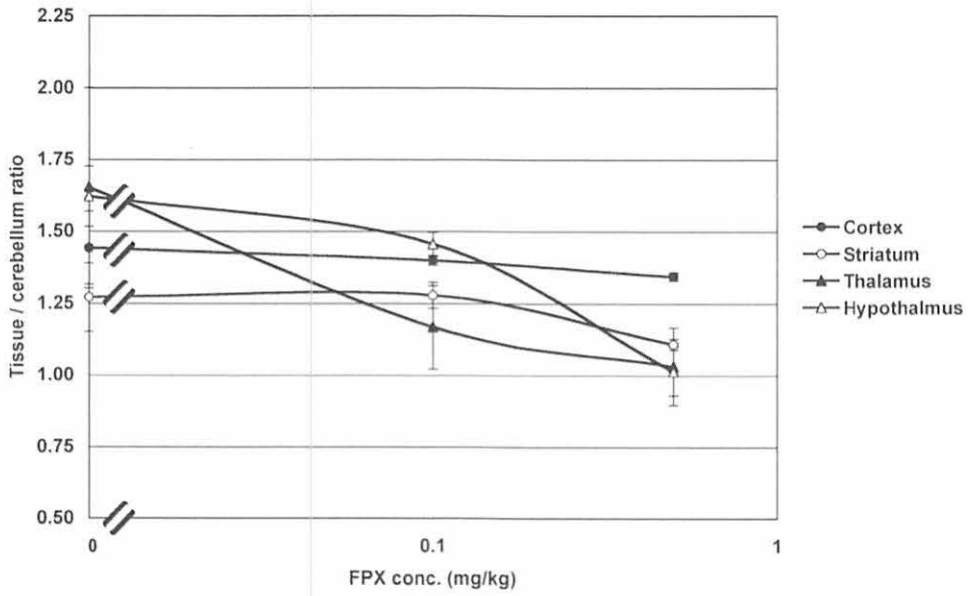

Figure 2. The true *in vivo* binding of [^{18}F]fluoroproxyfan. Dose-dependent inhibition of [^{18}F]fluoroproxyfan binding *in vivo*. Tissue-to-cerebellum ratios as a function of fluoroproxyfan dose at 30 min after [^{18}F]fluoroproxyfan injection. Data are expressed as tissue-to-cerebellum ratios (means ± S.E.M., n = 4).

VIII. NUCLEAR MEDICINE

VIII. 1. 2-(2-[2-Dimethylaminothiazol-5-yl]ethenyl)-6-(2-fluoroethoxy)-benzoxazole: A Novel PET Agent for In Vivo Detection of Dense Amyloid Plaques in Alzheimer's Disease Patients

Kudo Y.[1], Okamura N.[2], Furumoto S.[1], Tashiro M.[3], Furukawa K.[4], Maruyama M.[4], Itoh M.[3], Iwata R.[5], Yanai K.[2], and Arai H.[4]

[1]Biomedical Engineering Research Organization (TUBERO), Tohoku University
[2]Department of Pharmacology School of Medicine, Tohoku University
[3]Division of Cyclotron Nuclear Medicine, Cyclotron and Radioisotope Center, Tohoku University,
[4]Department of Geriatrics and Gerontology, Center for Asian Traditional Medicine School of Medicine, Tohoku University
[5]Division of Radiopharmaceutical Chemistry, Cyclotron and Radioisotope Center, Tohoku University,

Extensive deposition of dense amyloid fibrils is a characteristic neuropathologic hallmark in Alzheimer's disease (AD)[1-3]. Noninvasive detection of these molecules is potentially useful for early and precise detection of patients with AD. This study reports a novel compound, 2-(2-[2-dimethylaminothiazol-5-yl]ethenyl)-6-(2-fluoroethoxy) enzoxazole (BF-227, Fig. 1), for in vivo detection of dense amyloid deposits using PET.

Methods

The binding affinity of BF-227 to amyloid-β (Aβ) fibrils was calculated. The binding property of BF-227 to amyloid plaques was evaluated by neuropathologic staining of AD brain sections. Brain uptake and in vivo binding of BF-227 to Aβ deposits were also evaluated using mice. For clinical evaluation of ^{11}C-BF-227 as a PET probe, 11 normal (healthy) subjects and 10 patients with AD participated in this study. Dynamic PET images were obtained for 60 min after administration of ^{11}C-BF-227. The regional standardized uptake value (SUV) and the ratio of regional to cerebellar SUV were calculated as an index of ^{11}C-BF-227 retention. The regional tracer distribution in AD patients was statistically compared with that of aged normal subjects on a voxel-by-voxel basis[4].

Results

BF-227 displayed high binding affinity to synthetic Aβ1-42 fibrils (Ki [inhibition constant], 4.36 ± 1.5 nM). Neuropathologic staining has demonstrated preferential binding of this agent to dense amyloid deposits in AD brain (Fig. 2). Moreover, a biodistribution study of this agent revealed excellent brain uptake and specific labeling of amyloid deposits in transgenic mice. The present clinical PET study using ^{11}C-BF-227 demonstrated the retention of this tracer in cerebral cortices of AD patients but not in those of normal subjects (Fig. 3). All AD patients were clearly distinguishable from normal individuals using the temporal SUV ratio. Voxel-by-voxel analysis of PET images revealed that cortical BF-227 retention in AD patients is distributed primarily to the posterior association area of the brain and corresponded well with the preferred site for neuritic plaque depositions containing dense Aβ fibrils (Fig. 4).

Conclusion: These findings suggest that BF-227 is a promising PET probe for in vivo detection of dense amyloid deposits in AD patients.

References

1) Morris JH, Nagy Z. Alzheimer's disease. In: Esiri MM, Lee VM, Trojanowski JQ, eds. The Neuropathology of Dementia. 2nd ed. Cambridge, U.K.: Cambridge University Press; **4** (200) 161.
2) Goldman WP, Price JL, Storandt M, et al., Neurology **56** (2001) 361.
3) Price JL, Morris JC., Ann Neurol. **45** (1999) 358.
4) Friston KJ, Holmes AP, Worsley KJ, Poline JP, Frith CD, Frackowiack RSJ., Hum Brain Mapp. **2** (1995):189.

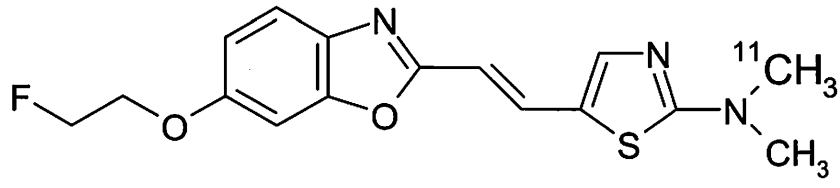

Figure 1. Chemical Structure of ^{11}C-BF-227.

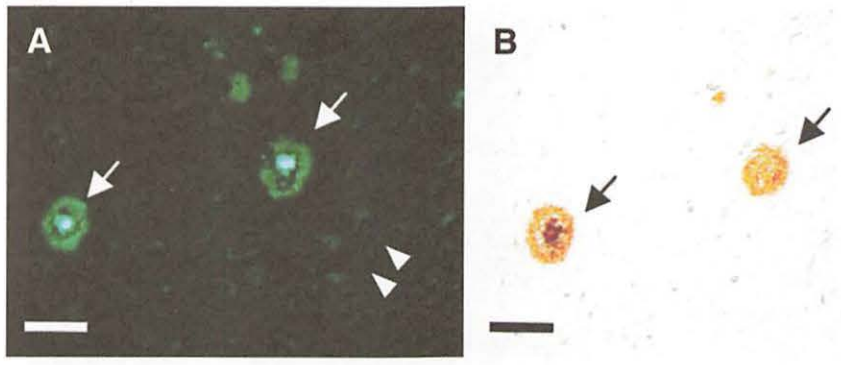

Figure 2. Neuropathologic staining of human brain sections by BF-227. Amyloid plaques are clearly stained with BF-227 in AD temporal brain sections (A). BF-227 staining correlates well with Aβ immunostaining in adjacent sections (B, arrows). Bar = 50 μm

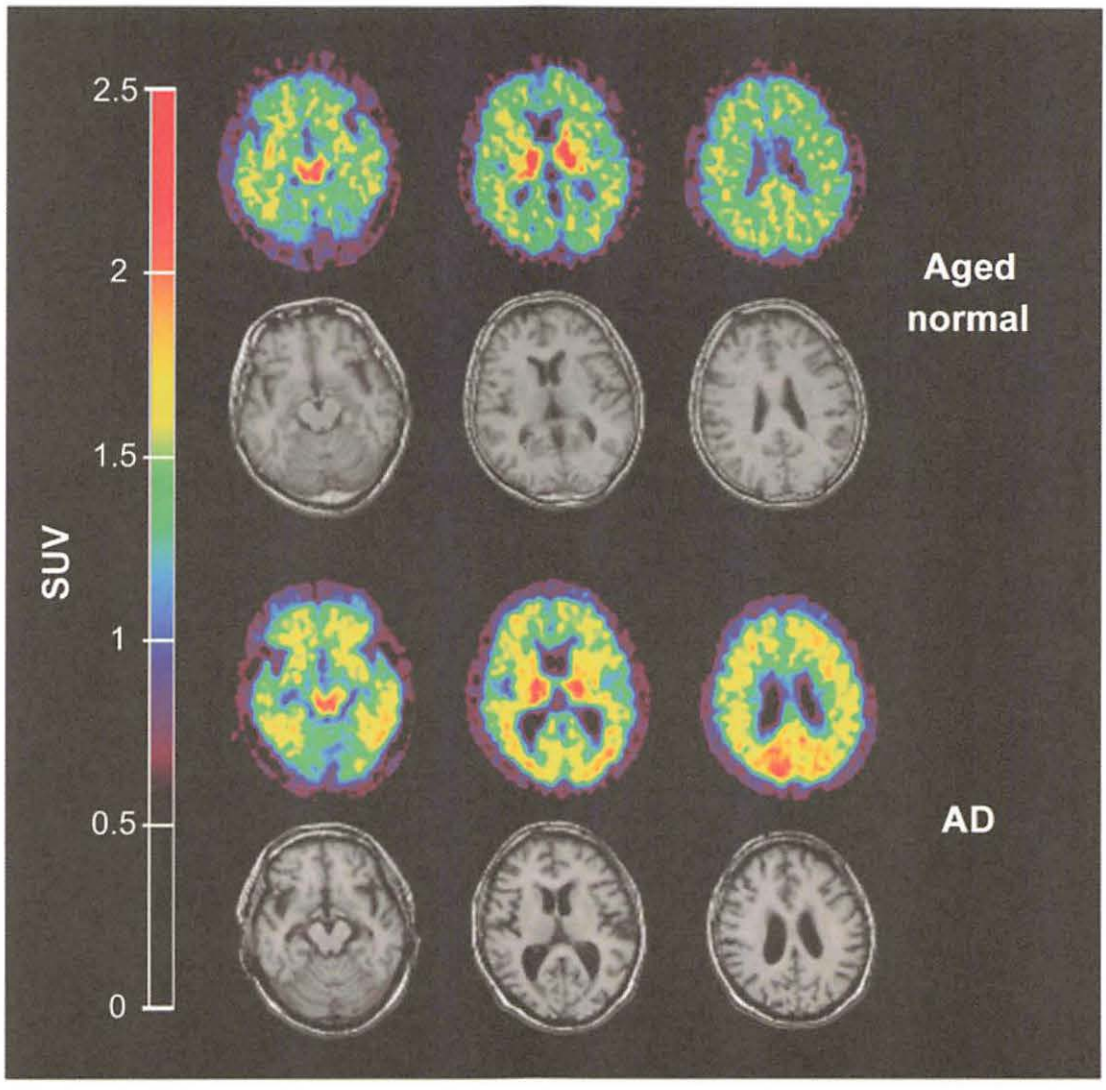

Figure 3. Mean SUV images between 20 and 40 min after injection of ^{11}C-BF-227 in aged normal subject (top, 70-y-old woman) and AD patient (bottom, 68-y-old woman). Coregistered MR images are shown below PET images.

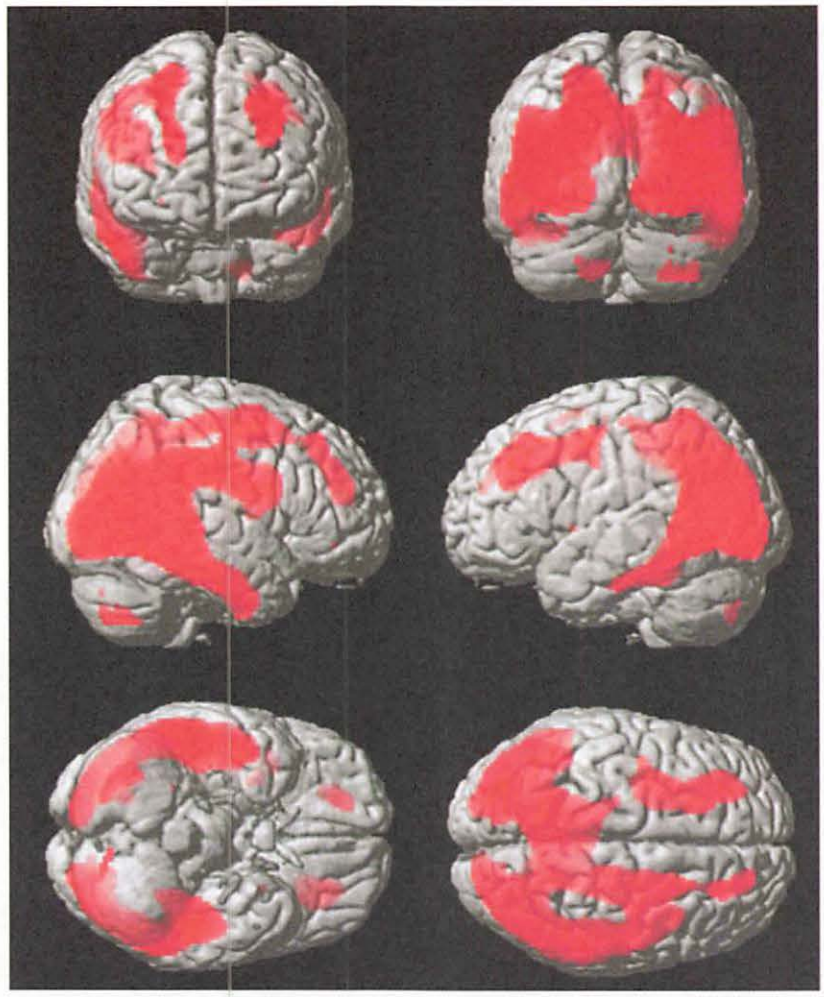

Figure 4. Brain regions show significantly elevated SUVs in AD patients compared with data from aged healthy subjects ($P < 0.001$, uncorrected for multiple comparisons).

VIII. 2. In Vivo Imaging of Donepezil Binding in the Brain Using [^{11}C]Donepezil-PET

Okamura N.[1], Funaki Y.[2], Tashiro M.[2], Kato M.[1], Ishikawa Y.[2], Ishikawa H.[3], Meguro K.[3], Iwata R.[2], Itoh M.[2], and Yanai K.[1]

[1]*Department of Pharmacology, Tohoku University School of Medicine*
[2]*Cyclotron and Radioisotope Center, Tohoku University*
[3]*Department of Geriatric Behavioral Neurology, Tohoku University School of Medicine*

Currently, cholinergic enhancement is a major approach to the treatment of cognitive and behavioral disturbances in dementia. AChE inhibitors (AChEIs) are widely prescribed to improve cognitive function in patients with Alzheimer's disease (AD)[1]. Thus, functional imaging of cholinergic function is a useful strategy for determination of the treatment protocol of demented patients. Donepezil hydrochloride is currently the AChEI most widely used for the treatment of AD. It exhibits selective binding of AChE compared with butyrylcholinesterase (BuChE)[2]. Radiolabeled donepezil can be used as a tracer to measure brain concentrations of AChE. If the distribution of donepezil in the brain can be quantitatively measured by PET, this will be useful for pharmacological evaluation of AChEIs and for prediction of efficacy of treatment with donepezil. In this study, we performed PET examinations using [5-^{11}C-methoxy]donepezil ([^{11}C]donepezil) and determined the in vivo binding characteristics of donepezil in AD patients.

Three young normal and 6 aged normal subjects and 10 patients with probable AD were studied to examine the distribution of [^{11}C]donepezil in the brain. The AD patients were recruited through The Tohoku University Hospital Dementia Patients Registry. The diagnosis of AD was made according to the National Institute of Neurologic Disorders and Stroke/Alzheimer's Disease and Related Disorders Association (NINCDS-ADRDA) criteria. After complete description of the study to the patients and subjects, written informed consent was obtained from them. PET study was performed within 3 months after the completion of medical and neuropsychological examination. Synthesis of [^{11}C]donepezil was performed as described previously[3]. The [^{11}C]donepezil PET study was performed using a SET-2400W PET scanner (Shimadzu Inc., Japan) under resting condition with eyes closed. Following a

68Ge/Ga transmission scan of 7 min duration, an emission scan was started soon after intravenous injection of 7.1 - 9.5 mCi of [^{11}C]donepezil. Dynamic emission tomography data were acquired for 60 min. Arterialized venous blood samples were also obtained from a hand vein, heated in a far-infrared mat, and radioactivity was measured in a well-type scintillation counter. Region of interest (ROI) analysis was performed to evaluate the regional distribution of [^{11}C]donepezil. Circular ROIs (1.0 cm in diameter) were placed on individual axial PET images, referring to the individual MR images. The distribution volume (DV) of [^{11}C]donepezil was calculated by Logan's graphical analysis[4], since donepezil reversibly binds AChE. Using this method, the DV in each ROI was determined from the slopes obtained from the values of each ROI and input function from metabolite-corrected plasma radioactivity. The slopes were determined from the last 15 points of the respective regions.

As a result, parametric images of [^{11}C]donepezil DV clearly revealed higher concentrations of tracer distribution in the striatum and cerebellum than in neocortex (Fig. 1). Patients with AD exhibited significant reduction of DV in all brain regions, compared with aged normal subjects (Fig. 1, Table 1). The magnitude of DV reduction in AD group was about 25% in the hippocampus and 20% in temporal and parietal cortices. In addition, [^{11}C]donepezil DV in the striatum, cerebellum, thalamus, parietal and anterior cingulate cortices was significantly correlated with regional AChE activity determined in a human postmortem study[5] (Fig. 2), suggesting selective binding of donepezil to AChE.

Current PET study demonstrated that intravenously administered [^{11}C]donepezil is mainly distributed in the striatum, thalamus, and cerebellum, which are known to contain high densities of AChE compared to cerebral cortex and hippocampus. This finding is consistent with the findings of our previous study in rats[3]. AD patients exhibited significant reduction of [^{11}C]donepezil DV in all brain regions examined. These reductions suggest early involvement of the cholinergic system in AD, since the AChE in brain is predominantly located in presynaptic cholinergic neurons[6]. A previous study demonstrated 21% reduction of hippocampal AChE activity in patients with early-onset AD[7]. We observed an approximately 20 - 25% reduction in the neocortex and hippocampus of AD patients. These findings suggest that the concentration of donepezil-binding AChE is matched by regional AChE activity. The amount of orally administered donepezil binding to AChE is considered to be a key factor determining therapeutic response. AChE binding occupancy by orally administered donepezil could be modulated by the blood-brain barrier permeability, tissue distribution, metabolism and also by AChE density in the patient's brain. Therefore, in vivo evaluation of AChE occupancy

could be a powerful strategy to determine the optimal dose of donepezil. In future, quantitative evaluation of donepezil binding site might be used to optimize the treatment regimen by donepezil and to predict the therapeutic response of donepezil.

In this study, the distribution of donepezil in human brain was successfully visualized using [^{11}C]donepezil and PET. Graphical analysis by Logan plots can be used to obtain quantitative estimates of specific donepezil binding. AD patients exhibited significant reduction of donepezil distribution, even in the early stage of disease. This imaging technique will be useful as a new surrogate marker for evaluation of treatment with donepezil.

References

1) Giacobini E., Taylor & Francis Group (2000) 181.
2) Sugimoto H., Ogura H., Arai Y., Iimura Y., Yamanishi Y., Jpn. J. Pharmacol. **89** (2002) 7.
3) Funaki Y., Kato M., Iwata R., Sakurai E., Sakurai E., Tashiro M., Ido T., Yanai K., J. Pharmacol. Sci. **91** (2003) 105.
4) Logan J.,. Nucl. Med. Biol. **27** (2000) 661.
5) Finkelstein Y., Wolff M., Biegon A., Ann. Neurol. **24** (1988) 252.
6) Mesulam M.M., Geula C., Brain Res. **577** (1992) 112.
7) Shinotoh H., Namba H., Fukushi K., Nagatsuka S., Tanaka N., Aotsuka A., Ota T., Tanaka S., Irie T., Ann. Neurol. **48** (2000) 194.

Table 1. Regional distribution volume of [^{11}C]donepezil in young and aged normal subjects and AD patients.

	Young normal	Aged normal	AD
Cerebellum	25.8 ±2.6	22.8 ±1.3	18.2 ±1.7 #*
Striatum	22.6 ±2.5	23.6 ±1.7	18.9 ±2.3 *
Thalamus	22.5 ±2.5	23.0 ±1.6	17.6 ±1.8 *
Frontal	19.8 ±2.2	18.2 ±1.0	14.6 ±1.7 #*
Temporal	20.5 ±2.2	19.2 ±1.0	15.3 ±1.2 #*
Parietal	20.5 ±2.4	18.9 ±1.0	15.2 ±1.5 #*
Occipital	21.1 ±2.4	19.0 ±1.2	15.1 ±1.9 #*
Anterior cingulate	20.6 ±2.4	19.3 ±1.2	14.9 ±1.8 #*
Posterior cingulate	22.1 ±2.5	20.6 ±1.2	16.4 ±1.9 #*
Hippocampus	22.4 ±1.6	20.6 ±0.9	15.3 ±1.6 #*

# $P<0.05$, significantly different from young normal group.
* $P<0.05$, significantly different from aged normal group.

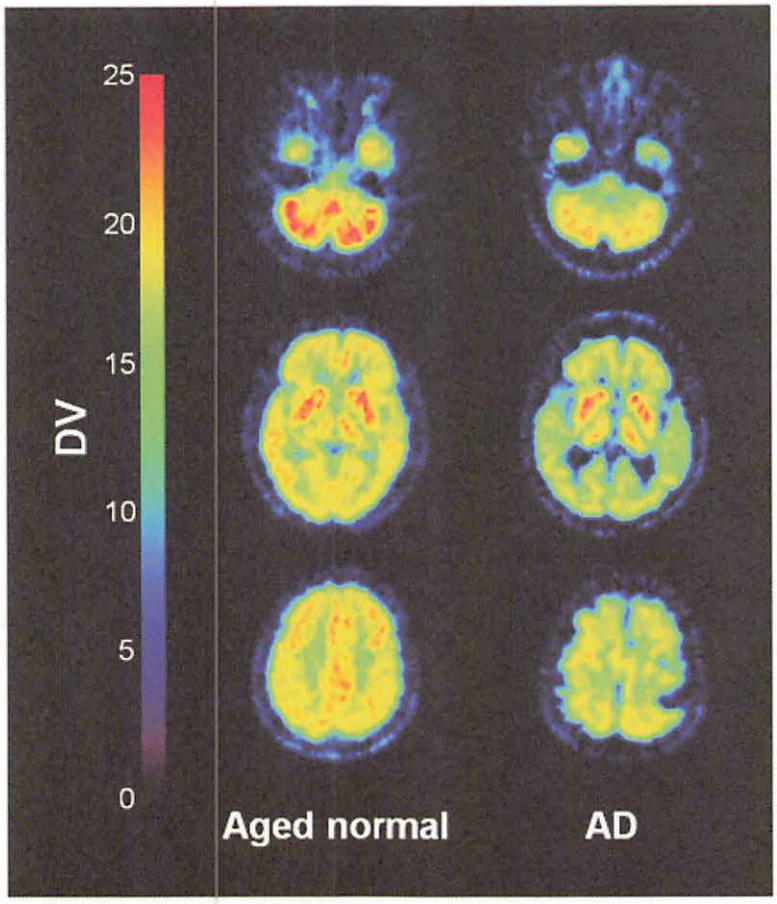

Figure 1. Distribution volume (DV) images of [^{11}C]donepezil in aged normal subject and AD patient.

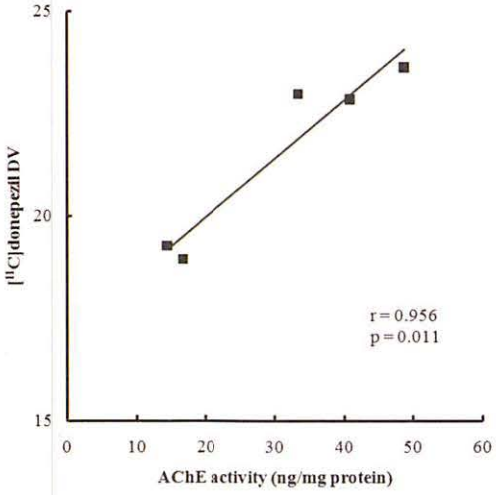

Figure 2. Correlation between distribution volume of [^{11}C]donepezil and AChE activity in the postmortem brain. Postmortem data was cited from ref. 5.

VIII. 3. Dynamic Human Imaging using ^{18}F-FRP170 as a New PET Tracer for Imaging Hypoxia

Kaneta T.[1], Takai Y.[2], Iwata R.[3], Hakamatsuka T.[1], Yasuda H.[3], Nakayama K.[4], Ishikawa Y.[3], Watanuki S.[3], Furumoto S.[3], Funaki Y.[3], Nakata E.[2], Jingu K.[5], Tsujitani M.[6], Ito M.[3], Fukuda H.[7], Takahashi S.[1], and Yamada S.[5]

[1]*Department of Diagnostic Radiology, Tohoku University*
[2]*School of Health Sciences, Faculty of Medicine, Tohoku University*
[3]*Cyclotron and Radioisotope Center, Tohoku University*
[4]*Department of Geriatric and Respiratory Medicine, Tohoku University*
[5]*Department of Radiation Oncology, Tohoku University*
[6]*POLA Chemical Industries, Yokohama, Japan*
[7]*Institute of Development, Aging and Cancer, Tohoku University*

The 2-nitroimidazole analogs are known to have an interesting property, namely, they accumulate selectively in hypoxic tissue. The mechanism for the intracellular retention in hypoxic cells is not fully understood. It is believed that 2-nitroimidazoles undergo nitro-reduction with the formation of products that bind to intracellular elements and remain trapped in hypoxic tissues[1]. ^{18}F-Fluoromisonidazole (^{18}F-FMISO) was the first such radiopharmaceutical developed, and was used most widely for imaging hypoxia. However, misonidazole is a rather lipophilic compound, and the images of ^{18}F-FMISO may have a low target-to-background ratio. Therefore, there is ongoing research to develop better compounds for clinical use. ^{18}F-FRP170, 1-(2-fluoro-1-[hydroxymethyl]ethoxy)- methyl-2-nitroimidazole, is a new hypoxia imaging agent for positron emission tomography (Fig. 1). This compound was synthesized by ^{18}F-labeling of RP170, which was developed as a new hydrophilic 2-nitroimidazole analog[2,3]. In the present study, we analyzed dynamic whole-body imaging in healthy volunteers and dynamic tumor imaging in three patients with lung cancer.

Methods

Four healthy male volunteers and three lung cancer patients were enrolled in this study. Volunteers underwent dynamic whole-body scans just after injection of ^{18}F-FRP170 for about 90 min, while the lung cancer patients underwent dynamic tumor imaging for about 60 or 120 min. Data are expressed as standardized uptake values (SUV). Regions of interest were placed

over images of each organ or tumor to generate time–SUV curves.

Results

The series of dynamic whole-body scans showed rapid elimination of ^{18}F-FRP170 from the kidneys following elimination from the liver. Figure 2 shows a series of dynamic whole-body images of a 32-year-old male volunteer. Very low physiological uptake was observed above the diaphragm. ^{18}F-FRP170 uptake in the lung cancer lesion could be visualized clearly from early after injection. The changes of tumor SUV, tumor/blood ratio, or tumor/muscle ratio about 30 min. after injection or later were small. Figure 3 shows ^{18}F-FRP170 images acquired 1 hr and 2 hr after injection in patient with lt. lung cancer. The tumor/muscle ratio and tumor/blood ratio were 1.69 and 1.09 at 1 h after injection, and 1.96 and 1.24 at 2 h, respectively.

Discussion

Since the 1990s, there have been many intensive studies using ^{18}F-FMISO, and a great deal of research effort has been directed toward synthesizing new hypoxia markers that overcome the limitations of ^{18}F-FMISO. Compounds characterized by high hydrophilicity were thought to be better for imaging hypoxia because of rapid blood clearance and high target-to-background ratio. Therefore, many 2-nitroimidazole analogs have been developed by changing the side chain of the drug. ^{18}F-FRP170 is designed as a hydrophilic 2-nitroimidazole analog, and is also expected to yield images with high contrast and a low background level. In the volunteer study, ^{18}F-FRP170 showed rapid elimination from almost all organs *via* excretion through the urinary pathway. In addition, its excretion into the bile was delayed. These observations were thought to be due to the high degree of hydrophilicity of the tracer. ^{18}F-FRP170 uptake in the lung cancer could be visualized clearly from early after injection. The tumor/muscle ratio tended to decrease slightly prior to 45-60 min after injection, but then tended to increase slightly. On the other hand, the tumor/blood ratio showed a rapid increase prior to about 30 min after injection, after which it increased gradually with time. The tumor/muscle ratio and tumor/blood ratio in Fig 3 were 1.69 and 1.09 at 1 h after injection, and 1.96 and 1.24 at 2 h, respectively. Both the tumor/muscle and tumor/blood ratios were higher 2 h than 1 h after injection, although the differences were too small to detect visually. The images obtained about 60 min after injection may be of sufficient quality to allow evaluation of tumor uptake in a clinical setting. However, considering the recent advances of

PET technology, the images of ^{18}F-FRP170 demonstrated in the present study may have room for improvement. For example, increasing injected doses, longer emission-scan time, or using the latest PET/CT scanner may improve the image quality. The 2-nitroimidazoles are known to enter the cells by passive diffusion; therefore, their intracellular uptake is thought not to be particularly high. It may be necessary to administer a larger amount of radioactivity than that used in the present study. From the standpoint of estimated radiation dose[4], about 370–555 MBq of ^{18}F-FRP170 may be considered safe for use in adults.

Conclusions: We analyzed dynamic ^{18}F-FRP170 images obtained in healthy volunteers and in three patients with lung cancer. Rapid elimination of the tracer from the kidney was seen in the volunteers, supporting the strong hydrophilicity of ^{18}F-FRP170. The images obtained in the cases of the lung cancer patients demonstrated good image contrast even at 1 h after injection. ^{18}F-FRP170 could be expected to yield good tumor images and allow scanning to begin early, but further investigations are warranted to clarify these points.

References

1) Nunn A., Linder K., Strauss H.W., Eur. J. Nucl. Med. **22** (1995) 265.
2) Wada H., Iwata R., Ido T., Takai Y., J. Label. Compd. Radiopharm. **43** (2000) 785.
3) Kaneta T., Takai Y., Kagaya Y., Yamane Y., Wada H., Yuki M., et al., J. Nucl. Med. **43** (2002) 109.
4) Ishikawa Y., Funaki Y., Iwata R., Furumoto S., Nakata E., Kudo Y., et al., Kaku Igaku **42** (2005) 1.

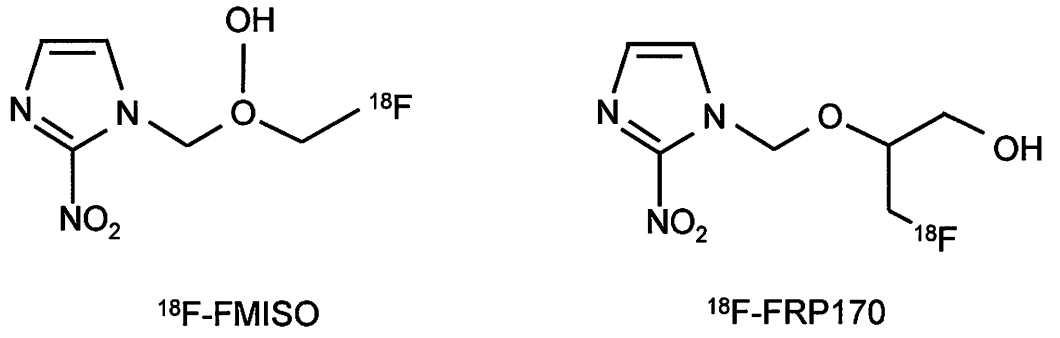

Figure 1. Chemical structures of ^{18}F-FMISO and ^{18}F-FRP170.

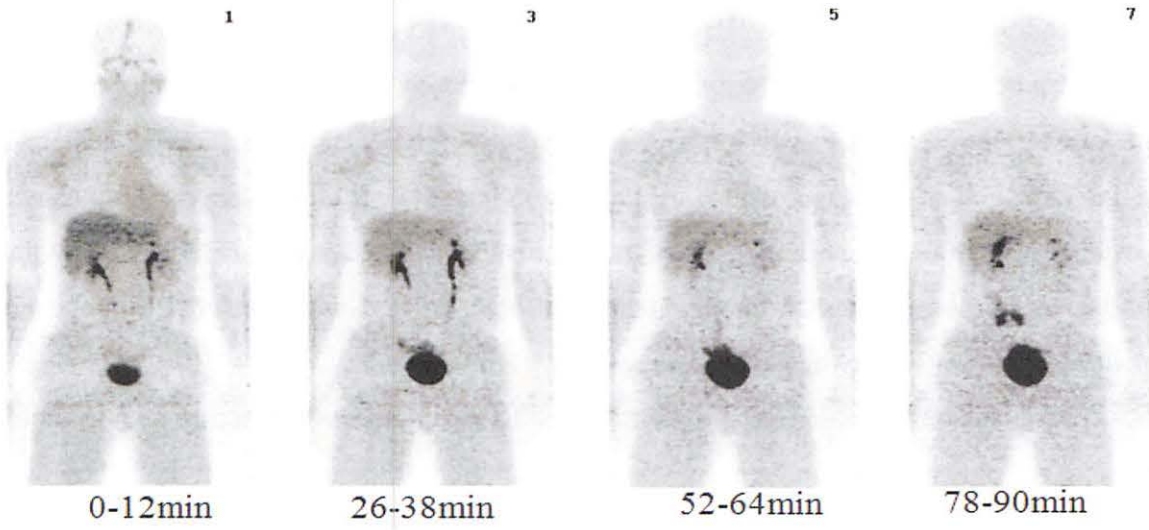

Figure 2. A series of dynamic whole-body images of a 32-year-old male volunteer.

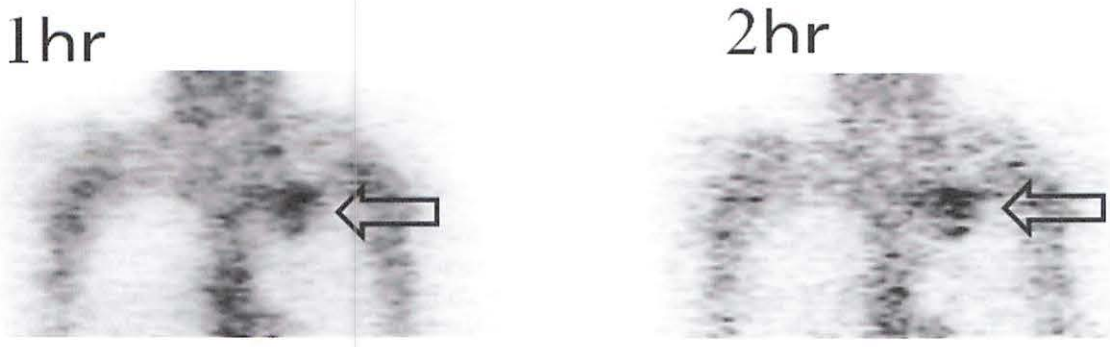

Figure 3. ^{18}F-FRP170 images of lung cancer (*arrow*) acquired 1 hr and 2hr after injection.

VIII. 4. Evaluate of P-Glycoprotein Activity as an Efflux Pump in the Blood-brain Barrier of Living Human Brain

Tashiro M.[1], Tsujimoto M.[3], Kato M.[2], Watanuki S.[1], Ohtani H.[4], Itoh M.[1], Sawada Y.[4], and Yanai K.[1,2]

[1]Division of Cyclotron Nuclear Medicine, Cyclotron and Radioisotope Center, Tohoku University
[2]Department of Pharmacology, Graduate School of Medicine, Tohoku University
[3]Department of Hospital Pharmacy, Kyoto Pharmaceutical University,
[4]Laboratory of Drug Informatics, Graduate School of Pharmaceutical Sciences, the University of Tokyo,

Introduction

The Human Genome Project (HGP), a 13-year international project, completed in 2003. They identified approximately 20,000-25,000 genes in human DNA and determined the sequences of the 3 billion chemical base pairs of the human DNA. Since then, many people have expected the establishment of a system for "individualized or personalized medicine". However, it is still a long way. There are huge number of transporters and enzymes contributing to every process of drug absorption, distribution, metabolism and excretion.

In the human body, for instance, there are many drug transporters such as p-glycoprotein (P-gp), multi-drug resistance protein (MRP); organic anion transporting polypeptide (OATP), in various organs of the human body. It is not easy to determine the functional effects of various genetic mutations. The field of "pharmaco-genomics" or "pharmaco-genetics" have explored the relationship between single nucleotide polymorphisms (SNPs) and pharmaco-kinetic/ -dynamic outcomes. The merit of using molecular imaging technique in this field is that we can obtain biological information regarding changes in an intermediate "endo-phenotype", lying between changes in genotype and phenotype.

As an example, P-gp, a gene product of MDR1 (Multi-drug resistance gene 1) in human, is one of the most important transporters contributing to drug transport in human body. It is working like a cellular pump equipped by a battery, transporting various xenobiotics (biologically-active substances from outside) being energized by ATP binding cassettes (ABC).

The P-gp was first discovered as the cause substance of multidrug-resistant cancer cells that altered membrane permeability of the anticancer drugs. Then, it was later identified in various normal tissues as well. Currently, it is known that the P-gp is expressed in cells of various organs such as the intestinal tract, liver, kidney, placenta, and brain [blood-brain barrier: BBB]). Most of these organs have secreting function where the cells are transporting the xenobiotics actively from the inside of endothelial cells of capillaries to the capillary lumen (Figure 1).

So far, the effect of MDR-1 polymorphism on the BBB permeability has been studied in human using PET and [^{11}C]verapamil between single nucleotide polymorphisms such as C1236T and C3435T. They demonstrated that there was no difference in the BBB permeability[1,2] where they did not find any difference among different polymorphisms. However, there have been no studies to evaluate the difference using drugs in clinical doses.

We have measured variation of histamine H1 receptor (H1R) occupancy following oral administration of various antihistamines. The variation in the cerebral H1R occupancies due to antihistamines may be in part a result of their different BBB permeabilities, as having been demonstrated as H1R occupancy using PET and [^{11}C]doxepin[2-5]. In clinical settings, however, permeability at the gut level would also affect the net antihistamine transport in to the brain.

Thus, the purpose of the present study is to examine whether the histamine H1R occupancy due to fexofenadine, a non-sedative antihistamine, varies between different genetic types or not, using a non-invasive technique such as PET. For this purpose, the authors tried to compare the amount of antihistamines transported into the brain tissue during 3 hours following medication. Fexofenadine is also a substrate of P-gp, and it is thought that BBB permeability is low even at an exceeded dose[5].

Methods

Thirty-nine healthy volunteers (24.2 +/- 4.0 years old) were studied. Informed consent was collected from each volunteer following adequate explanation, based on the permission from the ethics committee of Tohoku University Graduate School of Medicine. Blood sample was obtained from each volunteer and the polymorphism typing of MDR-1 gene was determined using polymerase chain reaction-restriction fragment length polymorphism (PCR-RFLP) method (C3435T mutation in exon 26 and C1236T mutation in exon 12). Out of the 39 subjects, 24 volunteered consented for further PET examination.

The PET examination was conducted in the 24 subjects, using fexofenadine hydrochloride (FEX) 120 mg or lactobacteria preparation 6 mg as placebo (PLA) with the

minimum washout period of 7 days. The volunteers were scanned 90 min after administration of oral tablets using an ECAT PT931 PET scanner (CTI Inc, Knoxville, TN, USA), taking 90 min for each scan (22 sequential scans: six scans for 90 seconds, seven scans for 180 seconds, six scans for 300 seconds and three scans for 600 seconds). The order of drug conditions was controlled and balanced. The basic protocol is demonstrated in the Figure 3.

After being corrected for tissue attenuation, brain images were processed by applying a Logan graphical analysis using cerebellar time activity curve as input functions to obtain binding potential (BP) images. Finally, brain BP images were created from which H1RO was calculated for the prefrontal, anterior cingulate, orbitofrontal and temporal cortices. The H1ROs following fexofenadine treatment was calculated based on the following equation: H1RO = $[(\text{mean } BP_{PLA} - \text{mean } BP_{FEX})/\text{mean } BP_{PLA}] \times 100$.

Results

Results of polymorphism analysis demonstrated that the numbers of holders of wild-type genetic pattern (CC), heterozygous mutation pattern (CT) and homozygous mutation pattern (TT), respectively were 10 (25.6%), 24 (61.5%), and 5 (12.8%) for 3435 mutation. The results for 1236 mutation were 4 (10.3%), 16 (41.0%), and 19 (48.7%), respectively. The present results were equal to previous studies for Japanese population.

Result of PET investigation is demonstrated in the Fig. 4, showing almost negligible differences between FEX and placebo conditions in some subjects. Further analysis regarding H1R occupancy following FEX treatment calculated based on the placebo data were demonstrated in the anterior cingulated gyrus, frontal cortex, occipital cortex, orbitofrontal cortex, and temporal cortex as -5.41%, -3.6%, -0.05%, -8.20%, -1.12%, respectively. In addition, an overall cortical mean value was -3.67%.

Comparison of H1R occupancy values averaged across the cortex among subgroups divided by polymorphism types (C3435T mutation) revealed the trend toward increased H1R occupancy in volunteers having mutated genes though there was no statistical significance among the subgroups (Fig. 2).

Discussions

This is a preliminary research regarding the variation in receptor occupancy of a psychoactive drug such as an antihistamine associated with genetic polymorphisms in human MDR1 gene.

First, H1R occupancy of fexofenadine in the present study was negative values in many brain regions. The values calculated in our previous study[5] were also negative values in some brain regions such as the anterior cingulate, where the baseline data was used from different subjects. In the present study, however, the H1R occupancy was calculated using the baseline (placebo condition) data obtained from the same subjects. Then it is hard to explain the negative values by the inter-individual difference.

Secondarily, the present PET study demonstrated that relatively higher H1R occupancy in the holders of mutant genes though these results were not statistically significant. The effect of MDR polymorphisms on the BBB permeability of fexofenadine has never been studied using PET. The PET results might suggest the presence of slight decrease in efflux function of P-glycoprotein in BBB among holders of mutations in comparison to wild-type gene holders. But it is not known if there is any BBB permeability variation among other drugs.

To draw a definitive conclusion, further investigation is needed to draw a conclusion with larger sample size. The molecular imaging technique seems to be very useful for establishment of the field of individualized medicine or personalized medicine. Importantly, the molecular imaging technique enables us to access the biological information of endophenotype. Observation of the endophenotype makes possible the prediction and explanation of the possible mechanism of drug side effects.

References

1) Ikoma Y., Takano A., Ito H., Kusuhara H., Sugiyama Y., Arakawa R., Fukumura T., Nakao R., Suzuki K., Suhara T., J. Nucl. Med. **47** (2006) 1531.
2) Takano A., Kusuhara H., Suhara T., Ieiri I., Morimoto T., Lee Y.J., Maeda J., Ikoma Y., Ito H., Suzuki K., Sugiyama Y., J. Nucl. Med. **47**(2006) 1427.
3) Yanai K., et al., Br. J. Pharmacol. **116** (1995) 1649.
4) Tagawa M., et al., Br. J. Clin. Pharmacol. **52** (2001) 501.
5) Tashiro M., Sakurada Y., Iwabuchi K., Mochizuki H., Kato M., Aoki M., Funaki Y., Itoh M., Iwata R., Wong D.F., Yanai K., J. Clin. Pharmacol. **44** (2004) 890.
6) Tashiro M., Mochizuki H., Sakurada Y., Ishii K., Oda K., Kimura Y., Sasaki T., Ishiwata K., Yanai K.,. Br. J. Clin. Pharmacol. **61** (2006) 16.

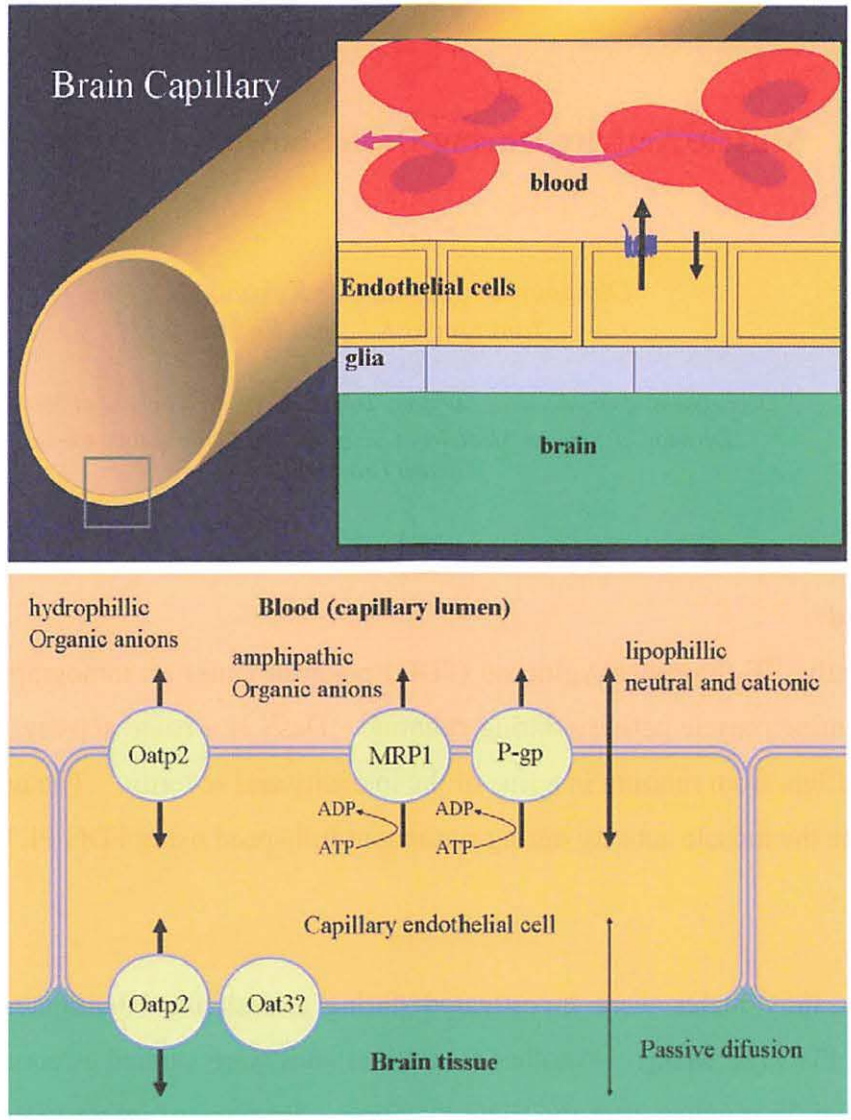

Figure 1. Basic structure of Blood-brain barrier (BBB) consisting of the capillary endothelial cells and glias. An efflux transporter (blue) is actively transporting specific substrates outward into the blood stream (TOP). Various transporters are located at the BBB. P-gp is transporting specific substrates outward using the energy supplied by ATP. Lipophillic drugs can enter the brain tissue easily. Hydorphillic drugs have difficulty to enter the brain tissue (BOTTOM).

VIII. 5. Muscle Activity During Dash Shown by ^{18}F-FDG PET Imaging

Ohnuma M.[1], Sugita T.[1], Kokubun S.[1], Itoh T.[1], Yamaguchi K.[1], and Rikimaru H.[2]

[1]Department of Orthopaedic Surgery, Tohoku University School of Medicine
[2]Division of Nuclear Medicine, Cyclotron and Radioisotope Center, Tohoku University

Background

Recently, ^{18}F-fluorodeoxyglucose (FDG) positron emission tomography (PET) has been used to examine muscle activity during running. Dash is a basic activity in various kinds of sports but differs from running in terms of the intensity and severity. The purpose of this study is to evaluate the muscle activity during running at full speed using FDG PET.

Methods

Six healthy males were investigated during a dash for 10 minutes after intravenous injection of FDG (37 MBq). Another 6 healthy males were studied as controls. PET images were obtained 45 minutes after the FDG injection. Regions of interest (ROI) were drawn on the anterior and posterior thighs, and the anterior and posterior legs. The standardized uptake value (SUV) was calculated to examine the FDG uptake of muscle tissue per unit volume according to the equation.

Results: In the control group, the mean standardized uptake values (SUVs) of the anterior thigh, the posterior thigh, the anterior leg, and the posterior leg were 0.49 ± 0.04, 0.44 ± 0.02, 0.46 ± 0.05, and 0.44 ± 0.07, respectively. In the dash group, the mean SUVs of the anterior thigh, the posterior thigh, the anterior leg, and the posterior leg were 0.74 ± 0.20, 0.79 ± 0.08, 0.61 ± 0.07, and 0.60 ± 0.08, respectively. FDG accumulation of the every four compartment in the dash group was significantly higher than that in the control. FDG accumulation of the posterior thigh was significantly higher than that of the anterior and the posterior leg in the dash group ($p<0.02$).

Conclusion: It was observed from our investigation that the posterior thigh muscles were

especially activated during a dash.

References

1) Mero A., Komi P.V., Eur. J. Appl. Physiol. **55** (1986) 553.
2) Mero A., Komi P.V., Med. Sci. Sports Exerc. **19** (1987) 266.
3) Montgomery W.H.III., Pink M., Perry J., Am. J. Sports Med. **22** (1994) 272.
4) Drace J.E., Pelc N.J., Radiology **193** (1994) 423.
5) Fisher M.J., Meyer R.A., Adams G..R., Foley J.M., Potchen E.J., Invest.Radiol. **25** (1990) 480.
6) Weidman E.R., Charles H.C., Negro-Vilar R., Sullivan M.J., MacFall J.R., Invest. Radiol. **26** (1991) 309.
7) Fujimoto T., Itoh M., Kumano H., Tashiro M., Ido T., Lancet **348** (1996) 266.
8) Reinhardt M., Beu M., Vosberg H., Herzog H., Hübinger A., Reinauer H., et al., J. Nucl. Med. **40** (1999) 977.
9) Tashiro M., Fujimoto T., Itoh M., Kubota K., Fujiwara T., Miyake M., et al., J. Nucl. Med. **40** (1999) 70.
10) Holloszy J.O., Hansen P.A., Rev Physiol. Biochem. Pharmacol. **128** (1996) 99.
11) Thorell A., Hirshman M.F., Nygren J., Jorfeldt L., Wojtaszewski J.F.P., Dufresne S.D., et al., Am. J. Physiol. 277(1999) E733.

VIII. 6. Exercise Induced Regulation of Whole-body Glucose Metabolism: A PET Study

Mehedi M.[1,2], Fujimoto T.[2], Tashiro M.[1], Miyake M.[1], Watanuki S.[1], and Itoh M.[1]

[1]*Division of Nuclear Medicine, Cyclotron and Radioisotope Center, Tohoku University*
[2]*Center for the Advancement of Higher Education, Tohoku University*

Abstract

Our aim was to visualize homeostatic energy regulation after exercise using ^{18}F-FDG and 3D-PET technique. Five healthy male subjects were studied with ^{18}F-FDG and 3DPET method after exercise task at 40% and 70% $\dot{V}O_{2max}$. Additional 6 subjects were studied as controls. ROIs were drawn to assess organ glucose metabolism in the skeletal muscles of thigh, lumbar/gluteal and upperlimb regions and visceral organs such as liver, heart and brain. Relative (standard uptake value, SUV) and absolute glucose metabolic rates (MRGlc) were calculated. Glucose metabolism was increased in the lowerlimb muscles and decreased in the viscera (i.e. Liver and Brain) at mild or moderate exercise loads, suggesting of homeostatic energy redistribution. Good correlation was found between SUV and MRGlc among all organs except for upperlimb muscles. ^{18}FDG-3DPET technique of muscles and visceral organs can give objective index of organ energy metabolism *in vivo* in human, which may have contributions in the sport and rehabilitation science.

Keywords: Exercise, Glucose metabolism, Whole-body, SUV, MRGlc.

Introduction

Regulation of organ metabolic consumption (i.e. glucose and fat) is necessary at exercise task[1]. During exercise, organ energy metabolism between organs are carried out from whole-body metabolic homeostasis. Previous reports[2,3] with semiquantification approach, mentioned the feasibility of glucose metabolic changes in the lower limb skeletal muscles and other organs after fixed exercise load, using ^{18}F-FDG and 3DPET method. Recently, Kemppainen J. and co-workers, assessed the glucose metabolism of single lowerlimb skeletal

muscle and myocardium using quantitative analysis[4]. However, no reports have assessed the absolute values of glucose metabolism (rMRGlc) at whole-body level after different exercise loads. Nuclear medicine technique, three dimensional positron emission tomography (3DPET) with administration of ^{18}FDG tracer[5], a glucose analogue, is a promising noninvasive imaging tool to elucidate organ activity from glucose metabolism as marker[6].

Our purpose was to evaluate workloads inducing whole-body organ glucose metabolism using semiquantitative and quantitative methods. We hypothesize, the redistribution of organ energy metabolism is implemented at whole-body level, when exercise is performed up to moderate workload.

Methods

Subjects

Eleven healthy male volunteers collaborated with this investigation. All subjects abstained from eating and drinking for at least 5 hours before the experiment. They were asked not to perform any kind of physical exercise from one day before investigation. Five subjects served as exercise group whose ages ranged from 21 to 23 years (Mean 21.80 ± 0.84 y). Another 6 subjects, aged mean 24 ± 5.34 y (Range; 19 ~ 33 y) were studied as resting control maintaining the same study protocol without exercise. ^{18}FDG dose for controls was in average 42.48 ± 6.63 MBq (Mean±SD.). A written fully informed consent was obtained from each subject before the study. This study protocol was approved by the Clinical Committee for Radioisotope Studies of Tohoku University.

Study Protocol

Ergometer bicycle exercise was arranged at 40% and 70% $\dot{V}O_{2max}$ workloads. $\dot{V}O_{2max}$ was measured by intermittent exercise on an ergometer bicycle (Monark 818E, Sweden), and the oxygen consumption rate was determined by an automated metabolic unit machine (AE280-S, Minato Co. Ltd. Osaka, Japan). Before the experiment, subjects rested for 20 minutes in a dim lit quiet room. One teflon catheter was inserted to their antecubital veins of the left hand for blood sampling to measure plasma glucose, lactate and insulin. Another teflon catheter was inserted to subject's antecubital vein of the opposite hand for [^{18}F]FDG administration. Then, they started ergometer bicycle riding at the speed of 60 revolution/min (Monark 818E, Sweden) at 40% and 70% $\dot{V}O_{2max}$ workloads. [^{18}F]FDG was injected through a catheter at 10 minutes later following exercise task. The radioactivity dose of the exercise

group was in average 38.37 ± 2.15 MBq (Mean ± SD). After the injection, subjects continued to pedal the bicycle for another 30 minutes, completing a total of 40 minutes task. Immediately after intravenous administration of FDG, heated arterialized venous blood was sampled from cubital vein opposite to the injection site. Plasma FDG concentrations were measured both during exercise and PET scan for 24 times. Plasma metabolite concentrations (i.e. Glucose, lactate and insulin) were measured at two points such as pre and post-exercise conditions.

Subjects lay down in supine position on PET table with eyes open following exercise task. The PET room was kept dimmed and quiet. The scan protocol was as follows: a 3 dimensional (3D) whole-body emission scan (3 min × 9 positions) was performed from the knee joint to the vertex followed by transmission scan (3 min × 9 frame) using a PET apparatus (SET2400 W, Shimadzu, Kyoto, Japan). The transmission scan (post-injection mode) was performed with a $^{68}Ge/^{68}Ga$ external rotating line source (370 MBq at purchase).

Calculation of glucose metabolism

ROIs were set on the skeletal muscles of thigh, lumbar/gluteal regions, upper-limb and visceral organs such as liver, heart, brain etc (Fig.1.). To evaluate the rate of glucose utilization, an autoradiographic method was applied using the equation shown below[7]:

$$rMRGlc = \frac{Cp}{LC}\left[\frac{K^*_1 k^*_3}{k^*_2 + k^*_3}\right]\left[\frac{C^* i(T) - C^* e(T)}{C^* m(T)}\right]$$

In another, semiquantitative analysis (Standard uptake value, SUV) was done by using the following equation:

$$\frac{Mean\ ROIcts\ (cps/pxls) \times Body\ weight(g)}{Injected\ dose\ (\mu Ci) \times Calibration\ factor\ (cps/\mu Ci)}$$

Statistical method

Group comparisons were done by using one-way analysis of variance (ANOVA) and Tukey's test (post-hoc analysis). The significant differences were set at $p<0.05$. Correlation was calculated using Pearson's correlation coefficient analysis.

Results

FDG uptake was only remarkable in the brain, heart and urinary bladder in the resting subject, while high uptake was visualized in the muscles of exercise conditions (Fig. 1).

Glucose metabolism (SUV and MRGlc) was increased in the skeletal muscles of thigh and lumbar/gluteal regions ($p<0.05$), and it was decreased in the brain ($p<0.05$) induced by 40% and 70% $\dot{V}O_{2max}$ workloads (Fig. 2). A correlation between SUV and MRGlc was found among organs (i.e. Thigh, lumbar/gluteal muscles, liver, heart and brain), except in the upperlimb muscles (Fig. 3 and Fig. 4). The changes in plasma metabolites were as follows: stable plasma glucose concentrations, an increase ($p<0.05$) plasma lactate concentration at post-exercise condition of 70% $\dot{V}O_{2max}$ (5.3±2.4 mmol/liter) to compare with pre-exercise condition (0.9±0.2 mmol/liter). The plasma insulin concentration was decreased ($p<0.05$) only at post-exercise workload of 70% $\dot{V}O_{2max}$ (2.0±0.7 U/mol) than pre-exercise condition (4.6±1.5 U/mol).

Discussions and Conclusion

Organ glucose uptake either increased or decreased almost linearly with the exercise loads up to moderate workload (70% $\dot{V}O_{2max}$). In spite of complexity of energy metabolic controls such as glucose-fatty acid metabolic interaction, aerobic-anaerobic interaction, and involvement of glycogenolysis[8], exercise workloads induced organ glucose metabolism were successfully assessed with ^{18}FDG-3DPET technique and two analytical approaches. Organ glucose uptake either increased or decreased almost linearly with the exercise loads up to moderate workload (70% $\dot{V}O_{2max}$), suggesting of homeostatic metabolic control. Semiquantitative method without blood samplings was found useful to estimate a rough trend of glucose consumptions. However, one organ failed to have good correlations between SUV and MRGlc, the upperlimb muscles for example, which demonstrates that semiquantitative approach needs a great care when metabolic rate of glucose utilization changes at whole-body level. ^{18}FDG-3DPET technique of muscles and visceral organs can give an objective index of organ energy metabolism *in vivo* in human, which may have contributions in the sport medicine and rehabilitation science.

Acknowledgements

This work was supported by a grant-in-aid (No. T Fujimoto) from the ministry of Education, Science, Sports and Culture, Japan and by the 13th Research-Aid Report in Medical Health Science of Meiji Life Foundation and Welfare.

References

1) Romijin J. A., Coyle E.F., Sidossis L.S., et al., J. Physiol. **265** (1993) E380.
2) Fujimoto T., Itoh M., H Kumano., et al., Lancet, **48** (1996) 266.
3) Tashiro M., Fujimoto T., Itoh M., et al., J. Nucl. Med. **40** (1999) 70.
4) Kemppainen J., Fujimoto T., Kari K.K., Viljanen T., Nuutila P., Knuuti J., J. Physiol. **542** (2002) 403.
5) Hamacher K., Coenen H.H., Stocklin G., J. Nucl. Med. **27** (1986) 235.
6) Harris M.L., Julyan P., Kulkarni B., et al., J. Cereb. Blood Flow Metab. **25** (2005) 520.
7) Phelps M.E., Huang S.C., Hoffman E.J., Selin C., Sokoloff L., Kuhl D.E., Ann. Neurol. **6** (1979) 371.
8) Kjaer M., Howlett K., Langfort J., et al., J. Physiol. **528** (2000) 371.

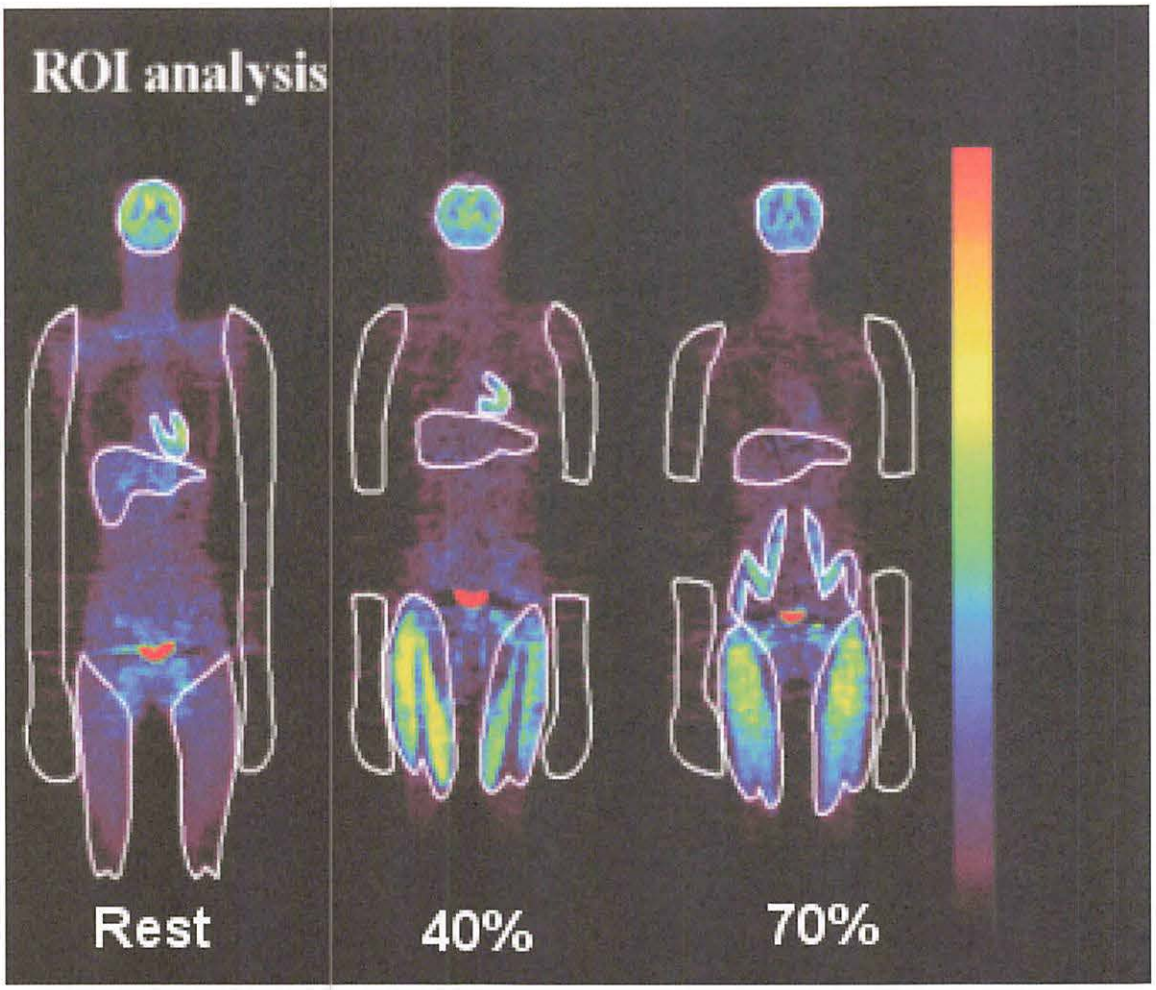

Figure 1. ROIs procedure in the individual organs, and ^{18}FDG uptake distributions are visualized at rest and different exercise loads (40% and 70% $\dot{V}O_{2max}$).

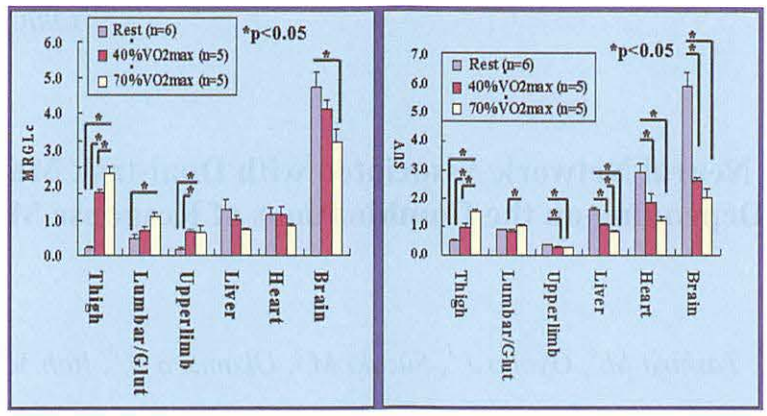

Figure 2. Glucose uptake changes (^{18}FDG uptake) after exercise loads (40% and 70% $\dot{V}O_{2max}$) were visualized in the skeletal muscles (i.e. Thigh, lumbar/gluteal region, and upperlimb) and visceral organs (i.e. Liver, heart and brain), demonstrating two analytical approaches (e.g., MRGLc and SUV).

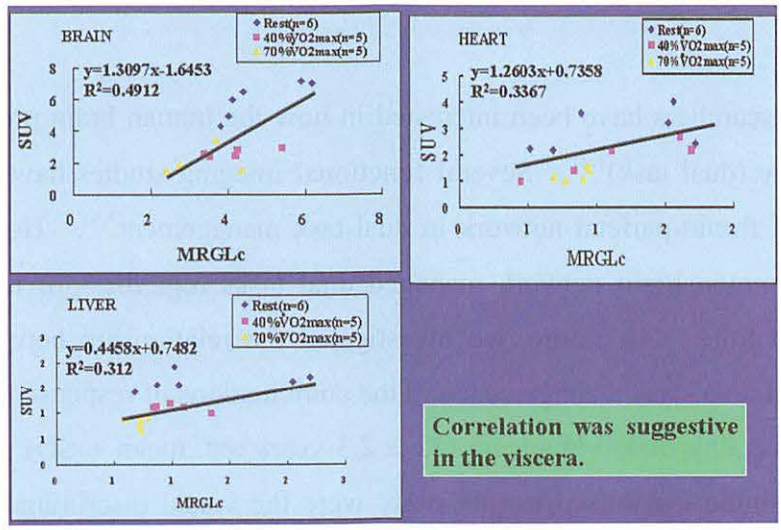

Figure 3. Correlation between SUV and MRGlc among visceral organs (i.e. Brain, liver and heart).

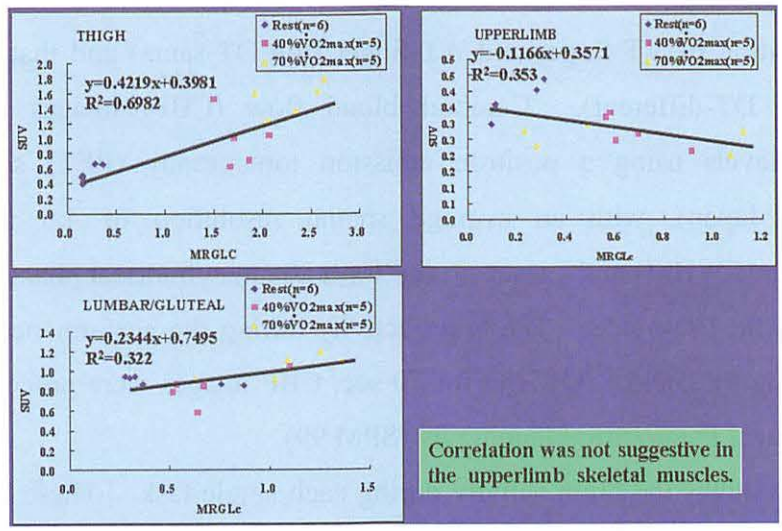

Figure 4. Correlation between SUV and MRGLc in the skeletal muscles (i.e. Thigh, lumbar/gluteal and upperlimb).

VIII. 7. Neural Network Associated with Dual-task Management Differs Depending on the Combinations of Response Modalities

Mochizuki H.[1,2], Tashiro M.[4], Gyoba J.[3], Suzuki M.[3], Okamura N.[2], Itoh M.[4] and Yanai K.[2]

[1]Department of Sensory-Motor Integration, National Institute for Physiological Science
[2]Department of Pharmacology, Tohoku University School of Medicin
[3]Department of Psychology, Graduate School of Arts and Letters, Tohoku University
[4]Cyclotron and Radioisotope Center, Tohoku University

Many researchers have been interested in how the human brain processes two things simultaneously (dual task)[1,2]. Several functional imaging studies have demonstrated the importance of fronto-parietal network in dual-task management[3,4]. However, it was still whether a common brain network managed dual tasks regardless of the combination of response modalities. Therefore, we investigated the relationship between brain activity associated with dual-task management and the combinations of response modalities.

Fifteen healthy male volunteers (22 ± 2.3 years old, mean ± SD) participated in this study. The single tasks used in this study were the visual discrimination task requiring finger response (left hand) (VT-finger) and the auditory discrimination tasks requiring finger responses (right hand) (AT-finger) and oral responses (AT-oral). The dual tasks were combination of VT-finger and AT-finger (the DT-same) and that of VT-finger and AT-oral (the DT-different). Cerebral blood flow (CBF) images were obtained at whole-brain levels using a positron emission tomography (PET) scanner (Shimadzu SET-2400W, Japan), with an average spatial resolution of 4.5 mm at full-width half-maximum (FWHM) and a sensitivity for a 20 cm cylindrical phantom of 48.6 k.c.p.s. KBq^{-1} ml^{-1} in the 3D-mode. The brain activity during the performance of the tasks was measured using PET and $[^{15}O]$-H_2O for 70 sec. CBF images were processed and analyzed using a Statistical Parametric Mapping 99 (SPM 99).

Figure 1 shows the brain activity during each single task. These brain regions were also activated during the dual tasks, but the neural activity activated in the single task condition was not significantly different from that in the dual task conditions. The premotor cortex, precuneus and posterior parietal cortex were significantly activated in the

DT-same condition, whereas the anterior and posterior parietal cortices were significantly activated in the DT-different condition (Fig. 2). These brain regions were not observed in the single task conditions. In addition, the neural activities in the right premotor cortex, precuneus and right posterior parietal cortex were significantly higher in the DT-same condition than in the DT-different condition, whereas the neural activities in the right anterior parietal cortex and right posterior parietal cortex were significantly higher in the DT-different condition than in the DT-same condition (Fig. 2). These results demonstrate that neural network associated with dual-task management differs depending on the combination of response modalities.

References

1) Pashler H., Psychol Bull. **116** (1994) 220.
2) Telford C.W., J Exp Psychol Hum Percept Perform. **14** (1931) 1.
3) D'Esposito M., Detre J.A., Alsop D.C., Shin R.K., Atlas S., Grossman M., Nature. **378** (1995) 279.
4) Szameitat A.J., Schubert T., Muller K., Von Cramon D.Y., J Cogn Neurosci. **14** (2002) 1184.

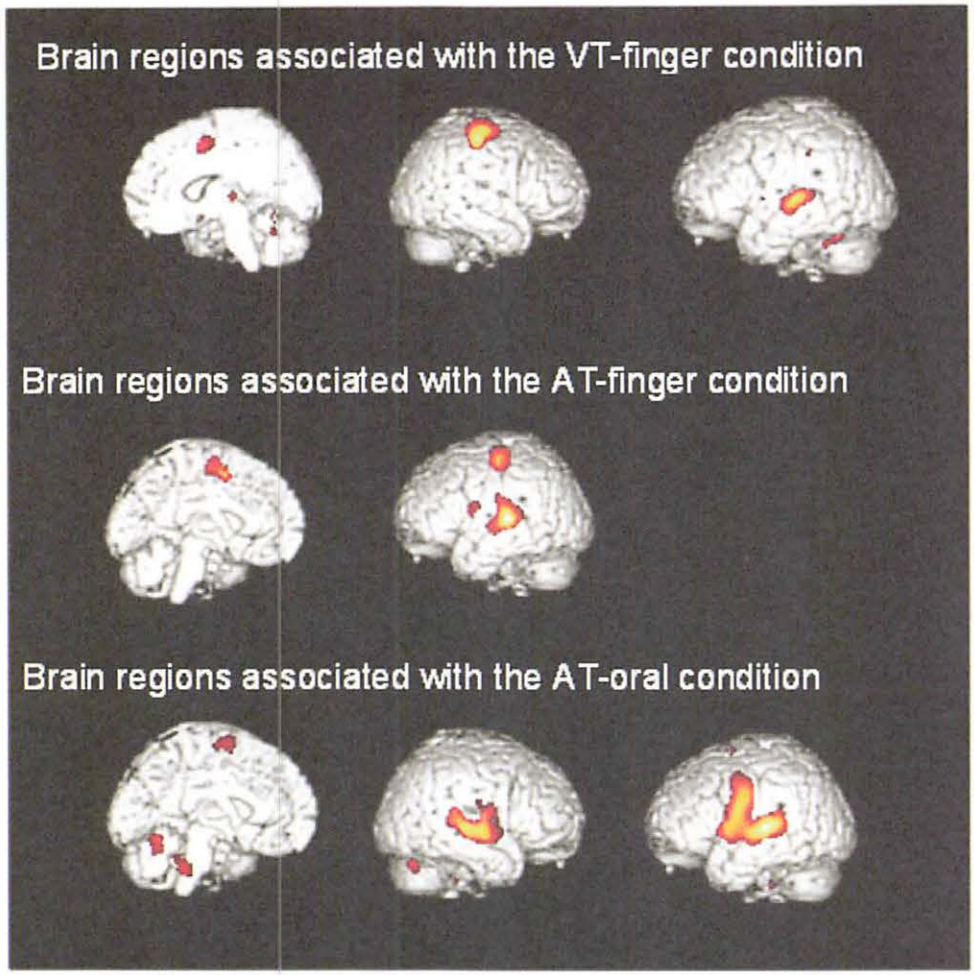

Figure 1. Brain regions activated in each single-task condition.

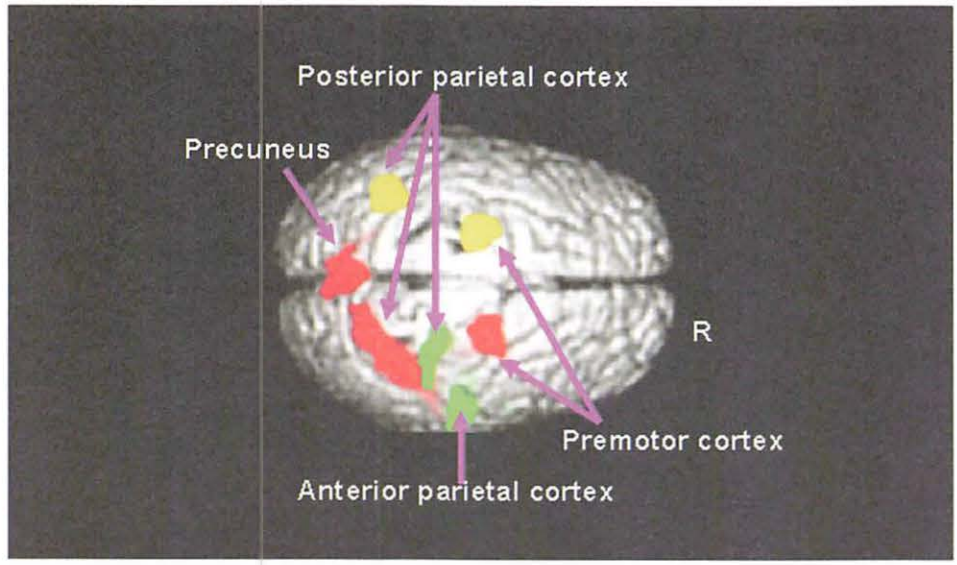

Figure 2. The difference in brain activity between the DT-same and DT-different conditions. Yellow: common brain regions, Red: specific for the DT-same condition, Green: specific for the DT-different condition. R: right hemisphere.

VIII. 8. Discrete Cortical Regions Associated with the Musical Beauty of Major and Minor Chords

Suzuki M.[1,2,3], Okamura N.[3], Kawachi Y.[2], Tashiro M.[4], Arao H.[5], Hoshishiba T.[6], Gyoba J.[2], and Yanai K.[3]

[1]*The Japan Society for the Promotion of Science*
[2]*Department of Psychology, Graduate School of Arts and Letters, Tohoku University*
[3]*Department of Pharmacology, Graduate School of Medicine, Tohoku University*
[4]*Division of Cyclotron Nuclear Medicine, Cyclotron and Radioisotope Center, Tohoku University*
[5]*Department of Kansei Design, Faculty of Psychological Science, Hiroshima International University*
[6]*Department of Media Technologies, School of Engineering, Nippon Bunri University*

Neural correlates of aesthetic pleasantness have been the subject of recent studies[1-6]. Those reports showed that aesthetic pleasantness utilizes the brain circuitry that is common to those involved in emotion and reward. However, it is unclear whether there is any specific brain activation corresponding to beauty derived from different "affective qualities".

Affective qualities refer to the various emotions and concepts represented by art that deeply touch our hearts. Some types of art conceptualize negative affective feelings such as sadness. Alternatively, artists also represent the positive side of human life (e.g., happiness). In music, minor and major modes—the main musical components—are closely related to whether negative or positive affective feelings are being expressed in musical pieces. Although the affective qualities of each mode are quite different[7-9], both produce an experience of beauty.

In this study, we investigated the neural correlates of perceiving the beauty of major and minor chords by using $[^{15}O]H_2O$ positron emission tomography. The aim of this study was to compare the rCBF changes elicited by the listening of beautiful major or minor consonant chords. Such a comparison would elucidate the specific brain areas responsible for the appreciation of the major and minor modes beyond the general reward-related system.

Method

Participants

The participants comprised 13 healthy males (20–26 years). All participants had normal hearing capacity and no history of neurological or psychiatric disease. The study protocol was approved by the Clinical Research and Ethics Committees of Tohoku University. All participants provided written informed consent to participate in the study.

Chord stimuli

13 participants selected their respective top five major and minor beautiful, and worst five major and minor ugly chord sequences from the 32 consonant/dissonant subsets (8 major consonant, 8 major dissonant, 8 minor consonant, and 8 minor dissonant sequences). In each sequence, eight chords were presented in succession at a rate of 1 chord/1.5 s, for a total duration of 12 s. Each chord consisted of four simultaneous tones played in a simulated piano mode with natural sustain. The selected sequences were assigned to each of the beautiful major consonance (B-MaC), ugly major dissonance (U-MaD), beautiful minor consonance (B-MiC), and ugly minor dissonance (U-MiD) conditions for each participant. Under each condition, the sequence perceived as the most beautiful or ugly was played first, followed by the other four sequences played in turn depending on the proximity of their keys. Finally, the most beautiful or ugly sequence was replayed. Total listening duration is 90 s in each condition.

Image acquisition and procedure

A three-dimensional PET was obtained using a SET2400W scanner (Shimadzu) in accordance with previously described methods[10]. Briefly, the participants were scanned for 70 s after an intravenous administration of approximately 5 mCi (185 MBq) of $[^{15}O]H_2O$ through an antecubital vein. A total of ten scans were conducted. Resting scans were performed during the first and last sessions. During the remaining eight scans, the chord sequences corresponding to each of the four conditions were presented in a counterbalanced order among the participants. After each scan, they were asked to rate the beauty of the chord sequence on a 7-point scale (1: most ugly, 7: most beautiful).

Statistical analysis of PET images

The SPM2 software (Welcome Department of Cognitive Neurology, London) was used for image realignment, normalization, and smoothing and to create statistical maps of

significant rCBF changes[11]. The normalized images were smoothed using a 12 × 12 × 12 mm Gaussian filter. The rCBF values were expressed as ml dl^{-1} min^{-1}, adjusted by the analysis of covariance, and were scaled to a mean of 50. The t-statistics were computed for each voxel in order to draw a comparison between the four experimental conditions and the resting condition. For an analysis of these comparisons, the threshold for significant voxels was set at $p < .0001$, uncorrected for multiple comparisons. At the cluster level, the threshold was set at corrected $p < .05$ for all subtraction analyses in order to reduce accidental findings due to Type I errors.

Results

Behavioral results

Two-way ANOVA (beautiful consonance/ugly dissonance × major/minor) was performed for behavioral data. Results revealed that the average rating score of the beautiful consonant chords was significantly higher scores than that of the ugly dissonant chords, regardless of the mode (major or minor) ($p < .001$; Fig. 1). Additionally, the major chords generally scored higher than the minor chords ($p < .001$). The average rating score of the beautiful major consonant chords was higher than that of the beautiful minor consonant chords ($p < .001$), whereas no significant difference was found between the mean ratings of the ugly major and minor dissonant chords.

Imaging results

We conducted the subtraction analyses to identify the brain areas that responded specifically to beautiful consonant or ugly dissonant music ($p < .0001$, uncorrected; Table 1). Listening to beautiful consonant chords, when compared to the ugly dissonant ones, induced significant activities in the dorsomedial midbrain. In contrast, when compared to beautiful consonant chords, ugly dissonant chords evoked significant activations of the right inferior parietal lobule, left insula, and left frontal sub-gyral (Table 1). Moreover, the rCBF of the dorsomedial midbrain activated by beautiful consonant chords, as compared to the ugly dissonant ones, was positively correlated with the subjective rating scores ($p < .05$). On the other hand, significantly negative correlations were found between the rating scores and rCBF of the IPL /left insula, when comparing ugly dissonant chords with beautiful consonant ones ($p < .05$).

In addition, a subtraction analysis comparing the major with minor chords regardless

of beauty showed no significant activation; however, the inverse subtraction showed activation of the left parahippocampal gyrus ($p < .0001$, uncorrected; Table 1).

We also conducted subtraction analyses to investigate specific regions corresponding to listening to the major beautiful and minor beautiful chords. A comparison between B-Mac (beautiful major consonant condition) versus U-MaD (ugly major dissonant condition) revealed that rCBF increases in the left middle temporal gyrus and the right fusiform gyrus ($p < .0001$, uncorrected; Table 2). A comparison between B-MaC versus B-MiC conditions also revealed significant rCBF in the left middle temporal gyrus (Table 3, Fig. 2). In contrast, areas of significantly higher rCBF during the presentation of the minor beautiful consonant chords as compared with the minor ugly dissonant chords appeared in the left dorsomedial midbrain, left rectal gyrus, right cerebellar tonsil, right inferior frontal lobule, left cingulate gyrus, left anterior cingulate gyrus, and right corpus striatum (Table 2). The right corpus striatum and culmen also displayed strong significant activations when comparing the B-MiC with B-MaC conditions (Table 3, Fig. 2).

Discussion

This study revealed the cortical regions responsible for the affective processing involved in listening to major/minor musical chords. Minor beautiful consonant chords in contrast with the minor ugly dissonant ones strongly activated several distinct spatial regions associated with reward and emotion. In contrast, no significant activations of those areas were observed during listening to major beautiful consonant chords as compared with when listening to major ugly dissonant ones despite the fact that the behavioral scores of the major beautiful consonant chords are significantly higher than those of the minor dissonant ones. These results suggest that the major and minor musical modes of beauty are represented in different areas of the brain, and the activations of the reward nerve system do not always have to correspond with an intensity of the subjective feeling of beauty.

A comparison between minor and major beautiful music revealed that the striatum and the MTG are important sites for the processing of minor or major beautiful consonant music, respectively. The striatum, which is projected by the dopaminergic neurons of the midbrain, is one of the most important regions that operate the reward system. Therefore, pleasure evoked by minor music is akin to reward and might stir up strong emotions in humans. On the other hand, the left MTG activated by the major beautiful chords is reported to mediate word processing—in particular, orthographic word or morphologic information processing[12-14]. The left MTG appears to be related to coherent and orderly

information processing. In the theory of harmonics, a major triad appears to exhibit more natural and fundamental characteristics of the physical nature of sound than does a minor triad[8].

Our findings primarily demonstrate that these different affective qualities, both of which are perceived within the realm of "beauty," are represented in distinct brain regions. This differential representation might underlie in part the depth and complexity of aesthetic pleasure evoked by art.

Acknowledgement

This study was supported by a JSPS Research Fellowship for Young Scientists to the first author (no. 184848) and by a MEXT Grant-in-Aid for Scientific Research to the seventh author (no. 18650063).

References

1) Blood A.J., et al., Nat. Neurosci. **2** (1999) 382.
2) Blood A.J., Zatorre R. J., Proc. Natl. Acad. Sci. USA. **98** (2001) 11818.
3) O'Doherty J., et al., Neuropsychologia **41** (2003) 147.
4) Brown S., et al., Neuroreport **15** (2004) 2033.
5) Kawabata H., Zeki S.J., Neurophysiol. **91**(2004) 1699.
6) Jacobsen T., et al., Neuroimage **29** (2006) 276.
7) Hevner K., Am. J. Psychol. **47** (1935) 103.
8) Crowder R.G., Psychomusicology **4** (1984) 3.
9) Gagnon L., Peretz I., Cognition Emotion **17** (2003) 25.
10) Okamura N., et al., Br. J. Pharmacol. **129** (2000) 115.
11) Friston K.J., et al., Hum Brain Mapp. **2** (1995) 189.
12) Sakai K.L., et al., Neurosci. Res. **39** (2001) 1.
13) Gernsbacher M.A., KaschaK M.P., Annu, Rev. Psychil. **54** (2003) 91.
14) Vigneau M., et al., Neuroimage **27** (2005) 694.

Table 1 The coordinates and Z-scores for the brain areas in subtraction analyses, Beauty consonance versus Ugliness dissonace conditions, and Major versus Minor conditions

Region	Side	Z-score	Talairaha Cordinates x, y, z
Beauty consonance vs Ugliness dissonance			
Dosomedial midbrain	L	3.97	-10, -28, -14
Ugliness dissonance vs Beauty consonance			
Inferior prietal lobule	R	3.56	57, -32, 53
Insula	L	3.30	-46, -15, 3
Frontal sub-gyral	L	3.30	-26, 20, 16
Minor vs Major			
Parahippocampus	L	3.45	-24, -35, -3

L = left, R = right

Table 2 The coordinates and Z-scores of brain regions in direct comparisons between B-MaC/B-MiC and U-MaD/U-MiD

	Side	Z-score	Talairaha Cordinates x, y, z
B-MaC vs U-MaD			
Middle temporal gyrus	L	3.77	-61, -1, 18
Fusiform gyrus	R	3.33	61, -15, -30
B-MiC vs U-MiD			
Dorsomedial midbrain	L	3.92	-10, -30, -13
Rectal gyrus	L	3.78	-6, 18, -28
Cerebellar tonsil	R	3.60	14, -60, -32
Inferior frontal gyrus	L	3.54	32, 31, 2
Cingulate gyrus	L	3.40	-4, -14, 32
Anterior cingulate gyrus	L	3.35	-8, 33, -2
Corpus striatum	R	3.34	32, -9, 10

L = left, R = right

B-MaC = beautiful major consonance, U-MaD = ugly major dissonance

B-MiC = beautiful minor consonance, U-MiD = ugly minor dissonance

Table 3 The coordinates and Z-scores of brain regions revealed by direct comparisons between B-MaC and B-MiC

	Side	Z-score	Talairaha Cordinates x, y, z
B-MaC vs B-MiC			
Middle temporal gyrus	L	3.77	-61, 3, -20
B-MiC vs B-MaC			
Corpus striatum	R	4.39	30, -15, 11
Culmen	L	3.43	-34, -44, -21

L = left, R = right

B-MaC = beautiful major consonance, B-MiC = beautiful minor consonance

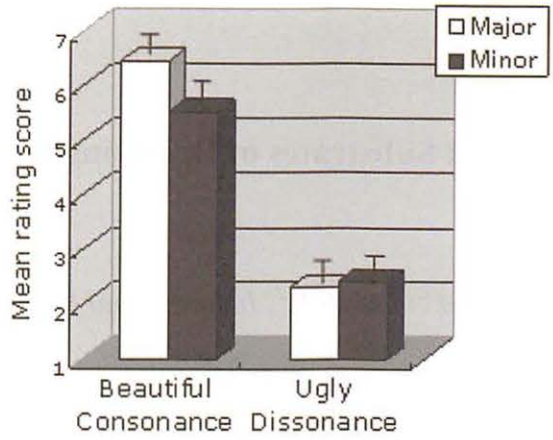

Figure 1. Mean rating scores of musical chord stimuli in each of the four conditions based on the behavioral results obtained after each PET scan. Each bar illustrates the standard error of each relative condition.

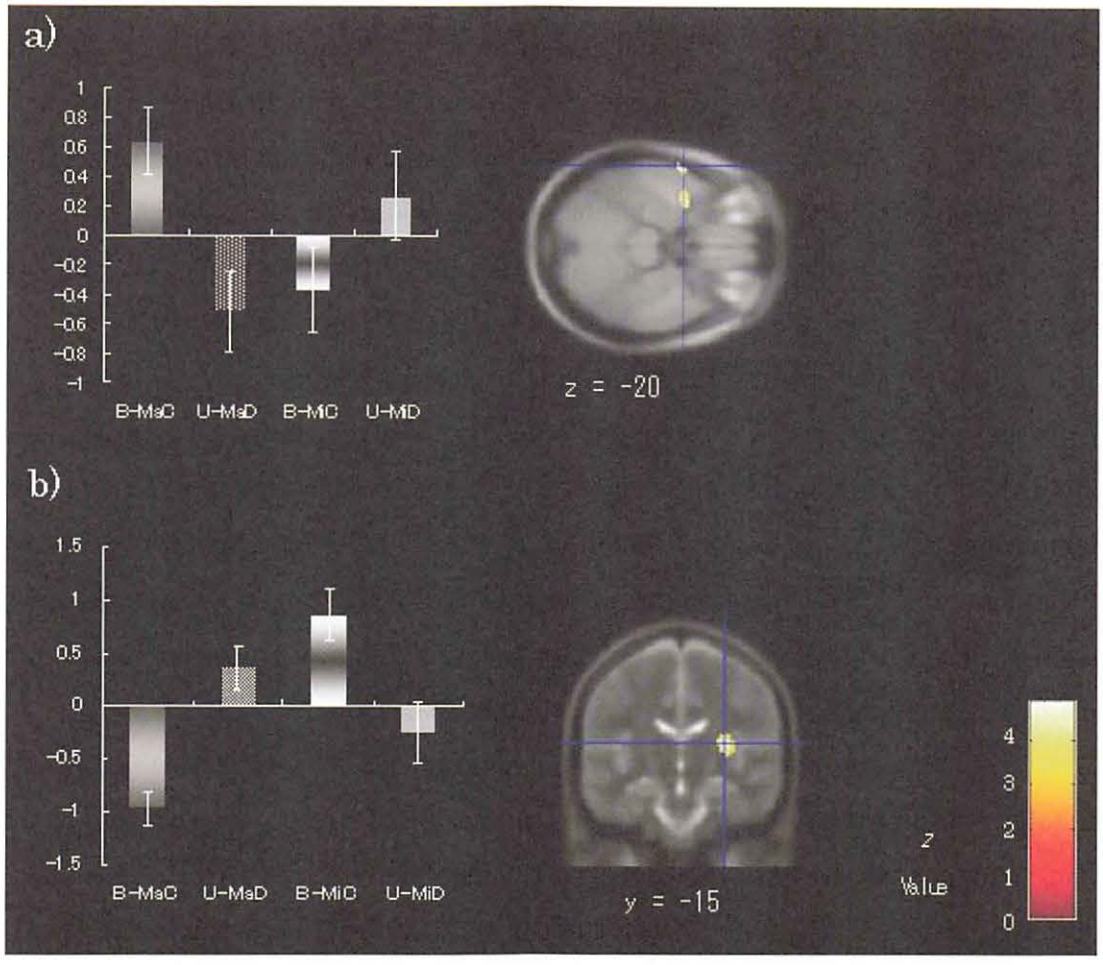

Figure 2. Neuroanatomical regions demonstrating significant increases in rCBF upon the subtraction of the B-MiC images from those of B-MaC (a) and vice versa (b). B-MaC compared with B-MiC increased rCBF in the left middle temporal gyrus (axel section; z = –20 mm), whereas B-MiC compared with B-MaC increased rCBF in the right corpus striatum (coronal section; y = –15 mm). Each bar shows the standard error of each relative condition. B-MaC, U-MaD, B-MiC, and U-MiD signify the beautiful major consonance ugly major dissonance, beautiful minor consonance, and ugly minor dissonance conditions, respectively.

VIII. 9. Neural Substrates of Deceiving Others

Abe N.[1], Suzuki M.[1,2], Mori E.[1], Itoh M.[2], and Fujii T.[1]

[1]Department of Behavioral Neurology and Cognitive Neuroscience, Tohoku University Graduate School of Medicine
[2]Division of Cyclotron Nuclear Medicine, Cyclotron and Radioisotope Center, Tohoku University

Since the pioneering research of Spence et al.[1)], an increasing number of neuroimaging studies have shown contributions of the prefrontal cortex to deception[2-14)]. Although subregions of this area have been differentially activated in these studies, their precise roles in relation to deception are still unclear. Previous neuroimaging studies of deception have focused on the truthfulness of responses as an essential factor (simple fabrication, i.e., the processes of inhibition of true responses and the production of deceptive ones). However, the reported activations of the prefrontal cortex might not be solely associated with processes of falsifying responses, because deception is not a simple mental activity, but rather a complex one composed of various cognitive functions. Although the inhibition of true responses and the production of deceptive ones are prerequisites for deception, the intention of deceiving others (deception with social interactions, i.e., deluding a questioner, irrespective of whether or not a response is truthful), which is likely to be accompanied by emotional regulation or social interaction, must be regarded as another important determinant for human deception.

In the present positron emission tomography (PET) study, the subjects performed the following four tasks. (1) An Honest-Truth task (HT): subjects were instructed by the interrogator to tell the truth about their past memories. (2) An Honest-Lie task (HL): subjects were instructed by the interrogator to tell lies about their past memories. (3) A Dishonest-Truth task (DT): subjects were instructed by the interrogator to tell lies about their past memories, but approximately 2 minutes before the initiation of this task, another experimenter (the second experimenter) secretly asked the subjects to deceive the interrogator by answering the questions truthfully. (4) A Dishonest-Lie task (DL): subjects were instructed by the interrogator to tell the truth about their past memories, but

approximately 2 minutes before the initiation of this task, the second experimenter secretly asked the subjects to deceive the interrogator by answering the questions untruthfully. Regional cerebral blood flow (rCBF) was measured using PET (SET2400W Shimadzu, FWHM 4.0 mm) and ^{15}O-labeled water (approximately 180 MBq for each injection). The PET data were analyzed with SPM2 (Wellcome Department of Imaging Neuroscience, UK).

To identify the brain regions associated with the two factors of deception, main effects of each factor were calculated from the functional imaging data. The main effect of falsifying the truthful responses {(HL – HT) + (DL – DT)} revealed significant activations in the left dorsolateral prefrontal cortex (BA8/9), left precuneus (BA7), left cerebellum, right anterior prefrontal cortex (BA10), and right cuneus (subcortical). The main effect of deceiving the interrogator {(DT – HT) + (DL – HL)} revealed significant activations in the left ventromedial prefrontal cortex (BA11), left precuneus (subcortical), left cerebellum, right middle temporal gyrus (BA38), right inferior temporal gyrus (BA20/38), and right cerebellum. At this stage of the analysis, setting a more lenient threshold ($p < 0.005$, cluster size > 15), we further examined whether or not the amygdala showed increased activity in either main effect. In the main effect of deceiving the interrogator, activation was detected in the left amygdala. Table 1 summarizes the data for anatomical structures and Brodmann's area, Montreal Neurological Institute (MNI) coordinates, Z-values, and cluster sizes of peak activations. The activated regions of interest are illustrated in Fig. 1.

The functional imaging data revealed that the left dorsolateral and right anterior prefrontal cortices were associated with the process of falsifying the truthful responses. Activations of the lateral prefrontal cortices related to the inhibition of true responses and the production of deceptive ones are likely to reflect executive function such as working memory and cognitive control. The left ventromedial prefrontal cortex and the amygdala were associated with the process of deceiving the interrogator. This result might be related to the previous findings that both the amygdala and the ventromedial prefrontal cortex are associated with emotional processing. Our results provide direct evidence for dissociable brain activities of prefrontal subregions and the amygdala in relation to the two different aspects of deception.

References

1) Spence S.A., Farrow T.F., Herford A.E., Wilkinson I.D., Zheng Y., Woodruff P.W., Neuroreport **12** (2001) 2849.
2) Abe N., Suzuki M., Tsukiura T., Mori E., Yamaguchi K., Itoh M., Fujii T., Cereb Cortex **16** (2006) 192.
3) Davatzikos C., Ruparel K., Fan Y., Shen D.G.., Acharyya M., Loughead J.W., Gur R.C., Langleben D.D., Neuroimage **28** (2005) 663.
4) Ganis G., Kosslyn S.M., Stose S., Thompson W.L., Yurgelun-Todd D.A., Cereb Cortex **13** (2003) 830.
5) Kozel F.A., Johnson K.A., Mu Q., Grenesko E.L., Laken S.J., George M.S., Biol Psychiatry **58** (2005) 605.
6) Kozel F.A., Padgett T.M., George M.S., Behav Neurosci **118** (2004) 852.
7) Kozel F.A., Revell L.J., Lorberbaum J.P., Shastri A., Elhai J.D., Horner M.D., Smith A., Nahas Z., Bohning D.E., George M.S., J Neuropsychiatry Clin Neurosci **16** (2004) 295.
8) Langleben D.D., Loughead J.W., Bilker W.B., Ruparel K., Childress A.R., Busch S.I., Gur R.C., Hum Brain Mapp **26** (2005) 262.
9) Langleben D.D., Schroeder L., Maldjian J.A., Gur R.C., McDonald S., Ragland J.D., O'Brien C.P., Childress A.R., Neuroimage **15** (2002) 727.
10) Lee T.M., Liu H.L., Chan C.C., Ng Y.B., Fox P.T., Gao J.H., Neuroimage **28** (2005) 305.
11) Lee T.M., Liu H.L., Tan L.H., Chan C.C., Mahankali S., Feng C.M., Hou J., Fox P.T., Gao J.H., Hum Brain Mapp **15** (2002) 157.
12) Mohamed F.B., Faro S.H., Gordon N.J., Platek S.M., Ahmad H., Williams J.M., Radiology **238** (2006) 679.
13) Nunez J.M., Casey B.J., Egner T., Hare T., Hirsch J., Neuroimage **25** (2005) 267.
14) Phan K.L., Magalhaes A., Ziemlewicz T.J., Fitzgerald D.A., Green C., Smith W., Acad Radiol **12** (2005) 164.

Table 1. Brain regions showing activation in each main effect of deception.

Region (Brodmann's Area)	MNI coordinates			Z value	Cluster size
	x	*y*	*z*		
Main effect of falsifying the truthful responses {(HL – HT) + (DL - DT)}					
Left dorsolateral prefrontal cortex (8/9)	-32	26	56	3.49	24
Left precuneus (7)	-12	-60	50	3.64	34
Left cerebellum	-10	-72	-28	4.53	48
Right anterior prefrontal cortex (10)	36	62	-2	4.11	19
Right cuneus (subcortical)	26	-70	14	3.74	22
Main effect of deceiving the interrogator {(DT – HT) + (DL - HL)}					
Left ventromedial prefrontal cortex (11)	-2	42	-16	3.93	18
Left precuneus (subcortical)	-14	-56	42	3.59	22
Left cerebellum	-14	-74	-48	3.54	29
Left amygdala※	-26	0	-26	2.95	24
Right middle temporal gyrus (38)	34	12	-34	3.96	53
Right inferior temporal gyrus (20)	50	8	-40	3.86	20
Right cerebellum	34	-54	-42	3.47	18

All peaks $p < 0.001$ uncorrected, except ※$p < 0.005$.

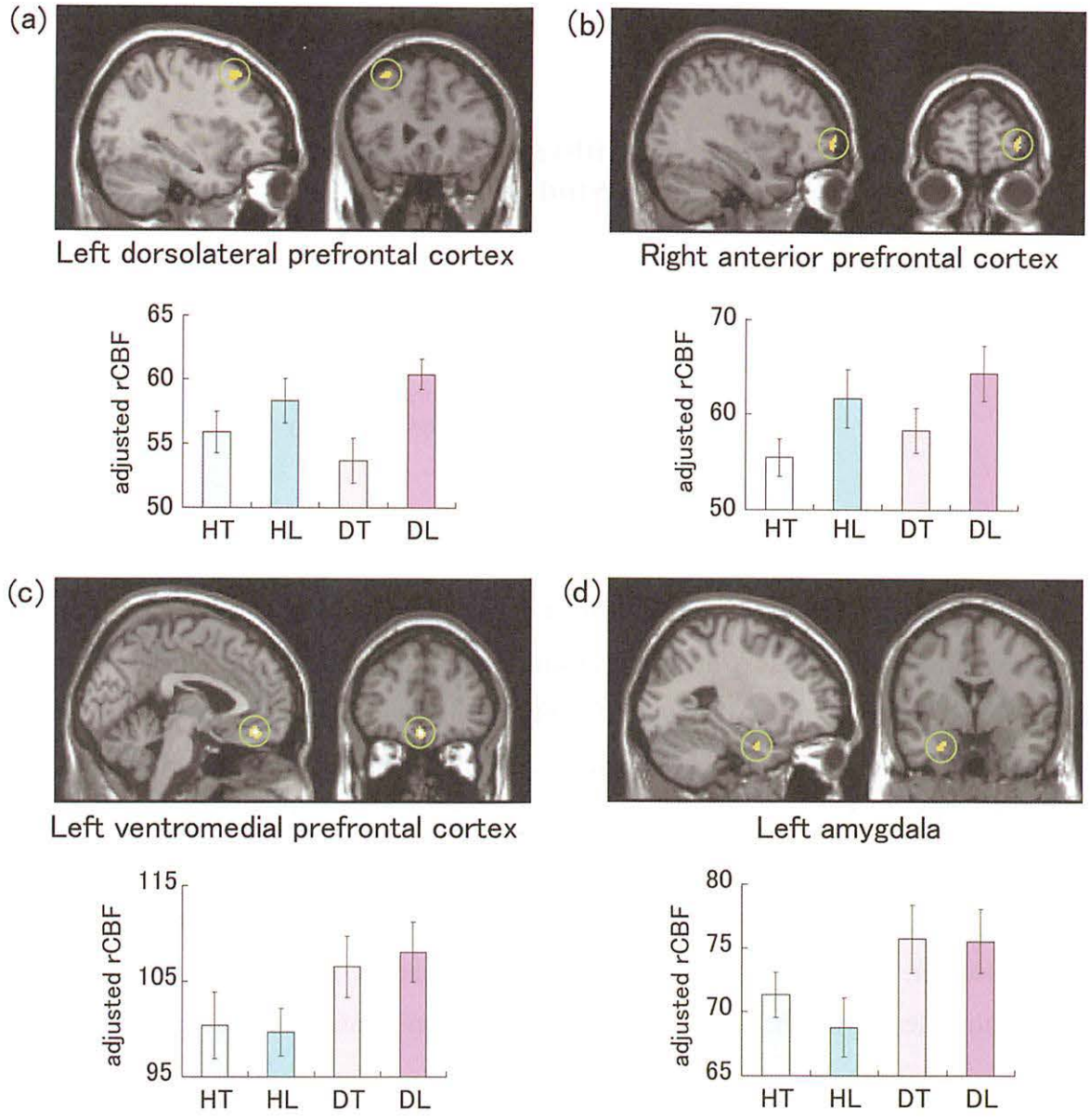

Figure 1. Activations of (a) the left dorsolateral prefrontal cortex, (b) the right anterior prefrontal cortex, (c) the left ventromedial prefrontal cortex, and (d) the left amygdala. The activations are superimposed onto magnetic resonance images of MNI templates ($p < 0.005$ for a display purpose). Histogram bars represent the rCBF values (mean ± s.e.m.) adjusted by global normalization during the four tasks. HT, Honest-Truth task; HL, Honest-Lie task; DT, Dishonest-Truth task; and DL, Dishonest-Lie task.

VIII. 10. Reviewed Article: Alexithymia and Awareness of Internal State in Human: A Study with $H_2{}^{15}O$ PET

Kano M.[1], Hamaguchi T.[1], Itoh M.[2], Yanai K.[1], and Fukudo S.[1]

[1]Graduate School of Medicine, Tohoku University
[2]Cyclotron Radioisotope Center, Tohoku University

Alexithymia: Clinical Significance

Alexithymia is a personality construct derived from clinical observations of patients with psychosomatic illness[1)], and is characterized by the followings: reduced ability to identify and describe one's feelings, difficulty in distinguishing feelings from the bodily sensations of emotional arousal, impaired symbolization, and a tendency to focus on external events rather than inner experiences[2)]. High rates of alexithymia have been reported in patients with essential hypertension, myocardial infarction, inflammatory bowel disease (IBD), functional gastrointestinal disorders (FGIDs), chronic pain, somatization, panic disorder, eating disorders, and post-traumatic stress disorders[3)]. These findings suggest that alexithymia has aversive effects not only on mental health but also on physical health.

Empirical studies indicate that alexithymia exacerbates physical illness. However, direct evidence to explain the mechanism of this exacerbation has not been provided. One hypothesis is that alexithymics amplify unpleasant internal signals. We review trends of studies on alexithymia including our study[18)] which we investigated how alexithymia influences sensitivity to visceral stimulation in human.

Visceral Stimulation and PET

In 45 non-clinical healthy subjects (34 males and 11 females), brain processing of visceral sensation induced by colonic distension was examined using $H_2{}^{15}O$ positron emission tomography (PET)[18)]. Subjective feeling evaluated on an ordinate scale and neuroendocrine response to stimuli were also measured. The degree of alexithymia was determined using the 20-item of Toronto alexithymia scale (TAS-20), and the correlation

between reaction to stimuli and the scores of TAS-20 and its three subscale [difficulty to identify feelings (DIF), difficulty to describe feelings (DDF) and external oriented thinking (EOT)] was evaluated. Statistical parametric mapping software (SPM2, Wellcome department of Cognitive Neurology, London, UK) was used create statistical maps of significant rCBF changes.

Recognition of Internal State and Activated Brain Region

At stimulation with the pressure of 40 mmHg, TAS-20 score significantly correlated with abdominal distention ($r = 0.3$, $p < 0.05$) and anxiety ($r = 0.3$, $p < 0.05$), while the score of DIF (difficulty to identify feelings) correlated with abdominal distention ($r = 0.27$, $p < 0.05$), abdominal pain ($r = 0.34$, $p < 0.05$), urgency for defecation ($r = 0.31$, $p < 0.05$), perceived stress ($r = 0.3$, $p < 0.05$), sleepiness ($r = -0.3$, $p < 0.05$) and anxiety ($r = 0.28$, $p < 0.005$)[18]. The scores of DDF (difficulty to describe feelings) and EOT (externally oriented thinking) did not correlate with any subjective perception.

TAS-20 score positively correlated with blood level of adrenaline ($r = 0.29$, $p < 0.05$), while the score of DIF positively correlated with blood levels of ACTH ($r = 0.33$, $p < 0.05$) and adrenaline ($r = 0.39$, $p < 0.01$). In contrast, the score of EOT negatively correlated with blood levels of ACTH ($r = -0.31$, $p < 0.05$) and adrenaline ($r = -0.27$, $p < 0.05$).

Areas of the brain where rCBF was higher in the alexithymics than in the non-alexithymics were: the right insula, middle frontal gyrus, midbrain, pregenual anterior cingulte gyrus, superior temporal gyrus, and postcentral gyrus (uncorrected $p<0.001$, Figure). TAS-20 scores positively correlated with both activity in the right insula and orbital gyrus and adrenaline levels in the blood in response to stimulation(uncorrected $p<0.001$). The score of DIF positively correlated with rCBF in the orbital gyrus, insula, frontal gyrus and cerebellum (uncorrected $p<0.001$).

Link of Alexithymia and Brain Function in Stress-related Disorders

The present study demonstrates that alexithymia is associated with hypersensitivity to visceral stimulation induced by colonic distension. Activation of brain areas associated with alexithymia, such as the pregenual anterior cingulate cortex, right insula and midbrain, supports afferent representation of bodily states, and efferent autonomic and endocrine responses that accompany it[4-8]. Alexithymics may be more aroused by interoception of unpleasant feeling than non-alexithymics thereby displaying more autonomic responses.

The results of this study support the somatosensory amplification hypothesis on alexithymia and could be used to confirm the results of clinical reports showing that alexithymia is associated with pain sensitivity in several chronic pain samples[9,10]. Although previous neuroimaging studies indicate that alexithymics were impaired in cognitive processing of emotion[11-13], the present study demonstrates that individuals with high alexithymia were more emotionally distressed and displayed excessive arousal to visceral sensation. Subjects with alexithymia might be less aware of affective stimuli at the cognitive level but highly aroused by affective stimuli at the physiological level. Previous studies showed that alexithymia was associated with gastrointestinal symptoms with no relation to endoscopic findings in 1141 patients[14] and high rate of alexithymia observed in FGID patients[15], the alexithymia construct itself is not something that can be ignored to study FGIDs. Our results are regarded as primary mechanisms of symptom development in FGIDs[16,17]. We believe that understanding the influence of alexithymia and cognitive emotional processing on brain-gut function would be useful to elucidate the pathophysiology of FGIDs.

Conclusion

The study from our institution[18] demonstrates that alexithymia is associated with hypersensitivity to visceral colonic stimulation. Our results show a positive correlation between TAS-20, and 1- activation of specific brain areas, 2- changes in blood neuroendocrine levels, and 3- subjective perception. These results support the somatosensory amplification hypothesis on alexithymia and could be one of the key mechanisms to explain the link between alexithymia and physical illness, especially FGIDs.

References

1) Sifneos P.E., patients. Psychotherapy and Psychosomatics **21** (1973) 133.
2) Taylor G.J., Bagby R.M., Parker J.D.A., Disorder of affect regulation: Alexithymia in medical and psychiatric illness. New York: Cambridge Univ Press; (1997).
3) Taylor G. J., Can. J. Psychiatry **45** (2000) 134.
4) Craig A.D., Nat. Rev. Neurosci. **3** (2002) 655.
5) Critchley H.D., Wiens S., Rotshtein P., Ohman A., Dolan R.J., Nat. Neurosci. **7** (2004)189.
6) Vogt B.A., Nat. Rev. Neurosci. **6** (2005) 533.
7) Barbas H., Brain Res. Bull. **52** (2000) 319.
8) Dunckley P., et al., J. Neurosci. **25** (2005) 7333.
9) Lumley M.A., Stettner L., Wehmer J., Psychosom. Res. **41** (1996) 505.
10) Lumley M.A., et al., Pain Med. **6** (2005) 251.
11) Berthoz S., et al., Am. J. Psychiatry **159** (2002) 159.
12) Kano M., et al., Brain **126** (2003) 126.
13) Mantani T., et al., Biol. Psychiatry **57** (2005) 982.
14) van Kerkhoven L.A., et al., J. Clin. Gastroentero. **40** (2006) 195.
15) Porcelli P., et al., Psychosom. Med. **65** (2003) 911.

16) Mertz H., Gut **51** (2002) 29.
17) Delvaux M., Gut **51** (2002) 67.
18) Kano M., et al., Pain, epub ahead of print (2007).

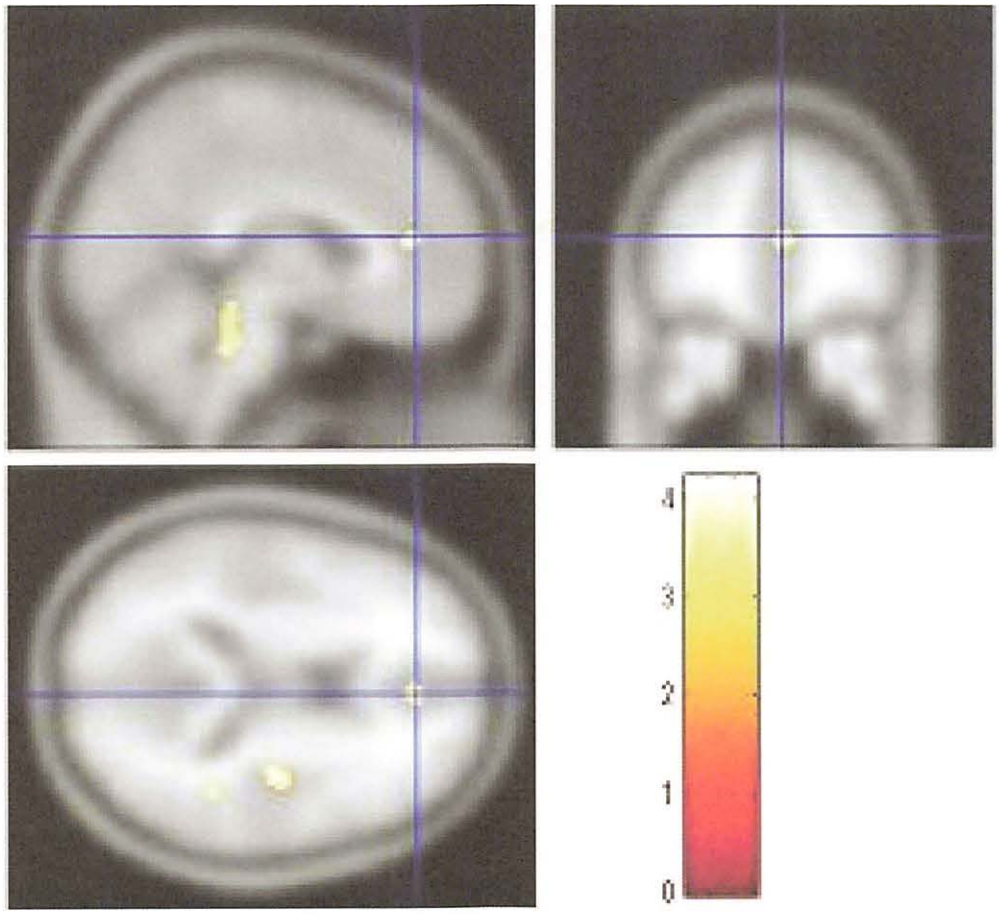

Figure 1. A statistical parametric map (SPM) showing the pregenual anterior cingulate cortex, midbrain, and right insula where rCBF was higher in the alexithymic subjects than in the non-alexithymics during colonic distension with a bag pressure of 40 mmHg ($p<0.001$, uncorrected).

IX. RADIATION PROTECTION AND TRAINING OF SAFETY HANDLING

IX. 1. Beginners Training for Safe Handling of Radiation and Radioisotopes in Tohoku University

Baba M., Yamazaki,H., Miyata T., and Iwata R.

Cyclotron and Radioisotope Center, Tohoku University

During 2006, the beginners training for safe handling of radiation and radioisotopes in Tohoku University was conducted in three courses as usual:
1) Radiation and Isotopes, 2) X-ray Machines and Electron Microscope, and 3) Synchrotron Radiation (SOR). The training was held twice a year, May and November, under the help for lectures and practice from various departments and research institutes of the university.

Lectures in English which were started in November of 2002 were continued for students and/or researchers who are not so familiar with Japanese language, by using PC projector and text of copies of view graphs (English class). The membership of the English class is almost constant as shown later.

The training for "Radiation and Radioisotopes" is for persons who use unshielded radioisotopes and accelerators, and has been conducted from 1977. The contents of lectures and practices are shown in Table 1. The order and content of the lecture was slightly modified from last November aiming at better understanding by trainees: the lecture on "the effect of radiation on human" was moved to the second to give stronger motivation for the training course and the following lectures. Along with the change, a new introductory lecture of "Introduction to radiation" was newly prepared as the first lecture to provide knowledge required to understand the lecture of "the effect of radiation on human". In the fiscal year of 2006, the training was performed for 465 persons (21 persons in the English class). The departments or institutes to which they belong are given in Table 2.

The training for "X-ray machines and electron microscopes" started at the end of 1983. The training is scheduled twice a year at the same time as that for "Radiation and Radioisotopes". In this course, only lectures are given with no practice. The contents of the lectures and the distributions of trainees are shown in Table 3 and Table 4, respectively. The number of trainees was 354 (37 in the English class).

The training for the "Synchrotron Radiation" began at the end of 1995. The contents of the lectures are the same as those of the radiation and radioisotopes but no practice. In 2006, the number of trainees of the SOR course was 88 (3 in the English class).

Table 1. Contents of the lectures and practices for safe handling of radiation and radioisotopes in 2006.

Lectures (one day)	Hours
Introduction to radiation	0.5
Effects of radiation on human	1.0
Radiation physics and measurements	1.0
Chemistry of radioisotopes	1.0
Radiological protection ordinance including video	1.5
Safe handling of radioisotopes	1.5

Practices (one day)	Hours
Treatment of unsealed radioactive solution	4.0
Measurement of surface contamination and decontamination	1.0
Measurement of gamma-rays and beta-rays	2.0

Table 2. Distribution of trainees for "Radiation and Radioisotopes" in 2006.

Department	Staff	Student	Total	English class
CYRIC	0	4	4	0
Medicine	18	62	80	4
Dentistry	1	0	1	0
Pharmacy	1	48	49	3
Science	3	62	65	1
Engineering	10	73	83	6
Agriculture	3	73	76	2
Research Institutes	22	85	107	5
The others	0	0	0	0
Total	58	407	465	21

Table 3. Contents of the lectures for "X-ray machines and Electron microscopes" in 2006 (same for both Japanese and English class)

Lectures (one day)	Hours
Safe handling of X-ray machines	1.5
Radiological protection ordinance	0.5
Video for safe handling of radiation and radioisotopes	0.5

Table 4. Distribution of trainees for "X-ray machines and Electron microscopes" in 2006.

Department	Staff	Student	Total	English class
Medicine	6	1	7	1
Dentistry	1	2	3	0
Pharmacy	0	7	7	0
Science	4	27	31	10
Engineering	9	173	182	11
Research Institutes	20	101	121	25
The others	0	3	3	0
Total	40	314	354	37

Table 5. Distribution of trainees for "Synchrotron radiation" in 2006.

Department	Staff	Student	Total	English Class
Pharmacy	1	0	1	0
Science	3	10	13	0
Engineering	4	19	23	0
Research Institutes	17	34	51	3
Total	25	63	88	3

IX. 2. Radiation Protection and Management

Miyata T.[1], Yamazaki H.[1], Baba M.[1], Kato M.[1], and Nakae H.[2]

[1]Cyclotron and Radioisotope Center, Tohoku University
[2]Japan Radiation Protection Co., Ltd.

(1) Overview

During the fiscal year of 2006, research and education in the center were conducted as active as usual.

In June 2006, we received periodic inspection by Nuclear Safety Technology Center concerning the technological aspect and also management system without serious problems.

New ^{7}Li(p,n) neutron source installed at the 3-2 course of CYRIC in 2005 has been used for experiments of semiconductors irradiation.

Last year, "β-ray analysis room" in Radio Isotope Building was converted into PET Research Room to promote life science research using PET and a γ-camera. The 931 PET placed in Research Building was moved to the room after conversion of the room and approval of radiation licensing.

The online radiation protection and management system of CYRIC which was installed in 2002 worked reliably although some problems such as slowing down of the system response when the data transfer rate is so high. The radiation detectors connected with the monitoring system performed reliably too while one gamma-ray detector should be repaired.

The measurement of radioactivity concentration which was started along with the reorganization of national university in 2004 is continued periodically but the observed level was low enough generally. Devices and gas counters with automatic sample changer for radioactivity concentration measurement (samplers, α.-β automatic counters) were routinely used without serious problems by several radiation facilities in Tohoku University.

(2) Unsealed radio nuclides used in CYRIC

The species and amounts of unsealed radio nuclides handled in CYRIC during the

fiscal year of 2006 are summarized in Table 1. The table includes the isotopes produced by the cyclotron as well as those purchased from the Japan Radio Isotope Association or taken over from other radioisotope institutes.

(3) Radiation exposure dose of individual worker

The exposure doses of the workers in CYRIC during 2006 are given in Table 2. The doses were sufficiently lower than the legal dose limits.

(4) Radiation monitoring of the workplace

Radiation dose rates inside and outside of the controlled areas in CYRIC were monitored periodically and occasionally when needed. They were generally below the legal dose limits although there are several "hot spots" in mSv/hr range like slits or beam stopper of the 930 cyclotron and so on. Surface contamination levels of the floors inside the controlled areas were also measured with a smear method and a survey meter method. They were under the legal regulation levels.

(5) Wastes management

The radioactive wastes were delivered to the Japan Radio Isotope Association twice in the fiscal year of 2006.

The concentration of radioisotopes in the air released from the stack after filtration was monitored with stack gas monitors. The values of concentration were well below the legal regulation levels. The radioactive water was stocked in the tanks at least for 3 days and then released to the sewerage after confirming that the concentration was lower than the legal regulation levels.

Radioactive organic scintillator waste was treated periodically by incinerator provided by Fuji-kogyo Co.Ltd. The incinerator was overhauled last year.

Table 1. Unsealed radioisotopes used in each building of CYRIC during 2006.
(a) Cyclotron Building (kBq)

Group 2		Group 3		Group4	
		^{11}C	713,955,300.000	^{18}F	584,585,200.000
		^{15}O	370,000.000	^{7}Be	1,000.000
Total	0	Total	714,235,300.000	Total	584,585,200.000

(b) Radio-isotope Building (kBq)

Group 2		Group 3		Group4	
^{56}Co	2,287.210	^{11}C	1,850,000.000	^{14}C	5,180.000
^{125}I	110,983.008	^{32}P	1,713,192.370	^{18}F	13,812,100.000
		^{48}V	1,975.269	^{3}H	25,584.300
		^{124}I			
Total	113,270.218	Total	3,597,167.639	Total	13,842,864.300

* Including the use in the "β-ray analysis" room

(c) Research Building (kBq)

Group1,2		Group 3		Group 4	
		^{15}O	10,915,000	^{18}F	2,401,670
Total	0	Total	14,615,000	Total	2,401,670

Table 2. Occupational radiation exposures at CYRIC during the fiscal year of 2006.

Dose range (mSv)	Number of individuals
No measurable exposure	36
Less than 1.0	14
1.0 to 2.0	3
2.0 to 3.0	1
3.0 to 4.0	1
Total number of persons monitored	55

X. PUBLICATIONS

X. PUBLICATIONS

[661] Formation of Po @ C_{60}.
T. Ohtsuki, K. Ohno.
Phys. Rev., **B72** (2005) 153411-1-3.

[662] Recruitment of fusiform face area associated with listening to degraded speech sounds in auditory-visual speech perception: a PET study.
Tetsuaki Kawase, Keiichiro Yamaguchi, Takenori Ogawa, Ken-ichi Suzuki, Maki Suzuki, Masatoshi Itoh, Toshimitsu Kobayashi, Toshikatsu Fujii.
Neurosci. Lett., **382** (2005) 254-258.

[663] Experimental Studies on Particle and Radionuclide Production Cross Sections for Tens of MeV Neutrons and Protons.
M. Baba.
AIP Conf. Proc. Int. Conf. Nucl. Data for Sci. and Tech. – ND2004 (September 2004), **769** (2005) 884.

[664] Measurement of differential cross sections of secondary heavy particles induced by tens of MeV particles.
M. Hagiwara, T. Sanami, M. Baba, T. Oishi, N. Hirabayashi, M. Takada, H. Nakashima and S. Tanaka,
AIP Conf. Proc. Int. Conf. Nucl. Data for Sci. and Tech. – ND2004 (September 2004) **769** (2005) 1031.

[665] Measurement of differential thick target neutron yields (TTY) from Fe, Cu(p,n) reactions at 35, 50 and 70 MeV.
T. Itoga, M. Hagiwara, N. Kawata, T. Yamauchi, N. Hirabayashi, T. Oishi and M. Baba.
AIP Conf. Proc. Int. Conf. Nucl. Data for Sci. and Tech. – ND2004 (September 2004) **769** (2005) 1568.

[666] Experimental studies on excitation functions of the proton-induced activation reactions on silver.
M.S.Uddin, M.Hagiwara, M.Baba, F.Tarkanyi, F. Ditroi.
Appl. Radiat. Isot. **62** (2005) 533–540.

[667] Measurement of neutron emission spectra in Li(d,n) reaction with thick and thin Targets for 40 MeV deuterons.
M. Hagiwara, T. Itoga, N. Kawata, N. Hirabayashi, T. Oishi, T. Yamauchi, M. Baba, M. Sugimoto, T. Muroga.
Fusion Sci. Tech., **48** (2005) 1320.

[668] Experimental studies on excitation functions of the proton-induced activation reactions on yttrium.
M.S. Uddin, M. Hagiwara, M. Baba, F. Tarkanyi, F. Ditroi.
Appl. Radiat. Isot., **63** (2005) 367–374.

[669] Brain histamine H_1 receptor occupancy of orally administered antihistamines measured by positron emission tomography with ^{11}C-doxepin in a placebo-controlled crossover study design in healthy subjects: a comparison of olopatadine and ketotifen.
M. Tashiro, H. Mochizuki, Y. Sakurada, K. Ishii, K. Oda, Y. Kimura, T. Sasaki, K. Ishiwata, K. Yanai.
Brit. J. Clinic. Pharmacol., **61** (2005) 16-26.

[670] Differential Absorbed Dose Distributions in Lineal Energy for Neutrons and Gamma-rays at the Mono-energetic Neutron Calibration facility.
M. Takada, M. Baba, H. Yamaguchi, K. Fujitaka.
Radiat. Protect. Dosimetry, **114** (2005) 481-490.

[671] Study of the pionic enhancement in ^{16}O($p, p^{\prime}$) ^{16}O(0^{-}, T=1) at 295 MeV.
T. Wakasa, G.P.A. Berg, H. Fujimura, K. Fujita, K. Hatanaka, M. Ichimura, M. Itoh, J. Kamiya, T. Kawabata, Y. Kitamura, E. Obayashi, H. Sakaguchi, N. Sakamoto, Y. Sakemi, Y. Shimizu, H. Takeda, M. Uchida, Y. Yasuda, H.P. Yoshida, M. Yosoi.
Phys. Lett., **B632** (2006) 485-489.

[672] Dissociable Roles of Prefrontal and Anterior Cingulate Cortices in Deception.
Nobuhito Abe, Maki Suzuki, Takashi Tsukiura, Etsuro Mori, Keiichiro Yamaguchi Masatoshi Itoh, Toshikatsu Fujii.
Cerebral Cortex, **16** (2006) 192-199.

[673] *O*-[^{18}F]fluoromethyl-L-tyrosine is a potential tracer for monitoring tumour response to chemotherapy using PET: an initial comparative in vivo study with deoxyglucose and thymidine.
Gengo Yamaura, Takashi Yoshioka, Hiroshi Fukuda, Keiichiro Yamaguchi, Manami Suzuki, Shozo Furumoto, Ren Iwata, Chikashi Ishioka.
Eur. J. Nucl. Med. Mol. Imag., **33** (2006) 1135-1139.

[674] Functional characterization of the brain-to-blood efflux clearance of human amyloid- ß peptide (1-40) across the rat blood-brain barrier.
Shingo Ito, Sumio Ohtsuki, Tetsuya Terasaki.
Neurosci. Res., **56** (2006) 246-252.

[675] Major Involvement of Low-Density Lipoprotein Receptor-Related Protein 1 in the Clearance of Plasma Free Amyloid ß -Peptide by the Liver.
Chihiro Tamaki, Sumio Ohtsuki, Takeshi Iwatsubo, Tadafumi Hashimoto, Kaoru Yamada, Chiori Yabuki, Tetsuya Terasaki.
Pharmaceut. Res., **23** (2006) 1407-1416.

[676] Comparison of ^{18}F-fluoromethylcholine and 2-deoxy-D-glucose in the distribution of tumor and inflammation.

Kazuo Kubota, Shozo Furumoto, Ren Iwata, Hiroshi Fukuda, Kazunori Kawamura, Kiichi Ishiwata.
Ann. Nucl. Med., **20** (2006) 527-533.

[677] Medial frontal cortex perfusion abnormalities as evaluated by positron emission tomography in women with climacteric symptoms.
Tetsuro Abe, Daniel Bereczki, Yasuo Takahashi, Manabu Tashiro, Ren Iwata, Masatoshi Itoh.
Menopause, **13** (2006) 891-901.

[678] Muscle activity during a dash shown by ^{18}F-fluorodeoxyglucose positron emission tomography.
Masahiro Ohmura, Takehiko Sugita, Shoichi Kokubun, Keiichiro Yamaguchi, Hisashi Rikimaru.
J. Orthopaedic Sci., **11** (2006) 42-45.

[679] Quasi-monoenergetci Neutron Sources.
M.Baba.
Proc. Sci.; Proc. Int. Symp. Fast Neutron Detectors and its Application, April 2006, Cape Town.

[680] Noise elimination in lead-slowing down neutron spectrometer using digital signal processing.
Proc. Sci.; Proc. Int. Symp. Fast Neutron Detectors and its Application, April 2006, Cape Town.

[681] Benchmark experiments for neutron moderator assembly for cyclotron-based Boron Neutron Capture Therapy.
Y.Unno, S.Yonai, M.Baba, T.Itoga, S.Kamada, Y.Tahara, H.Yokobori.
Proc. Int. Congress on Neutron Capture Therapy (Oct. 9-13, 2006), (2006) 331-334.

[682] Installation and Application of Intense ^{7}Li(p,n) Neutron Source.
M. Baba, H. Okamura, M. Hagiwara, T. Itoga, S. Kamada, Y. Yahagi, E. Ibe
Proc. Int. Symp. on 10th Neutron Dosimetry, , Radiation Protection and Dosimetry, doi:10.1093/rpd/ncm005.

[683] Fast response neutron emission monitor for fusion reactor using stilben scintillator and flash-ADC.
T. Itoga, T. Okuji, N. Nakhstine, M. Baba, M. Ishikawa, T. Nishitani
Proc. Int. Symp. on 10th Neutron Dosimetry, , Radiation Protection and Dosimetry, doi:10.1093/rpd/ncm141.

[684] Differential cross section on neutron-induced frgament emission reaction for microdosimetry study
M. Hagiwara, T. Sanami, T. Oishi
Proc. Int. Symp. on 10th Neutron Dosimetry, Radiation Protection and Dosimetry, doi:10.1093/rpd/ncm022.

[685] Ultra fast, radiation resistant fast neutron detector.
M. Nakhostin.
Proc. Int. Symp. on 10th Neutron Dosimetry, Radiation Protection and Dosimetry, doi:10.1093/rpd/ncm040.

[686] Precise measurement of first Townsend coefficient, using parallel plate avalanche chamber
Mohammad Nakhostin, Mamoru Baba, Tsutomu Ohtsuki, Tadao Oishi, Toshiro Itoga
Nucl. Instrum. Meth. Phys. Res. A: **572** (2007) 999-1003.

[687] Excitation functions of long lived products in deuteron induced nuclear reactions on platinum up to 40 MeV.
F. Ditroi, F. Tarkanyi, J. Csikai, M.S. Uddin, M. Hagiwara, M. Baba, Yu.N. Shubin, S.F. Kovalev.
Nucl. Instrum. Meth. Phys. Res. B, **243** (2006) 20-27.

[688] Engineering Design of a Spallation Reaction-based Neutron Generator for Boron Neutron Capture Therapy.
Yoshihisa Tahara, Yasushi Oda, Takako Shiraki, Takehiko Tsutsui, Hitoshi Yokobori, Shunsuke Yonai, Mamoru Baba, Takashi Nakamura.
J. Nucl. Sci. Technol., **43** (2006) 9-19.

[689] Fast collimated neutron flux measurement using stilbene scintillator and flashy analog-to-digital converter in JT-60U
M. Ishikawa, T. Itoga, T. Okuji, M. Nakhostin, K. Shinohara, T. Hayashi, Sukegawa, M. Baba, T. Nishitani
Rev. Sci. Instrum., **77** (2006) 10E706-1~3.

[690] A BNCT Neutron Generator using 30 MeV proton beam.
Y. Tahara, S. Abe, Y. Akiyama, Y. Kamei, H. Yokobori, Y. Unno, Mamoru Baba.
Proc. Int. Congress on Neutron capture Therapy (Oct. 9-13, 2006), 327-330.

[691] Experimental studies of the deuteron-induced activation cross-sections on ^{nat}Ag.
M.S. Uddin, M. Hagiwara, M. Baba, F. Tárkányi, F. Ditrói, S. Takács, A. Hermanne.
Appl. Radiat. Isot. **64** (2006) 1013-1019.

[692] Excitation functions of long lived products in deuteron induced nuclear reactions on platinum up to 40 MeV.
F. Ditrói, T. F.árkányi, J. Csikai, M.S. Uddin, M. Hagiwara, M. Baba, Yu.N Shubin, S.F. Kovalev.
Nucl. Inst. Meth. Phys. Res. B **243** (2006) 20-27.

[693] Experimental study of the excitation functions of proton induced reactions on ^{nat}Sn up to 65 MeV.
A. Hermanne, F. Tárkányi, F. Ditrói, S. Takács, R. Adam Rebeles, M.S. Uddin, M. Hagiwara, M. Baba, Yu.N. Shubin, S.F. Kovalev.
Nucl. Instr. Meth. Phys. Res. B **247** (2006) 180-191.

[694] Activation cross-sections on cadmium: Proton induced nuclear reactions up to 80 MeV.
F. Tarkanyi, B. Kiraly, F. Ditroi, S. Takacs, J. Csikai, A. Hermanne, M.S. Uddin, M. Hagiwara, M. Baba, T. Ido, Yu.N. Shubin, S.F. Kovalev.
Nucl. Instr. Meth. Phys. Res. B **245** (2006) 379-394.

[695] Cross sections of deuteron induced nuclear reactions on irridium.
F. Tarkanyi, B. Kiraly, F. Ditroi, S. Stakacs, J. Csikai, A. Hermanne, M.S. Uddin, M. Hagiwara, M. Baba, YU.N. Shubin, S.F. Kovalev.
Nucl. Inst. Method Phys Res. B 247 , (2006) 210-216.

XI. MEMBERS OF COMMITTEE

XI. MEMBERS OF COMMITTEE (as of Jan. 1, 2007)

General

(Chairman)	Keizo	Ishii	(Graduate School of Engineering)
	Tetsuo	Shoji	(Executive Vice President)
	Osamu	Hashimoto	(Graduate School of Science)
	Kazuaki	Iwasa	(Graduate School of Science)
	Akira	Takahashi	(Graduate School of Medicine)
	Keiichi	Sasaki	(Graduate School of Dentistry)
	Koji	Fukunaga	(Graduate School of Pharmaceutical Sciences)
	Akira	Hasegawa	(Graduate School of Engineering)
	Ryoichi	Katsumata	(Graduate School of Agricultural Science)
	Kazuhiko	Nishitani	(Graduate School of Life Science)
	Isamu	Sato	(Institute for Materials Research)
	Hiroshi	Fukuda	(Institute for Development, Aging and Cancer)
	Osamu	Tochiyama	(Institute of Multidisciplinary Research for Advanced Materials)
	Syoki	Takahashi	(University Hospital)
	Jirohta	Kasagi	(Laboratory of Nuclear Science)
	Masatoshi	Itoh	(CYRIC)
	Mamoru	Baba	(CYRIC)
	Ren	Iwata	(CYRIC)
	Hiromichi	Yamazaki	(CYRIC)
	Yasuhiro	Sakemi	(CYRIC)
	Tsutomu	Shinozuka	(CYRIC)
	Manabu	Tashiro	(CYRIC)
	Hirokazu	Tamura	(Graduate School of Science)
	Kazuhiko	Yanai	(Graduate School of Medicine)

	Tetsuya	Ono	(Radiation Safety Committee, Research Promotion Council)
(Observer)	Seiko	Sato	(Head of Administration Office, Graduate School of Information Science)

Cyclotron

(Chairman)	Osamu	Hashimoto	(Graduate School of Science)
	Toshio	Kobayashi	(Graduate School of Science)
	Hideya	Onodera	(Graduate School of Science)
	Hirokazu	Tamura	(Graduate School of Science)
	Kazushige	Maeda	(Graduate School of Science)
	Yasushi	Kino	(Graduate School of Science)
	Keizo	Ishii	(Graduate School of Engineering)
	Akira	Hasegawa	(Graduate School of Engineering)
	Isamu	Sato	(Institute for Materials Research)
	Anpo	Sai	(Institute of Multidisciplinary Research for Advanced Materials)
	Tsutomu	Otsuki	(Laboratory of Nuclear Science)
	Masatoshi	Itoh	(CYRIC)
	Mamoru	Baba	(CYRIC)
	Ren	Iwata	(CYRIC)
	Hiromichi	Yamazaki	(CYRIC)
	Yasuhiro	Sakemi	(CYRIC)
	Tsutomu	Shinozuka	(CYRIC)

Radiation Protection and Training of Safe Handling

(Chairman)	Mamoru	Baba	(CYRIC)
	Kazuaki	Iwasa	(Graduate School of Science)
	Yoshihiko	Uehara	(Graduate School of Medicine)
	Tetuya	Terasaki	(Graduate School of Pharmaceutical Sciences)

	Keizo	Ishii	(Graduate School of Engineering)
	Michio	Komai	(Graduate School of Agricultural Science)
	Kazuhiro	Sogawa	(Graduate School of Life Science)
	Tatuo	Shikama	(Institute for Materials Research)
	Katuyoshi	Hori	(Institute for Development, Aging and Cancer)
	Tomohiro	Kaneta	(University Hospital)
	Ren	Iwata	(CYRIC)
	Hiromichi	Yamazaki	(CYRIC)
	Tsutomu	Shinozuka	(CYRIC)

Life Science

(Chairman)	Masatoshi	Itoh	(CYRIC)
	Noriaki	Ohuchi	(Graduate School of Medicine)
	Shogo	Yamada	(Graduate School of Medicine)
	Syoki	Takahashi	(Graduate School of Medicine)
	Teiji	Tominaga	(Graduate School of Medicine)
	Masahiko	Yamamoto	(Graduate School of Medicine)
	Yukitsuka	Kudo	(Biomedical Engineering Research Organization)
	Keiichi	Sasaki	(Graduate School of Dentistry)
	Masayuki	Seki	(Graduate School Pharmaceutical Sciences)
	Keizo	Ishii	(Graduate School of Engineering)
	Kazuhiko	Nishitani	(Graduate School of Life Science)
	Takashi	Yoshioka	(Institute for Development, Aging and Cancer)
	Nariyasu	Mano	(University Hospital)
	Yoshihiro	Takai	(College of Medical Sciences)
	Ren	Iwata	(CYRIC)
	Hiromichi	Yamazaki	(CYRIC)
	Manabu	Tashiro	(CYRIC)

	Yoshihito	Funaki	(CYRIC)

Prevention of Radiation Hazards

(Chairman)	Mamoru	Baba	(CYRIC)
	Naohito	Iwasa	(Graduate School of Science)
	Yasushi	Kino	(Graduate School of Science)
	Keizo	Ishii	(Graduate School of Engineering)
	Ren	Iwata	(CYRIC)
	Hiromichi	Yamazaki	(CYRIC)
	Yasuhiro	Sakemi	(CYRIC)
	Tsutomu	Shinozuka	(CYRIC)
	Manabu	Tashiro	(CYRIC)
	Takamoto	Miyata	(CYRIC)
	Tomoya	Yonezawa	(CYRIC)

Research Program

(Chairman)	Mamoru	Baba	(CYRIC)
	Osamu	Hashimoto	(CYRIC)
	Toshio	Kobayashi	(Graduate School of Science)
	Hirokazu	Tamura	(Graduate School of Science)
	Kazushige	Maeda	(Graduate School of Science)
	Kazuhiko	Yanai	(Graduate School of Science)
	Akira	Takahashi	(Graduate School of Medicine)
	Akira	Hasegawa	(Graduate School of Engineering)
	Atuki	Terakawa	(Graduate School of Engineering)
	Isamu	Sato	(Institute for Materials Research)
	Takashi	Yoshioka	(Institute for Development, Aging and Cancer)
	Syoki	Takahashi	(University Hospital)
	Jirohta	Kasagi	(Laboratory of Nuclear Science)
	Tsutomu	Otsuki	(Laboratory of Nuclear Science)

Tsutomu	Sekine	(Center for the Advancement of Higher Education)
Masatoshi	Itoh	(CYRIC)
Ren	Iwata	(CYRIC)
Hiromichi	Yamazaki	(CYRIC)
Yasuhiro	Sakemi	(CYRIC)
Tsutomu	Shinozuka	(CYRIC)
Manabu	Tashiro	(CYRIC)

XII. STAFF

XII. STAFF (as of Jan. 1, 2007)

Director Keizo Ishii

Division of Accelerator

Osamu	Hashimoto[1)]
Tsutomu	Shinozuka
Takashi	Wakui
Mifuyu	Ukai
Shizuo	Chiba[6)]
Yasuaki	Ohmiya[6)]
Naoto	Takahashi[6)]
Shigenaga	Yokokawa[6)]

Division of Instrumentations

Sakemi	Yasuhiro
Hirokazu	Tanura[1)]
Hikonojo	Orihara[5)]
Hiroyuki	Okamura[5)]
Atuki	Terakawa[3)]
Masatoshi	Itoh
Sho-ichi	Watanuki
Kazutaka	Ohzeki

Division of Radiopharmaceutical Chemistry

Ren	Iwata
Yukitsuka	Kudo[4)]
Yoshihito	Funaki
Yohichi	Ishikawa
Shozo	Furumoto[4)]

Division of Cyclotron Nuclear Medicine

Masatoshi	Itoh
Kazuhiko	Yanai[2)]
Keiichiro	Yamaguchi[5)]
Kohichiro	Kawashima[5)]
Manabu	Tashiro
Masayasu	Miyake
Maki	Suzuki
Mehedi	Masud
Sabina	Khond Kar
Kazuaki	Kumagai
Takehisa	Sasaki
Kyokutoh	Dan
Targino Rodrigues Dos Santos	
Takeshi	Ogura

Division of Radiation Protection and Safety Control

Mamoru	Baba
Hiromichi	Yamazaki
Takashi	Nakamura[5)]
Takamoto	Miyata
Tomoyoshi	Yamazaki
Hirokazu	Nakae[7)]

Graduate Student and Researcher

Tomokazu	Suzuki	(Graduate School of Science)
Yu-ji	Miyashita	(Graduate School of Science)
Nozomi	Sato	(Graduate School of Science)
Miharu	Ohkuma	(Graduate School of Science)
Naoya	Sugimoto	(Graduate School of Science)
Shingo	Fukushima	(Graduate School of Science)
Tomohiro	Terazono	(Graduate School of Science)
Ryo	Matsuo	(Graduate School of Science)
Miki	Tateoka	(Graduate School of Science)

Yoshio	Honda	(Graduate School Pharmaceutical Sciences)
Makoto	Sasaki	(Graduate School Pharmaceutical Sciences)
Akihiro	Sugawara	(Graduate School, Division of Medicine)
Margaretha	Sulistyoningsih	(Graduate School, Division of Medicine)
Toshiro	Itoga	(Graduate School of Engineering)
Takuji	Ohishi	(Graduate School of Engineering)
Mohammad	Nakhostin	(Graduate School of Engineering)
Akram	Mohammadi	(Graduate School of Engineering)
Yasuhiro	Unno	(Graduate School of Engineering)
Soh	Kamata	(Graduate School of Engineering)
Wataru	Takahashi	(Graduate School of Engineering)
Toshio	Okuchi	(Graduate School of Engineering)
Yoichi	Yamaguchi	(Graduate School of Engineering)

Office Staff

Seiko	Sato
Tomoya	Yonezawa
Yoshiaki	Kawamura
Yu-ko	Yamashita
Mitsuko	Endo
Kyoko	Fujisawa
Fumiko	Mayama
Masakatsu	Itoh
Kietu	Takahashi
Kimiko	Abe
Asami	Sawada
Yoshiro	Sukegawa
Ai	Endo
Shurikeiko	Fujimoto

1) Graduate School of Science
2) Graduate School of Medicine
3) Graduate School of Engineering
4) TUBERO
5) Visiting Professor
6) SUMI-JU Accelerator Service Ltd.
7) Japan Radiation Protection Co., Ltd.